

UNIVERSITAT POLITÈCNICA DE CATALUNYA  
CONSEJO SUPERIOR DE INVESTIGACIONES CIENTÍFICAS

GRAVITATIONAL WAVE RADIATION  
FROM SINGLE AND BINARY  
WHITE DWARFS

by

PABLO LORÉN AGUILAR

A THESIS SUBMITTED FOR THE DEGREE OF

DOCTOR OF PHILOSOPHY

ADVISORS:

ENRIQUE GARCÍA-BERRO  
JORDI ISERN

*Barcelona, November 2008*



*Alabado seas, Señor,  
por la hermana Luna,  
por el cielo de noche,  
y todas las estrellas del firmamento.  
Qué brillantes las has hecho,  
qué preciosas y bellas.*

San Francisco de Asís



# Contents

<b>Motivation and outline of the thesis</b>	<b>v</b>
<b>1 Introduction</b>	<b>1</b>
1.1 The last window of astronomy: gravitational waves . . . . .	1
1.2 Gravitational waves from pulsating white dwarfs . . . . .	5
1.3 Galactic white dwarf binaries . . . . .	8
<b>2 The gravitational wave radiation from pulsating white dwarfs</b>	<b>11</b>
2.1 Introduction . . . . .	11
2.2 Input physics and method of calculation . . . . .	13
2.2.1 Nonradial pulsation modes . . . . .	13
2.2.2 Numerical codes . . . . .	14
2.2.3 Gravitational waves from a pulsating white dwarf . . . . .	14
2.3 Results . . . . .	16
2.3.1 Gravitational wave signal . . . . .	16
2.3.2 Detectability . . . . .	23
2.4 Discussion and conclusions . . . . .	26
<b>3 Gravitational wave radiation from the coalescence of white dwarfs</b>	<b>29</b>
3.1 Introduction . . . . .	29
3.2 Gravitational wave emission in SPH . . . . .	31
3.3 Calibration and consistency checks . . . . .	32
3.4 Results . . . . .	35
3.4.1 Gravitational wave emission . . . . .	35
3.4.2 Detectability . . . . .	43
3.5 Discussion and conclusions . . . . .	47
<b>4 High-resolution SPH simulations of the merger of white dwarfs</b>	<b>49</b>
4.1 Introduction . . . . .	49
4.2 Input physics and method of calculation . . . . .	52
4.3 Results . . . . .	55
4.4 Discussion . . . . .	63

4.4.1	Comparison with theory . . . . .	63
4.4.2	Gravitational wave radiation . . . . .	69
4.4.3	Fallback luminosities . . . . .	71
4.4.4	Long-term evolution . . . . .	73
4.5	Conclusions . . . . .	76
<b>5</b>	<b>Evidence of a merger of binary white dwarfs: the case of GD 362</b>	<b>79</b>
5.1	Introduction . . . . .	79
5.2	Characteristics of the merger products . . . . .	80
5.3	Results . . . . .	84
5.3.1	The chemical abundances . . . . .	84
5.3.2	The infrared excess . . . . .	88
5.3.3	Accretion from planets or asteroids . . . . .	89
5.3.4	Magnetic braking . . . . .	90
5.4	Discussion and conclusions . . . . .	94
<b>6</b>	<b>Conclusions</b>	<b>97</b>
<b>A</b>	<b>Gravitational waves</b>	<b>101</b>
A.1	General relativity . . . . .	101
A.2	Linearized general relativity . . . . .	102
A.3	Plane waves . . . . .	104
A.4	The sources of gravitational waves . . . . .	106
<b>B</b>	<b>The essence of SPH</b>	<b>109</b>
B.1	Introduction . . . . .	109
B.2	Interpolation . . . . .	110
B.3	SPH derivatives . . . . .	112
B.4	Errors in the integral interpolant . . . . .	113
B.5	SPH Euler equations . . . . .	114
B.6	Resolution varying in space and time . . . . .	116
B.7	Artificial viscosity . . . . .	117
B.8	Integration . . . . .	121
<b>C</b>	<b>Cluster architecture</b>	<b>125</b>
C.1	Characteristics of the cluster . . . . .	125
<b>D</b>	<b>Code parallelization</b>	<b>129</b>
D.1	Message Passage Interface and parallelization strategy . . . . .	129

# Agradecimientos

Johann Wolfgang Goethe dijo una vez que, si nos encontramos a alguien que nos debe agradecimiento, enseguida lo recordamos. Pero cuántas veces nos encontramos con alguien al que debemos agradecimiento y no pensamos en ello! Con este espíritu, me gustaría mostrar mi más profundo y sincero agradecimiento a todas aquellas personas que de un modo u otro han contribuido a hacer que este apasionante viaje, emprendido hace ya unos cuantos años, llegase a buen puerto.

Como es lógico, todo barco que desee navegar necesita un buen timón, y yo he tenido la inmensa suerte de poder contar con uno de excepción. Enrique y Jordi, os agradezco de todo corazón que me admitierais como vuestro estudiante y me permitiésteis comenzar lo que siempre había sido un sueño para mí. Mucho es lo que he aprendido de vosotros y más aún lo que me queda por aprender. Habéis sido unos maravillosos maestros y, si he podido hacer mía aunque sea sólo una ínfima parte de vuestro modo de entender la ciencia, me consideraré una persona privilegiada. En particular, Enrique, te quería agradecer haber sabido guiarme con paciencia, fe y habilidad a través del día a día. Gracias por tu infinita capacidad de trabajo y espero que gracias a lo que he aprendido de tí, pueda ser yo el que algún día te diga: “¿Ves?, tengo razón, como casi siempre”.

Además de un buen timón, un barco necesita un buen casco. Necesita ser de un noble material, que se mantenga a flote y sea resistente. Desde luego, si a alguien tengo que agradecer haberme proporcionado la fortaleza necesaria para mantenerme a flote todos estos años es a mis padres. Nunca podré agradecerlos lo suficiente los valores que desde muy pequeño me inculcásteis. Gracias a vosotros aprendí a amar la ciencia y gracias a vosotros he llegado hasta donde estoy ahora. Es mirándome en vosotros como he crecido cada día y trato de mejorar como persona, es mirándome en vosotros como anhelo mi futuro y, es mirándome en vosotros como me gustaría echar la vista atrás y poder decir que he vivido.

Y qué sería de un viaje en barco sin unos buenos compañeros de travesía. Durante los últimos años he tenido la inmensa fortuna de compartir un espacio y un tiempo con unos maravillosos compañeros de trabajo. Que me han ayudado en infinitas ocasiones siempre que los he necesitado, que han sido mi paño de lágrimas cuando las cosas no han salido bien y que han aguantado con paciencia mi exagerada tendencia a hablar demasiado sobre mí mismo. En especial, me gustaría agradecerlos

a todos vosotros, los descamisados, la infinidad de agradabilísimas comidas que hemos compartido juntos. Las charlas de sobremesa, las risas y los chistes malos, las comidas de chiringuito, los chismes y cotilleos, los miles de *youtubes*, el te de arengadas, las lecciones de nihilismo, sarcasmo y mucho más. Muchas gracias a todos por ser como sois. Dicen que quien tiene un amigo tiene un tesoro, pues bien, yo me siento el hombre más rico del mundo, muchísimas gracias. Muchas gracias también a los que han sido mis compañeros en el mundo del SPH: Josep, Alba y Joakim. Gracias por vuestro trabajo del que tanto he aprendido y gracias por mostrarme los errores, que yo por mí mismo jamás hubiese sido capaz de ver. Y por supuesto, gracias a los que habéis sido mis maestros en el noble arte del Linux. Josep, Dani, Fernando y Toni, sin vosotros mi trabajo y crecimiento profesional hubiera sido imposible. Mil gracias por vuestra paciencia y por tantas y tantas cosas que me habéis enseñado. Os merecéis también una y mil gracias todas aquellas personas que durante años habéis aguantado mi ineptitud a la hora de llevar los trámites administrativos de mi tesis. Silvia, Esther, Jordi, Isabel, Eva, Anna, Pilar. . . El vuestro es un trabajo muy duro y en demasiadas ocasiones muy poco reconocido. Sin vuestro esfuerzo, nada de esto hubiera sido posible. Muchas gracias por tener paciencia conmigo y por vuestro inmejorable trabajo.

Y por último, pero no por ello menos importante, un barco necesita un rumbo. Y qué mejor guía podría tener un barco que las estrellas. Estrellas, que han guiado mi vida desde muy pequeño, como bien podrían atestiguar mis padres, y que continúan haciéndolo en la actualidad. Pero sin duda, la estrella más brillante y hermosa que jamás ha guiado y guiará mi vida no reluce en el cielo, sino que lo hace aquí, a mi lado desde hace ya casi diez años. Ana, gracias por hacerme un hombre feliz. Gracias por ser mi guía en este loco viaje de la vida. Contigo, todo es un poquito más fácil, y sin duda, tu apoyo constante y comprensión, así como tu inquebrantable empeño en que consiguiera mi sueño, han sido unos de los grandes responsables de que ahora esté escribiendo estos agradecimientos. Te quiero, siempre te he querido, y siempre te querré.

Finalmente, simplemente quería pedir perdón a todas aquellas personas que por algún motivo, se hayan podido sentir ofendidas por algo que yo haya hecho o dicho. Jamás fué mi intención ofender a nadie ni jamás lo será. De todo corazón, mil gracias a todos y espero poder continuar navegando mucho tiempo a vuestro lado, mientras juntos, contemplamos las estrellas.

Desde un punto de vista material, la elaboración de esta tesis ha sido posible gracias a la ayuda del Ministerio de Educación y Ciencia mediante una beca de formación de investigadores. También ha sido parcialmente financiada por los proyectos AYA05-08013-C03-01/02, por la Unión Europea (FEDER), y por la AGAUR.

# Motivation and outline of the thesis

Although gravitational waves are a prediction of the Theory of General Relativity, and although there have been some observations that suggest that this prediction might be right, no direct observation has been successful until now. Many efforts are being done in order to construct a new generation of, either ground or space-based, gravitational wave detectors. Some examples are LISA, TAMA, LIGO, and VIRGO. Each of these detectors has or will have its own gravitational wave frequency range, allowing for the observation of different astrophysical phenomena. In particular, LISA (Laser Interferometer Space Antenna) a joint ESA and NASA effort should be able to eventually detect the gravitational wave emission from galactic binaries involving at least a degenerate object (Mironowski 1965; Evans et al. 1987), such as double neutron stars binaries, cataclysmic binaries, close double white dwarf binaries and binary systems composed of a white dwarf and a neutron star. Additionally the range frequencies of LISA would also allow for the detection of gravitational waves arising from the non-radial pulsations of white dwarfs. In the present thesis, the gravitational wave emission from single and binary white dwarfs is going to be studied.

White dwarfs are, by far, the most numerous stellar remnants in our Galaxy. Consequently, its study is of paramount importance to understand the current evolutionary status of the Galaxy. This, together with the relatively simple and well known physical processes involved in their formation and evolution, makes them an ideal tool for fundamental physics. A good fraction of white dwarfs belongs to binary systems. Moreover, the final destiny of these binary systems is to merge due precisely to energy loss by the emission of gravitational waves. Such an emission is expected to be detectable by LISA, due to the frequency range at which typically white dwarf binary systems are supposed to radiate (Hils et al. 1990). Also, single pulsating white dwarfs are supposedly powerful sources of gravitational waves. In particular, certain non-radial pulsational modes could be detectable by space-borne detectors, since it can be shown that the frequency of the radiated gravitational waves lies within the range of sensibility of LISA — see García-Berro et al. (2006) and references therein. However, in order for LISA to be able to detect gravitational

waves, it is of primordial importance to have a complete set of waveforms to which the otherwise noisy signal which LISA will record can be compared. According to the previous discussion the goals of the present thesis are, on the one hand, to develop efficient numerical algorithms able to follow the hydrodynamical evolution of the merger of binary systems and, on the other, to compute accurate gravitational wave emission patterns of such systems in order to predict what LISA could eventually detect. Additionally, we also pretend to study the gravitational wave emission of single pulsating white dwarfs.

We have organized the present thesis in the following way. The first chapter reviews the most relevant issues concerning the emission of gravitational waves. We also review some of the most relevant aspects of pulsating white dwarfs and of white dwarf binary systems. For the sake of completeness we also will provide some details about the characteristics of LISA. Chapter 2 is devoted to study the gravitational wave patterns of single pulsating white dwarfs and to analyze the ability of LISA to detect them. It follows chapter 3, where we study the gravitational wave emission of coalescing double white dwarfs binary systems. In both chapters we will pay especial attention to the possible detectability of such signals by LISA. In chapter 4 we perform high resolution simulations of the merger of binary white dwarfs in order to check the sensitivity of our results to the resolution employed in the calculations. Finally in chapter 5 we analyze possible outcomes of the mergers studied in chapter 3 and 4. More specifically, we study if a massive white dwarf, GD 362, with very anomalous surface composition could be the result of the merger of two white dwarfs. This might bear important consequences because the origin of these peculiar white dwarfs is still unknown. Finally, in chapter 6 we will draw our conclusions and some possible future research lines will be pointed out.

Additionally, the most basic aspects of the gravitational wave theory are reviewed in appendix A, whereas in appendix B we describe the most relevant features of our numerical code. It is important to realize that in order to simulate an intrinsically three-dimensional phenomenon like the coalescence of binary white dwarfs we have used a technique called SPH (Smoothed Particle Hydrodynamics). The reader should bear in mind that SPH is an approximate technique to solve the equations of fluid dynamics. However, we will show that this technique is specially well suited for the kind of problems we want to solve. This technique was first introduced by Lucy (1977). Since then, it has been successfully used in many fields, being perhaps astrophysics one of the most relevant amongst them. We have used a previously developed code (Guerrero et al. 2004) which already has been shown to be efficient and to provide reliable results. Nevertheless, given the numerical difficulties which must be faced when simulating the astrophysical situations which are studied in the present thesis, a substantial part of the work which is described here has consisted in improving its performance and reliability. More specifically, perhaps the most relevant contributions — but not the only ones — have been the introduction of a new prescription of artificial viscosity, the inclusion of individual timesteps for

each of the particles and the parallelization of the code. Finally, in appendix C we describe in some detail the technical details of our particular implementation of the code, paying special attention to code parallelization and to the specially built-in cluster of computers.



# Chapter 1

## Introduction

Gravitational waves are a direct consequence of General Relativity. Much effort has been made to detect them, but due to the intrinsic experimental difficulties involved in detection and data analysis no definite result has yet been obtained. Supernova core collapse, binary systems involving compact objects and pulsating neutron stars are, amongst others, promising sources of gravitational waves — see Schutz (1999) for a comprehensive review of the subject. Moreover, with the advent of the current generation of terrestrial gravitational wave detectors, like LIGO (Abramovici et al. 1992), VIRGO (Acernese et al. 2004), GEO600 (Willke et al. 2004), or TAMA (Takahashi & the TAMA Collaboration 2004), and of space-borne interferometers like LISA (Bender 1998, 2000), gravitational wave astronomy will probably soon be a possible reality.

### 1.1 The last window of astronomy: gravitational waves

The existence of gravitational waves is nowadays almost universally accepted. Essentially, gravitational waves can be thought as *ripples in space-time*. In other words, due to the fact that in General Relativity space and time become dynamical variables, certain ondulatory space-time solutions similar to those found in electromagnetic theory can be found. Although very different in its concept, gravitational wave detectors are intended to be the analogous of the traditional optical telescopes. This new generation of telescopes will allow us to enter into a completely new range of observational events, some of which might lead us to completely new scenarios or even to new astrophysical paradigms.

There are different possible designs for such gravitational telescopes. Some of them are based on laser interferometry and some other are based on material acoustic resonances, but all of them rely on the same physical principle. These detectors are designed to measure the distortion that is created by a gravitational wave as it transverses a certain region of the space-time. Unfortunately these distortions are

extremely weak, making its detection an enormous challenge. The first one to point out the possibility of detecting gravitational waves was Joseph Weber in the early sixties. He designed a resonant antenna consisting in a 1.5 tons cylinder surrounded by some piezoelectric crystals. He showed that when a gravitational wave crosses the detector, an electric signal would be emitted. The cylinder mass and size were carefully chosen in order to make the fundamental vibrational frequency be coincident with the expected gravitational wave frequency of a typical core collapse supernova event. Unfortunately and despite the claims of Weber of several gravitational wave detections, nowadays we know that his design was not sensitive enough. However, his pioneering work started a global effort towards the construction of newer and more sensitive detectors. Nowadays, resonant detectors have been notably improved with respect to the original designs of Weber, although the underlying physical principles are the same. Some good examples of them are the Italian AURIGA (Cerdonio et al. 1993) project, the Dutch miniGRAIL (Coccia et al. 1998) sphere or the United States ALLEGRO project.

However, in the last few years another detection method has been shown to be an alternative to resonant detectors. Interferometric techniques have been proven to be the best option in the endeavour of detecting gravitational waves. If a gravitational wave transverses the arm of an interferometer the change in the arm-length must be translated into a measurable change in the phase difference. The only problem relies in the extremely small change that a gravitational wave will produce into a laboratory-sized interferometer. In order to solve the problem kilometer-sized detectors have been constructed in different countries around the world. In spite of the gigantic size of such detectors, the change in the arm-length of the detector is still almost at the limit of detectability — one thousandth the diameter of a proton for a 4 km arm-long interferometer — and supposes a tremendous technical effort. Some examples of this type of detectors are the American detector LIGO (Abramovici et al. 1992), the European VIRGO (Acernese et al. 2004), or the Japanese TAMA (Takahashi & the TAMA Collaboration 2004). The frequency interval covered by this kind of detectors ranges from a few Hz up to some tenths of kHz, being instrumental noise the responsible of the upper limit and terrestrial noise of the lower one. Despite these limitations, terrestrial interferometric detectors should in principle be able to detect events like core-collapse supernova, rotating neutron stars or black hole-neutron star mergers. Unfortunately, events like massive black hole mergers, emission from galactic compact binaries or relic emission from the very early universe will be by far out of the observable frequency range.

The main source of noise below 1 Hz in terrestrial detectors are gravitational gradients induced by time variations of the local gravitational potential. Thus, the only way of detecting smaller frequencies is by going into space. This is precisely the aim of LISA (Laser Interferometer Space Antenna). This space mission will consist basically in a giant Michelson Morley interferometer (Prince et al. 2007). It will use a three-satellite constellation, which will form a 5 million kilometers sided equilateral

triangle, in order to perform very accurate interferometric measures of the distance between the satellites as this distance changes when gravitational waves cross it — see appendix A. The three satellites will orbit around the Sun in the ecliptic plane, 1 AU from the Sun and 20 degrees behind Earth. The natural free-fall orbits of the three satellites maintain this triangular formation throughout time, with the triangle appearing to rotate about its center once per year (Prince et al. 2007). Possible variations of arm length due to orbital motion will not affect the results, because the typical frequency of such changes is safely out of the observational range.

Despite being very simple in concept, LISA represents a huge technological challenge. There are many issues which are at the edge of the current technological capabilities but perhaps one of the most serious problems of the mission is the so-called drag-free mechanism. In order to ensure that the measured changes of the distance between the satellites are only due to gravitational waves, each of the satellites will carry a platinum-gold test mass which must be in an as perfect as possible free fall. These test masses will be used as an inertial reference for the local optical assembly (Prince et al. 2007). Each one of the satellites will be moving around its test mass acting as a shield for any external disturbance, sensing test mass position and using on-board rockets to correct its position as necessary without changing noticeably the trajectory of the test mass. It must be proven to be feasible and in order to do so a previous mission, called LTP (LISA Test Package), will be launched around 2010.

Another example of the technical difficulties is the beam dispersion of the interferometric laser. It will be so weakened after travelling the 5 million kilometers distance between satellites that the signal must be received, amplified and returned with the same phase and frequency as the incoming one. This has never been implemented in any previous space mission (Schutz & Ricci 2001), but there are preliminary studies that ensure that this can be indeed done. A detailed description of the mission is, however, beyond the scope of this work. The reader interested in the technological details of the LISA mission might take a look at the excellent review documents available at <http://lisa.esa.int> and <http://lisa.nasa.gov/>.

For the purpose of this work it is nevertheless important to review some important scientific issues of LISA. In particular, one of these issues is the range of frequencies to which LISA will be sensitive. This frequency range that LISA will cover lies between 1 and  $1 \times 10^{-4}$  Hz approximately. This frequency interval is limited by the test-mass acceleration noise in the low-frequency band, by the shot noise and the optical-path measurement errors in the mid-frequency band and by the arm length in the high-frequency band. An order of magnitude approximation of the minimum gravitational wave signal that LISA will be able to detect is

$$h = \frac{\Delta l}{l} \sim 10^{-23} \quad (1.1)$$

in one year of observation, with a signal-to-noise ratio of 5. That is, LISA will be able

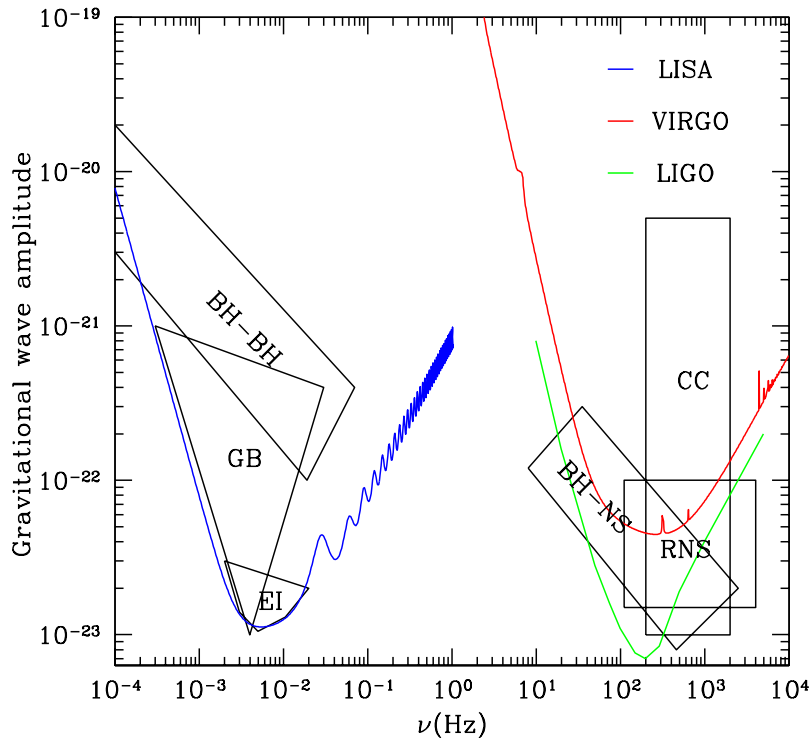


Figure 1.1: Sources of gravitational waves of astrophysical interest. The expected dimensionless strains are compared to the sensitivities of the two terrestrial major gravitational wave detectors: LIGO and VIRGO, and to the expected sensitivity of LISA. In this figure CC stands for core-collapse supernova, RNS for rotating neutron stars, BH-NS for black hole-neutron star mergers, BH-BH for the coalescence of binary black holes, GB for Galactic binaries and, finally, EI for extreme mass-ratio inspirals.

to measure variations of 0.05 picometers over a separation of 5 million kilometers (Prince et al. 2007). This frequency and amplitude combination will cover some of the most interesting known high-energy astrophysical events. In Fig. 1.1 we show a comparison of the sensitivity limits of LISA, and the previously mentioned VIRGO and LIGO. As can be seen both detectors complement the measurements that LISA will eventually perform. In this figure are also shown the expected amplitudes and frequencies in which some of the previously mentioned gravitational wave sources would radiate.

Thus, due to the forthcoming operation of LISA, it is essential to develop a complete set of waveforms to which the otherwise noisy signal which LISA will record can

be compared. As previously said, one of the aims of the present thesis is to compute such waveforms for two interesting and common astrophysical phenomena, the non-radial pulsations of white dwarfs and the merging of binary systems of white dwarfs. The next sections will be devoted to the study of the physics of such phenomena and its relation with the LISA mission.

## 1.2 Gravitational waves from pulsating white dwarfs

As explained in detail in appendix A, the gravitational wave emission in the mass-quadrupole approximation is given by

$$h_{jk}^{\text{TT}}(t, \vec{x}) = \frac{2G}{c^4 d} \ddot{Q}_{jk}^{\text{TT}}(t_r) \quad (1.2)$$

where  $\ddot{Q}$  stands for the second time derivative of the mass quadrupole and  $t_r$  is the retarded time. The order of magnitude of the gravitational wave signal will be then

$$h \sim \frac{G}{c^4} \frac{Mv^2}{d} \sim \frac{G}{c^4} \left( \frac{E_k}{d} \right) \sim 8 \times 10^{-50} \left( \frac{E_k}{d} \right) \quad (1.3)$$

where  $E_k$  is the kinetic energy involved in the process leading to the emission of gravitational waves and  $d$  is the distance to the source of gravitational waves. Accordingly, it can be seen from Eq. (1.2) that only those mass displacements with a non-zero mass quadrupole second derivative — that is, with non-symmetric accelerated mass displacements — will radiate gravitational waves. Furthermore, in order to obtain amplitudes of the order of  $10^{-23}$  large masses and velocities are necessary. For example, for an hypothetical process located at a distance of  $\sim 10$  kpc — which is approximately the distance to the Galactic center — a kinetic energy of  $E_k \sim 10^{48}$  erg would be needed for LISA to be able to detect the event.

One of the simplest astrophysical processes which can lead to the emission of gravitational waves are non-radial pulsations of white dwarfs. White dwarfs are the most numerous remnants of stellar evolution and apart from the obvious fact that the non-radial pulsations of such star have a non-zero second time derivative of the quadrupole moment, it can be easily seen that they involve enough kinetic energy to become detectable because the relevant range of frequencies lies within the sensibility band of LISA. Consider for example a white dwarf of  $\sim 1M_\odot$  undergoing non-radial oscillations with a period of  $\sim 1$  s and with an amplitude  $\delta R/R \sim 10^{-4}$ , which are otherwise typical values for white dwarfs. The kinetic energy associated the mass displacements of such stars is  $E_k \sim Mv^2 \sim 10^{45}$  erg, which is not far from the lower observational limit of LISA. Hence, gravitational wave emission from galactic pulsating white dwarfs should in principle be a serious candidate to be detected by LISA. Thus, in the remaining of this section we describe in some detail the main characteristics of pulsating white dwarfs.

Nowadays it is commonly believed that all stars pulsate during some phases of their evolution. As first suggested by Eddington, for stellar pulsations to be driven stellar material must be able to increase its net thermal energy content for every thermodynamic cycle around its equilibrium state. The most widely accepted driving mechanism is the so called  $\kappa$  mechanism. The opacity,  $\kappa$ , can be understood as the capacity of a certain material for trapping electromagnetic radiation. Its dependence on the density and temperature of the stellar material is given to a first order approximation by Kramer's law

$$\kappa \propto \frac{\rho}{T^{7/2}} \quad (1.4)$$

It is easy to see that for an ideal gas when contraction is proceeding opacity must decrease due to its highest sensibility to temperature. This would prevent any thermal energy gain, thus damping any pulsation that might be eventually present. However, the situation becomes different for the stellar regions in which the material is partially ionized. When contraction proceeds in these regions, the temperature does not rise as much as expected, due to the fact that some of the energy released during contraction is used to further increase the degree of ionization. Consequently, the density dependence dominates and the opacity of the stellar material increases. On the contrary, when stellar material is expanding recombination takes place, releasing energy which prevents the material to be cooled as much as it should be expected. Consequently, again the density dependence dominates and the opacity of the stellar material is reduced. As a result of this process, stellar material is able to increase its thermal energy content and stellar pulsations are sustained. Accordingly, and quite generally, stars — and most particularly, white dwarfs — pulsate non-radially. Fig. 1.2 shows an example of a non-radial pulsation mode. These non-radial pulsations can be classified into three basic types, depending on the main restoring mechanism. For the case of the so-called  $p$ -modes the main restoring force is pressure, whereas for  $g$ -modes the main restoring force is gravity. Finally,  $f$ -modes are an intermediate case between  $p$ - and  $g$ -modes. In all the cases, these kind of stellar oscillations have a typical pulsational time-scales of the order

$$\tau \sim \sqrt{G\rho} \quad (1.5)$$

Note that adopting a typical density of  $\sim 10^6$  g/cm<sup>3</sup> for a white dwarf gives a pulsational period of  $\sim 1$  s, which is well within the sensitivity band of LISA. Detailed calculations show that pulsational periods of white dwarf range typically from a few seconds — for  $f$ - and  $p$ -modes — up to 1000 seconds for  $g$ -modes.

White dwarfs can be classified in two main groups, the ones showing hydrogen in their spectra — usually referred to as DA white dwarfs — and those which do not show hydrogen in their spectra — known as non-DA white dwarfs. This latter group can be further divided in several different subgroups according to their spectral features — DO, DB, DQ, DC... Of particular interest for the forthcoming discussion

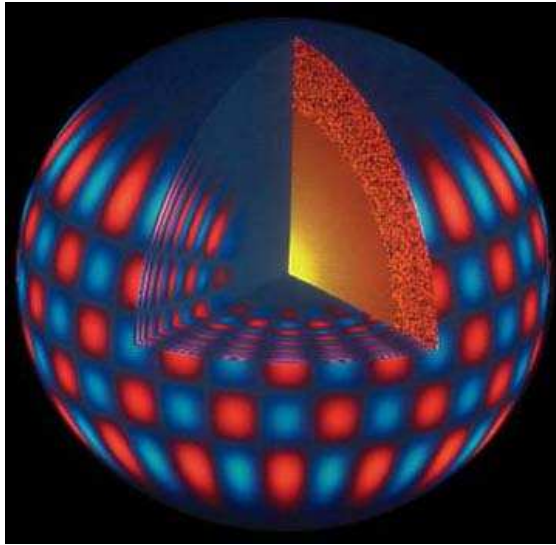


Figure 1.2: Representation of a non-radial pulsational mode in a star.

are those white dwarfs which show He I spectral features — which are known as DB white dwarfs — and those stars showing either pure He II spectra or mixed He I and He II spectra — which are called DO white dwarfs. The former classification is valid for both pulsating and non-pulsating white dwarfs. Additionally, amongst white dwarfs, the ones showing periodic variations in their luminosity curves are called variable white dwarfs. They can be classified into three main groups, according to their physical properties and spectral type. ZZ Ceti stars (or DAV white dwarfs) are variable white dwarfs with hydrogen-rich atmospheres, V777 Her stars (or DBV white dwarfs) and GW Vir stars (or DOV white dwarfs) are variable white dwarfs with hydrogen-deficient atmospheres — see Gautschy & Saio (1996) for an excellent review.

Variable DO white dwarfs (DOV), also known as variable PG1159 white dwarfs, are stars which are in an evolutionary phase somewhere between the planetary nebulae phase and the white dwarf cooling phase. They have effective temperatures ranging between  $7.5 \times 10^4$  and  $2 \times 10^5$  K, surface gravities within  $\log g = 5.5$  and 8 and their typical luminosities are  $\log(L/L_\odot) \sim 2$ . One of the basic characteristics of these kind of variable stars is that they exhibit strong abundances of He II, C and O and a complete lack of H. They are commonly believed to end their lives as DB white dwarfs after cooling and sedimentation of the heavier atmospheric elements (Unglaub & Bues 2000). Typical pulsational periods for DOV stars range from 400 s up to 1800 s and all of them can be attributed to  $g$ -modes. The driving mechanism for this modes is thought to be the C and O partial ionization zones (Starrfield et al. 1984).

Variable DB white dwarfs (DBV) have temperatures which range between  $2.2 \times 10^4$  and  $2.4 \times 10^4$  K, surface gravities of  $\log g \sim 8$  and luminosities of  $\log(L/L_\odot) \sim -1.2$ . As it is the case of DOV stars, they exhibit a lack of hydrogen but in this case their atmospheres are made of pure He I and no heavy elements seem to be present. They have typical pulsational periods ranging from 140 s up to 1000 s, which, again, are thought to correspond to  $g$ -modes. In this case, the main pulsational driving mechanism is thought to be the second He partial ionization zone (Bradley & Winget 1994).

Finally, the variable DA stars (DAV or ZZ Ceti) have temperatures which range between  $1.2 \times 10^4$  and  $1.4 \times 10^4$  K, surface gravities of  $\log g \sim 8$  and luminosities of  $\log(L/L_\odot) \sim -2.8$ . Unlike the other two types of variable white dwarfs, DAV stars show large abundances of hydrogen in their spectra. Their typical pulsational periods range between 100 s and 1000 s. In this case the main pulsational driving mechanism is thought to be the partially ionized hydrogen region and, again, all the observed pulsations are thought to correspond to  $g$ -modes (Dolez & Vauclair 1981; Winget et al. 1982)

In chapter 2 we will study in detail the gravitational wave emission of several representative models for each one of the three types of pulsating white dwarfs and we will investigate whether the closest and well studied white dwarfs belonging to each one of the families could be eventually detectable by LISA. In order to do so we will use an up-to-date numerical code to compute the pulsational modes. Once we have all the detailed properties of the pulsational modes we will be able to calculate in detail its gravitational wave emission and the potential interest of the pulsating white dwarfs for the LISA mission will be assessed.

### 1.3 Galactic white dwarf binaries

Another source of gravitational radiation are Galactic close binary systems involving at least one compact object. Binary systems also have a non-zero second time derivative of the quadrupole momentum and the strength of the arising gravitational wave emission is large enough to be detectable by LISA. For instance, consider a system of two white dwarfs of comparable masses  $M$ , and orbital separation  $R$ . The orbital velocity is then given by

$$v \sim \sqrt{\frac{GM}{R}} \quad (1.6)$$

Adopting typical white dwarf masses of  $\sim 1 M_\odot$  and orbital separations of  $\sim 0.04 R_\odot$  — see chapter 3 for details — an associated kinetic energy of  $E_k \sim Mv^2 \sim 10^{50}$  erg is obtained, making close white dwarf binary systems another guaranteed source for LISA. It is believed that there are around 200 million close white dwarf binary systems in our Galaxy. According to Evans et al. (1987) many of those systems

have small enough separations in order to be brought in contact by gravitational wave emission in time scales of  $10^5$  to  $10^{10}$  yrs. These systems in the last few years before the merger phase starts will produce a gravitational wave emission of  $h \simeq 10^{-21}$  with frequencies ranging from 10 to 100 mHz. Hence, the Galactic white dwarf binary population will contribute to generate a gravitational wave background which will extend up to some mHz (Mironowski 1965; Evans et al. 1987; Prince et al. 2007) masking any low-amplitude signal occurring in this frequency region.

The process of formation of close white dwarf binaries involves two mass transfer episodes of the progenitor stars when each of the components of the binary system evolves off the main sequence. Depending on when during the lives of the binary components the mass transfer episodes occur the components may have different core compositions. In particular, we may have He-He systems with a total mass  $M_{\text{tot}} \leq 0.75 M_{\odot}$ , He-CO for those systems with masses within the range  $0.75 M_{\odot} \leq M_{\text{tot}} \leq 1.45 M_{\odot}$ , CO-CO for masses larger than  $M_{\text{tot}} \sim 1.45 M_{\odot}$  and even He-ONe or CO-ONe systems when one of the white dwarfs is a massive one. The fate of all these systems is to merge due precisely to angular momentum loss by gravitational wave radiation. It is expected that during the coalescence of these systems large amounts of gravitational waves will be radiated. As it will be shown in detail in chapter 3, coalescing white dwarf binary systems will emerge out of the confusion noise region eventually becoming detectable events. Thus, studying in detail the coalescence of close white dwarf binary systems is of the maximum interest to produce theoretical waveforms to which the data obtained by LISA can be finally compared.

However, this is not the only reason why close white dwarf binary systems are interesting targets. The coalescence process has been shown to result in a configuration composed by a central compact object surrounded by an accretion disk. For systems whose mass exceeds  $1.4 M_{\odot}$ , if the accretion rate from the disk is moderate enough, a type Ia supernova event becomes the most probable outcome. On the contrary, if the accretion rate is too high, an off-center ignition seems to be unavoidable and an ONe white dwarf turns out to be the most probable outcome. Thus, studying the properties of the final merged configuration also bears important consequences for other astrophysical scenarios.

Nonetheless, type Ia supernova are not the only interesting astrophysical objects which can be attributed to a merger of binary white dwarfs. Recently, there has been an enhanced interest for studying a certain type of white dwarfs, the so-called DAZ white dwarfs. These white dwarfs present hydrogen spectral features, high photospheric metal abundances and, in some cases, a massive circumstellar disk has been found surrounding them. The very high metal abundances cannot be satisfactorily explained by normal white dwarf evolution, since due to their strong gravity, at the typical white dwarf atmospheric temperatures, metals should sink very rapidly in the atmospheres of these white dwarfs. Amongst other possibilities, a merger of white dwarfs has been invoked as a possible explanation (García-Berro et al. 2007).

Finally, for the sake of completeness and despite the fact that this is beyond the scope of the present thesis, it is worth mentioning here that there are still more objects that are attributed to a white dwarf merger. For instance, sdB and RCrB are other examples of possible merger remnants. According to this discussion, we will devote chapter 3 to study the expected gravitational waveforms during the coalescence. In chapter 4 we will discuss the effects of the adopted spatial resolution. To do this a set of high-resolution white dwarf merger simulations will be discussed. We will pay attention not only to the merging process but also to the long term evolution of the remnant system. Finally, in chapter 5 we will demonstrate that possibly one of the observed DAZ white dwarfs with circumstellar disk, GD362, might be the result of a merger of white dwarfs.

## Chapter 2

# The gravitational wave radiation from pulsating white dwarfs

In this chapter the emission of gravitational radiation from pulsating white dwarfs is considered. This is done by using an up-to-date stellar evolutionary code coupled with a state-of-the-art pulsational code. The emission of gravitational waves is computed for a standard  $0.6 M_{\odot}$  white dwarf with a liquid carbon-oxygen core and a hydrogen-rich envelope, for a massive DA white dwarf with a partially crystallized core for which various  $\ell = 2$  modes have been observed (BPM 37093) and for PG 1159–035, the prototype of the GW Vir class of variable stars, for which several quadrupole modes have been observed as well. We find that these stars do not radiate sizeable amounts of gravitational waves through their observed pulsation  $g$ -modes, in line with previous studies. We also explore the possibility of detecting gravitational waves radiated by the  $f$ -mode and the  $p$ -modes. We find that in this case the gravitational wave signal is very large and, hence, the modes decay very rapidly. We also discuss the possible implications of our calculations for the detection of gravitational waves from pulsating white dwarfs within the framework of future space-borne interferometers like LISA.

### 2.1 Introduction

Despite its potential interest, the emission of gravitational waves by pulsating white dwarfs has been little explored up to now. Apart from the pioneering work of Osaki & Hansen (1973), only the gravitational wave radiation of rotating white dwarfs undergoing quasi-radial oscillations has been studied so far — see Benacquista et al. (2003) and references therein. White dwarfs are the most common end-point of the evolution of low- and intermediate-mass stars. Hence, white dwarfs constitute, by far, the most numerous stellar remnants in our Galaxy, outnumbering neutron stars. Moreover, the relative simplicity of their physics allows us to obtain very

detailed models which can be ultimately compared with their observed properties. Among white dwarfs there are three specific families of variable stars, known as ZZ Ceti (or DAV, with hydrogen-rich envelopes and  $T_{\text{eff}} \sim 12\,000$  K), V777 Her (or DBV, with helium-rich envelopes and  $T_{\text{eff}} \sim 25\,000$  K) and GW Vir stars (or variable PG 1159 objects, with envelopes which are rich in carbon, oxygen and helium, and  $T_{\text{eff}}$  ranging from  $\sim 80\,000$  to  $150\,000$  K), which show periodic variations in their light curves — see Gautschy & Saio (1995, 1996) for reviews. The typical periods are within  $\sim 100$  s and  $\sim 2\,000$  s and, consequently, lay in the region of frequencies to which LISA will be sensitive. The luminosity changes of these variable stars have been successfully explained as due to nonradial  $g$ -mode pulsations. At present, there is a general consensus that variable white dwarfs are very interesting targets for pulsational studies. Their very simple internal structures allow us to predict theoretically the pulsational frequencies with a very high degree of detail and sophistication. Also, they have a very rich spectrum of frequencies which may give us information about the stellar mass, the core composition, the mass of the surface helium and hydrogen layers (if present), the angular speed of rotation and the strength of the magnetic field — see, for instance, Pfeiffer et al. (1996) and Bradley (1998, 2001), amongst others. Consequently, it is not surprising that in recent years ZZ Ceti and V777 Her white dwarfs, as well as GW Vir stars, have been the preferred targets for the network called the “Whole Earth Telescope” (WET). WET observations have been of an unprecedented quality, and in some cases have allowed us to disentangle the internal structure and evolutionary status of several white dwarf stars by applying the powerful tools of asteroseismology (Nather 1995; Kawaler 1998)

BPM 37093 is the most massive pulsating white dwarf ever found (Kanaan et al. 1992). It is a massive ZZ Ceti star — that is, with a hydrogen-rich atmosphere — with a stellar mass of  $\sim 1.05 M_{\odot}$ , and an effective temperature  $T_{\text{eff}} \simeq 11\,800$  K. BPM 37093 has been thoroughly studied (both theoretically and observationally) because presumably it should have a sizeable crystallized core (Winget et al. 1997). Hence, for BPM 37093 we have detailed models (Montgomery & Winget 1999; Córscico et al. 2005) and extensive observational data (Kanaan et al. 2005). One of the most apparent modes of BPM 37093 has a period  $P = 531.1$  s, very close to the frequency of maximum sensitivity of LISA and pulsates with  $\ell = 2$ . Since  $\ell = 1$  modes do not radiate gravitational waves it turns out that only  $\ell = 2$  modes are relevant for the emission of gravitational waves, thus making BPM 37093 an especially suitable target for LISA. Moreover, the distance to BPM 37093 is known ( $d = 16.8$  pc). Consequently, a detailed study of the possibility of detecting the gravitational waves emitted by this star is of the maximum interest, but still remains to be done. On the other hand, PG 1159–035, the prototype of the GW Vir class of objects, has a complex spectrum with several  $\ell = 2$  modes (Winget et al. 1991). Unfortunately there is no reliable parallax determination for PG 1159–035. Werner et al. (1991) provide  $d \sim 800^{+600}_{-400}$  pc, whereas Kawaler & Bradley (1994) obtained

$d \simeq 400 \pm 40$  pc. However, a spectroscopic determination of its mass ( $M_\star \simeq 0.54 M_\odot$ ) is available. These are, to the best of our knowledge, the only two known white dwarf pulsators with confirmed quadrupole  $g$ -modes.

We have first computed the gravitational waves radiated by a typical  $0.6 M_\odot$  white dwarf with a carbon-oxygen core and a  $10^{-4} M_\star$  hydrogen envelope, which we regard as our fiducial model. For this model white dwarf we first compute the gravitational waves emitted by  $g$ -modes. Then we compute the gravitational waves emitted by BPM 37093 and PG 1159–035, the only two known white dwarfs with quadrupole  $g$ -modes. As it will be shown below, we have found that the fluxes radiated away by these two stars in the form of gravitational waves are very small. This is why we also explore other possibilities. In particular we have also computed the fluxes radiated by the  $f$ - and  $p$ -modes, independently of the lack of observational evidence for these modes in pulsating white dwarfs.

## 2.2 Input physics and method of calculation

### 2.2.1 Nonradial pulsation modes

Unno et al. (1989) and Cox (1980) give details of nonradial stellar pulsations. Here we give a brief overview of the basic properties of nonradial modes. Briefly, nonradial modes are the most general kind of stellar oscillations. There exist two subclasses of nonradial pulsations, namely *spheroidal* and *toroidal* modes. Of interest in this chapter are the spheroidal modes, which are further classified into  $g$ -,  $f$ - and  $p$ -modes according to the main restoring force acting on the oscillations, gravity for the  $g$ - and  $f$ -modes and pressure for the  $p$ -modes.

For a spherically symmetric star, a linear nonradial pulsation mode can be represented as a standing wave of the form  $\Psi'_{k,\ell,m}(r, \theta, \phi, t) = \Psi'_{k,\ell,m}(r) Y_\ell^m(\theta, \phi) e^{i\sigma_{k,\ell,m}t}$ , where the prime indicates a small eulerian perturbation of a given quantity  $\Psi$  (like the pressure, gravitational potential, . . .) and  $Y_\ell^m(\theta, \phi)$  are the corresponding spherical harmonics. Geometrically,  $\ell$  is the number of nodal lines on the stellar surface and  $m$  is the number of such nodal lines in longitude. In the absence of any physical agent able to remove spherical symmetry (like magnetic fields or rotation), the eigenfrequencies  $\sigma_{k,\ell,m}$  are dependent on  $\ell$  but are  $2\ell + 1$  times degenerate in  $m$ .  $\Psi'_{k,\ell,m}(r)$  is the radial part of the eigenfunctions, which for realistic models necessarily must be computed numerically together with  $\sigma_{k,\ell,m}$ . The index  $k$  (known as the radial order of the mode) represents, in the frame of simple stellar models (like those of white dwarf stars which we shall study below), the number of nodes in the radial component of the eigenfunction. Generally speaking,  $g$ -modes are characterized by low oscillation frequencies (long periods) and by displacements of the stellar fluid essentially in the horizontal direction. At variance,  $p$ -modes have high frequencies (short periods) and are characterized by essentially radial displacements of the stellar fluid. Finally, there is a single  $f$ -mode for a given  $\ell$  ( $\geq 2$ ) value. This mode

does not have any node in the radial direction ( $k = 0$ ) and possesses an intermediate character between  $g$ - and  $p$ -modes. Its eigenfrequency lies between that of the low order  $g$ - and  $p$ -modes, and generally slowly increases when  $\ell$  increases. For  $g$ -modes ( $p$ -modes), the larger the value of  $k$  the lower (higher) the oscillation frequency.

### 2.2.2 Numerical codes

We compute the nonradial pulsation modes of the white dwarf models considered in this work with the help of the same pulsational code described in detail in Córscico et al. (2001a, 2002). The code, which is based on a standard finite differences scheme, provides very accurate oscillation frequencies and nonradial eigenfunctions, and has been employed in numerous works on white dwarf pulsations — see, for instance, Córscico et al. (2004) and references therein. The code solves the fourth-order set of equations governing newtonian, linear, nonradial stellar pulsations in the adiabatic approximation following the dimensionless formulation given in Unno et al. (1989). To build up the white dwarf models needed for our pulsational code we employed the LPCODE evolutionary code described in detail in Althaus et al. (2003, 2005b). Our evolutionary code contains very detailed physical ingredients. A full description of these physical ingredients can be found in Althaus et al. (2003, 2005b) where an extensive description of these inputs is done. However, we will summarize here the most important inputs. For instance, the equation of state includes partial ionization, radiation pressure, ionic contributions, partially degenerate electrons and Coulomb interactions. For the white dwarf regime, we include an updated version of the equation of state of Magni & Mazzitelli (1979). The code uses OPAL radiative opacities — including carbon- and oxygen-rich compositions — for arbitrary metallicity from Iglesias & Rogers (1996) and molecular opacities from Alexander & Ferguson (1994). High-density conductive opacities are taken from Itoh et al. (1994) and the references cited there, whereas neutrino emission rates are those of Itoh et al. (1996), and references therein. The stellar models for BPM 37093 and PG 1159–035 discussed below have been derived from full evolutionary calculations that take into account the history of the progenitor stars — see Althaus et al. (2003, 2005b) for details. During the white dwarf cooling phase, the effects of time-dependent element diffusion have been considered in the calculations.

### 2.2.3 Gravitational waves from a pulsating white dwarf

The basic formalism for deriving the gravitational wave radiation of pulsating objects (either white dwarfs or neutron stars) is well known — see, for instance, Osaki & Hansen (1973). We will extend it to the case in which a white dwarf has a partially crystallized core. Generally speaking, the amplitude of a gravitational wave emitted from any slow-moving source in the quadrupole approximation is given by (Misner et al. 1973)

$$h_{ij}^{\text{TT}} = \frac{2G}{c^4 d} \ddot{Q}_{ij}^{\text{TT}}, \quad (2.1)$$

where ‘‘TT’’ stands for the traceless-transverse gauge,  $d$  for the distance, and  $Q$  is the quadrupole moment of the mass distribution, which is defined as

$$Q_{ij} = \int_{R^3} \rho(\vec{r})(3x_i x_j - \delta_{ij} r^2) d^3 r \quad (2.2)$$

As previously stated, we assume that the spatial and temporal behavior of the the perturbed density profile is provided by the following expression:

$$\rho(\vec{r}, t) = \rho_0(r) + \rho'(r) \text{Re} (Y_\ell^m(\theta, \phi) e^{i\sigma t}) \quad (2.3)$$

where  $\rho_0$  is the unperturbed density profile,  $\rho'(r)$  stands for the radial perturbation of the density profile,  $Y_\ell^m(\theta, \phi)$  are the spherical harmonics, and  $\sigma$  is the pulsational frequency. As we are dealing with  $\ell = 2$  modes, and since the emission of gravitational waves in this case will be the same for all the values of  $m$ , we shall choose the simplest case. That is, we adopt  $\ell = 2$  and  $m = 0$ . Additionally, it must be taken into account that BPM 37093 has a sizeable crystallized core. Therefore, the appropriate boundary conditions differ from those of an ordinary star. Particularly, the boundary condition at the stellar center (when crystallization has not yet set in) is that given by Osaki & Hansen (1973). However, when the core of the white dwarf undergoes crystallization we switch the fluid internal boundary conditions to the so-called ‘‘hard sphere’’ boundary conditions (Montgomery & Winget 1999). Within this approximation the nonradial eigenfunctions are inhibited from propagating in the crystallized region of the core. Consequently, and keeping in mind that for the axisymmetric case  $Q_{11} = Q_{22} = -\frac{1}{2}Q_{33}$  and  $Q_{ij} = 0$  if  $i \neq j$  (Osaki & Hansen 1973), the following expression can be easily obtained

$$Q_{33} = \int_0^{2\pi} d\phi \int_0^\pi \sqrt{\frac{5}{16\pi}} \sin \theta (\cos^2 \theta - 1) (3 \cos^2 \theta - 1) d\theta \int_{R_0}^{R_\star} r^4 \rho'(r) \cos(\sigma t) dr \quad (2.4)$$

where  $R_\star$  and  $R_0$  are the stellar radius and the radial coordinate of the crystallization front, respectively. By using Poisson’s equation

$$4\pi G \rho'(r) = \frac{1}{r^2} \frac{d}{dr} \left( r^2 \frac{d\Phi'}{dr} \right) - \frac{6}{r^2} \Phi' \quad (2.5)$$

and Eq. (2.4) it can be shown after a straightforward calculation that the dimensionless strain,  $h_{33}^{\text{TT}}$ , is given by

$$h_{33}^{\text{TT}} \approx 5 \times 10^{-18} \left( \frac{M_\star}{M_\odot} \right) \left( \frac{R_\star}{R_\odot} \right)^2 \left( \frac{\nu}{1 \text{ mHz}} \right)^2 \left( \frac{1 \text{ pc}}{d} \right) \left[ A(R_\star) - F_\mu F_R^2 A(R_0) \right] \cos(\sigma t) \quad (2.6)$$

being  $\nu = 2\pi\sigma$  the frequency of the signal and

$$\begin{aligned} A(r) &\equiv y_4 - 2y_3 \\ y_3 &\equiv \frac{\Phi'}{gr} \\ y_4 &\equiv \frac{1}{g} \frac{d\Phi'}{dr} \\ F_\mu &\equiv \frac{M_0}{M_\star} \\ F_R &\equiv \frac{R_0}{R_\star} \end{aligned} \quad (2.7)$$

In these expressions  $\Phi'$  is the perturbed gravitational potential,  $g$  is the gravitational acceleration at a given radius,  $M_\star$  and  $R_\star$  are the mass and radius of the star, and  $M_0$  and  $R_0$  are the mass and radius of the crystallized core of the white dwarf. Obviously, in the non-crystallized case,  $M_0$  and  $R_0$  are identically zero (corresponding to the stellar center). The advantage of the previously described formalism is that the quantities  $y_3$  and  $y_4$  can be easily tabulated for a typical stellar model, whereas the rest can be observationally obtained. Finally, the luminosity radiated in the form of gravitational waves is (Osaki & Hansen 1973):

$$L_{\text{GW}} \approx 10^{36} \left( \frac{M_\star}{M_\odot} \right)^2 \left( \frac{R_\star}{R_\odot} \right)^4 \left( \frac{\nu}{1 \text{ mHz}} \right)^6 \left[ A(R_\star) - F_\mu F_R^2 A(R_0) \right]^2 \quad (2.8)$$

## 2.3 Results

### 2.3.1 Gravitational wave signal

Fig. 2.1 shows the run, as a function of the mass coordinate, of the functions  $y_3$  — left panels — and  $y_4$  — right panels — discussed in §2.2.3 for the  $g$ -modes of our fiducial model (a typical  $0.6 M_\odot$  white dwarf made of carbon and oxygen with a liquid core and hydrogen envelope of  $10^{-4} M_\star$ ), for BPM 37093 — a massive ( $M_\star \simeq 1.05 M_\odot$ ) white dwarf, with a sizeable crystallized core — and for PG 1159–035, the other

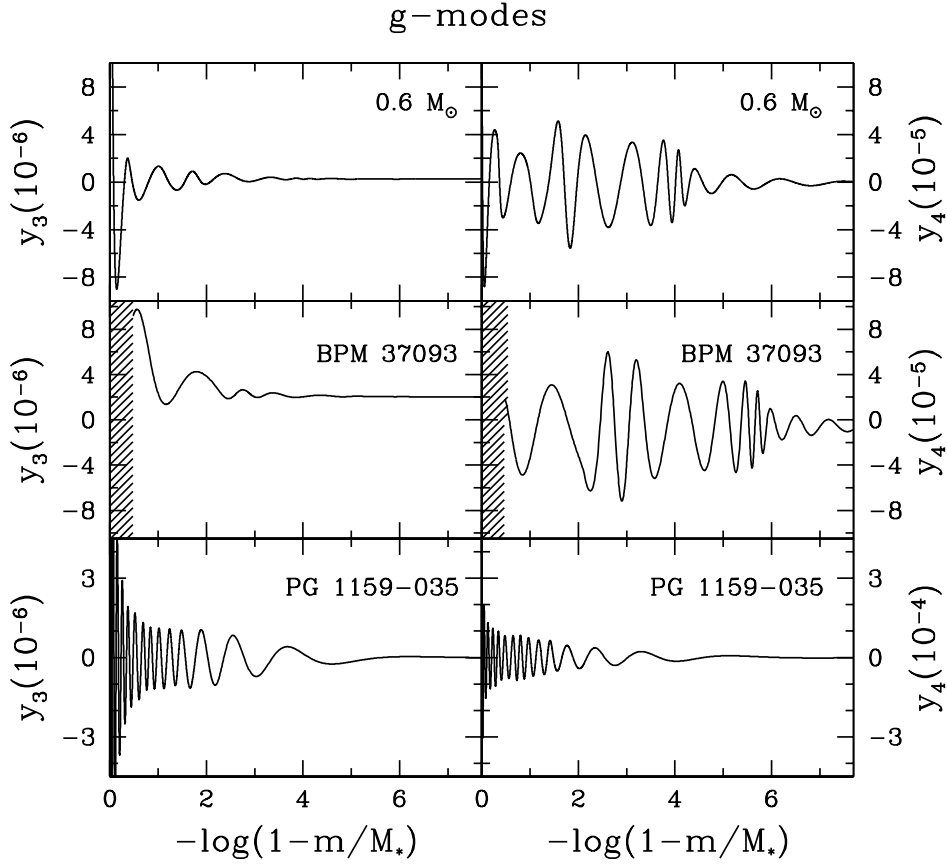


Figure 2.1: Run of the  $y_3$  — left panels — and  $y_4$  — right panels — eigenfunctions for the  $g$ -modes of a typical  $0.6 M_\odot$  white dwarf — top panels — for BPM 37093 — central panels — and for PG 1159-035 — bottom panels — as a function of the mass coordinate  $\log(1 - m/M_*)$ . For the case of BPM 37093 the crystallized core is shown as a hatched area. See text for details.

known white dwarf with unambiguously identified quadrupole  $g$ -modes. The fractional change in radius due to pulsations,  $\delta R_*/R_*$ , must not necessarily be the same for each pulsation mode. However, the linear theory of nonradial pulsations does not provide any indication of the value of the fractional change in radius, since the governing equations are homogeneous and the normalization of the eigenfunctions is arbitrary (Cox 1980). In addition,  $\delta R_*/R_*$  is poorly constrained by the observations, since the luminosity variations of pulsating white dwarfs are almost exclusively caused by changes in temperature, not by their radius variations (Robinson et al.

1982). Thus, we have adopted, somewhat arbitrarily, that the fractional change in radius due to pulsations is  $\delta R_\star/R_\star = 10^{-4}$  for all the considered modes, which is a typical value for pulsating white dwarfs, and reasonably reproduces the amplitude of the observed light curve (Robinson et al. 1982).

We discuss the results obtained for our fiducial model (top panels of Fig. 2.1). We have chosen to display the quadrupole ( $\ell = 2$ )  $g$ -mode with radial order  $k = 25$ , which has a period  $P = 678.22$  s. As can be seen the functions  $y_3$  and  $y_4$  are small everywhere in the star, their amplitudes being of the order of  $\sim 10^{-6}$  and  $\sim 10^{-4}$ , respectively. Moreover, the amplitudes are only significant for the central regions of the white dwarf. For the case of BPM 37093 — central panels — we show the quadrupole  $g$ -mode with  $k = 27$ . This  $g$ -mode has a period  $P = 536.4$  s, which is very close to one of the observed periods,  $P = 531.1$  s. Since BPM 37093 is a massive white dwarf, a sizeable region of its core is crystallized. This region is clearly marked in the central panels of Fig. 2.1 as a shaded area. We note that in this region the amplitudes of both  $y_3$  and  $y_4$  are null. For the PG 1159–035 model — bottom panels — we display the quadrupole mode with  $k = 30$ , which best fits the observed period of  $P = 423.2$  s. This mode has a period  $P = 423.8$  s, thus providing an excellent fit to the observational data.

In Table 2.1 we summarize the most important results for several  $g$ -modes of the models computed so far. We have assumed that all of the observed periods in BPM 37093 and in PG 1159–035 in Table 2.1 are  $\ell = 2$ , following the works by Kanaan et al. (2005) and Winget et al. (1991), respectively. The maximum dimensionless strain,  $h_{\max}$  for BPM 37093 has been computed adopting the measured distance to the source ( $d = 16.8$  pc), whereas for our fiducial model we have adopted a distance  $d = 50$  pc, which we consider to be representative of a typical white dwarf. For the case of PG 1159–035 we have adopted a distance of 400 pc, in line with the determinations of Werner et al. (1991) and Kawaler & Bradley (1994). Column 7 provides the luminosity radiated away in the form of gravitational waves,  $L_{\text{GW}}$ , computed with Eq. (2.8). In the last column of Table 2.1 we list the kinetic energy of each of the modes. In general, the agreement between the computed and the observed periods is rather good for all the modes, both for the case of BPM 37093 and for PG 1159–035. However, the amplitudes of the dimensionless strains are small in all cases. This is also the case for the luminosities radiated away in the form of gravitational waves. In the best of the cases BPM 37093 radiates away  $\sim 10^{19}$  erg/s in the form of gravitational waves, whereas PG 1159–035 radiates away a much more modest amount, only  $\sim 10^{17}$  erg/s.

For our fiducial model — third section of Table 2.1 — the larger the radial order  $k$ , the smaller the dimensionless strain and the smaller the luminosities radiated away in the form of gravitational waves. In particular, an increase from  $k = 1$  to  $k = 10$  produces a reduction of a factor of almost  $4 \times 10^2$  in the dimensionless strain and of  $3 \times 10^6$  in the flux of gravitational waves. The reductions when considering the  $k = 20$  mode are much more modest. This is because low- $k$  modes sample

Table 2.1: Summary of the gravitational wave emission of the  $g$ -modes of BPM 37093 and PG 1159–035. Our fiducial model is also shown for comparison. In all cases we have adopted  $\delta R_\star/R_\star = 10^{-4}$ . The first column lists the model. The second column corresponds to its respective mass. In the third column we show the radial order,  $k$ , of the computed  $g$ -mode. The observed and the computed periods (in seconds) are given in columns 4 and 5, respectively. In column 6 we give the maximum dimensionless strain,  $h_{\max}$ . Column 7 lists the luminosity in the form of gravitational waves and column 8 lists the kinetic energy of the modes.

Model	$M/M_\odot$	$k$	$P_o$ (s)	$P_c$ (s)	$h_{\max}$	$L_{\text{GW}}$ (erg/s)	$\log(E_K)$ (erg)
BPM 37093	1.10	26	511.7	516.7	$4.8 \times 10^{-28}$	$9.2 \times 10^{18}$	46.4
		27	531.1	536.4	$5.4 \times 10^{-28}$	$1.1 \times 10^{19}$	46.5
		28	548.4	555.8	$5.3 \times 10^{-28}$	$9.9 \times 10^{18}$	46.6
		29	582.0	574.9	$6.4 \times 10^{-28}$	$1.3 \times 10^{19}$	46.7
		30	600.7	593.0	$6.4 \times 10^{-28}$	$1.2 \times 10^{19}$	46.8
		32	633.5	630.4	$5.5 \times 10^{-28}$	$8.3 \times 10^{18}$	46.9
PG 1159–035	0.54	25	352.7	358.9	$1.0 \times 10^{-30}$	$5.0 \times 10^{16}$	44.0
		30	423.8	423.2	$2.3 \times 10^{-30}$	$1.7 \times 10^{17}$	43.8
		50	694.9	684.5	$3.5 \times 10^{-31}$	$1.6 \times 10^{15}$	43.4
		55	734.2	752.9	$2.0 \times 10^{-31}$	$4.1 \times 10^{14}$	43.3
		60	812.6	818.1	$1.8 \times 10^{-31}$	$2.8 \times 10^{14}$	43.2
		70	968.7	950.1	$6.0 \times 10^{-32}$	$2.5 \times 10^{13}$	42.8
0.6 $M_\odot$	0.6	1	—	66.6	$6.9 \times 10^{-25}$	$1.0 \times 10^{28}$	47.0
		10	—	310.3	$1.8 \times 10^{-27}$	$3.1 \times 10^{21}$	44.8
		20	—	555.2	$1.5 \times 10^{-27}$	$6.6 \times 10^{20}$	45.1

the core more than high- $k$  modes, and since the core has a higher density, larger mass motions are produced, and hence more gravitational wave losses are produced. Nevertheless, both the dimensionless strains and the fluxes of gravitational waves are in this case much larger than those found for BPM 37093 and PG 1159–035. For the case of BPM 37093 pulsations occur only in a small region of the star as a result of its crystallized core. Thus, despite its mass being much larger than that of our fiducial model, the emission of gravitational waves is strongly inhibited. For the case of PG 1159–035, the most important reason why so few gravitational waves are radiated away is its small mass (and average density).

Given the results obtained for the quadrupole  $g$ -modes studied up to now we ask whether other modes, namely the  $f$ - and  $p$ -modes, of pulsating white dwarfs can radiate away a measurable amount of gravitational waves. Thus, we have extended our calculations to incorporate such modes, despite the lack of observational evidence for them. Obviously, for these modes we do not know the appropriate value of  $\delta R_\star/R_\star$ , since the estimate  $\delta R_\star/R_\star = 10^{-4}$  is based on observed  $g$ -modes in white

Table 2.2: Summary of the gravitational wave emission of the  $f$ - and  $p$ -modes of BPM 37093 and PG 1159–035. Our fiducial model is also shown for the sake of comparison. In all cases we have adopted  $\delta R_*/R_* = 10^{-4}$ . We show the model (first column), its respective mass (second column), the considered mode (third column), the radial order (fourth column), the respective frequency of the mode (fifth column), the dimensionless strain (sixth column), the luminosity radiated away in the form of gravitational waves (seventh column) and the kinetic energy (last column).

Model	$M/M_\odot$	Mode	$k$	$\nu$ (Hz)	$h_{\max}$	$L_{\text{GW}}$ (erg/s)	$\log(E_K)$ (erg)
BPM 37093	1.10	$f$	0	$2.7 \times 10^{-1}$	$6.6 \times 10^{-19}$	$3.4 \times 10^{41}$	49.2
		$p$	1	$9.3 \times 10^{-1}$	$9.1 \times 10^{-20}$	$7.7 \times 10^{40}$	47.8
PG 1159–035	0.54	$f$	0	$4.8 \times 10^{-2}$	$1.2 \times 10^{-22}$	$2.1 \times 10^{35}$	45.5
		$p$	1	$5.9 \times 10^{-2}$	$7.1 \times 10^{-23}$	$5.1 \times 10^{34}$	44.6
$0.6 M_\odot$	0.60	$f$	0	$8.8 \times 10^{-2}$	$5.6 \times 10^{-20}$	$2.3 \times 10^{39}$	47.0
		$p$	1	$1.8 \times 10^{-1}$	$6.4 \times 10^{-21}$	$1.3 \times 10^{38}$	48.6
		$p$	5	$4.6 \times 10^{-1}$	$6.1 \times 10^{-21}$	$7.5 \times 10^{38}$	46.0

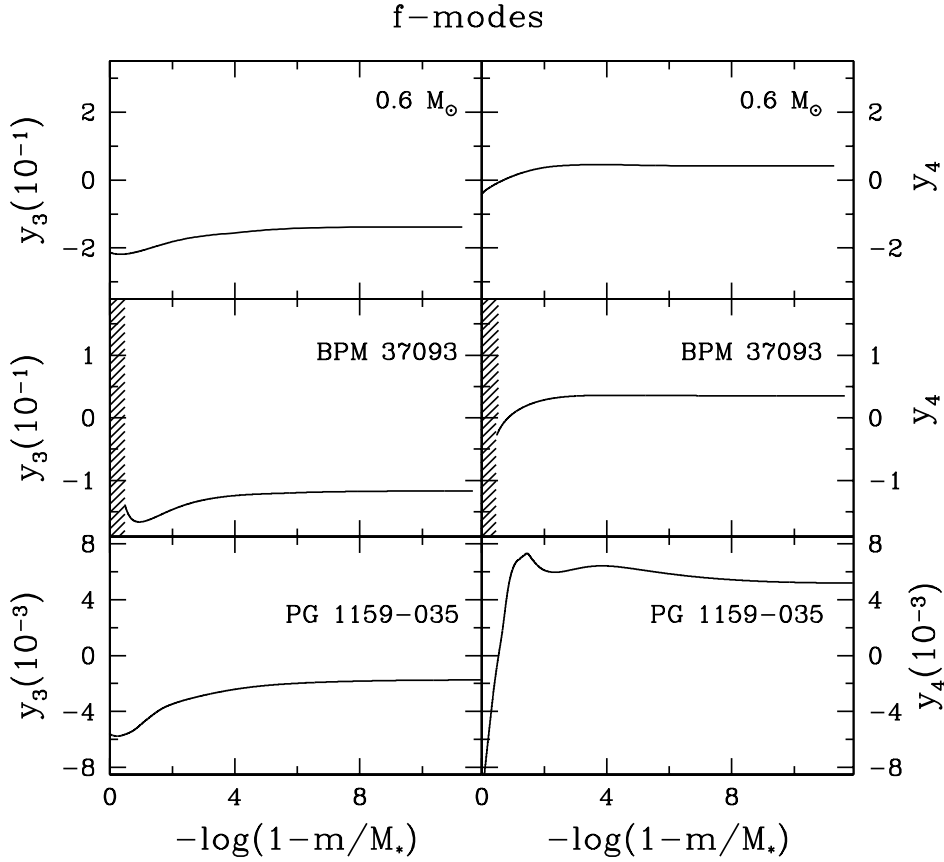


Figure 2.2: Same as Fig. 2.1 for the  $f$ -mode of our  $0.6 M_{\odot}$  fiducial model, for BPM 37093 and for PG 1159–035.

dwarfs. However, for the calculations reported here we adopted the same value. Fig. 2.2 shows the run of the functions  $y_3$  and  $y_4$  for  $f$ -modes of our fiducial model, for BPM 37093 and for PG 1159–035. As is the case for all  $f$ -modes the radial order is zero, and their respective periods are (from top to bottom): 11.35 s, 3.7 s and 20.9 s. The functions  $y_3$  and  $y_4$  are much larger than in the case previously studied. In this case the functions  $y_3$  and  $y_4$  have large amplitudes everywhere and do not vanish at the surface. Consequently, we expect that a large number of gravitational waves can be radiated away. This is indeed the case, as can be observed in Table 2.2. For all the  $f$ -modes of the three models presented here the dimensionless strains are several orders of magnitude larger and, moreover, the luminosities radiated away are much larger than the optical luminosities, even of the order of  $10^{41}$  erg/s in the

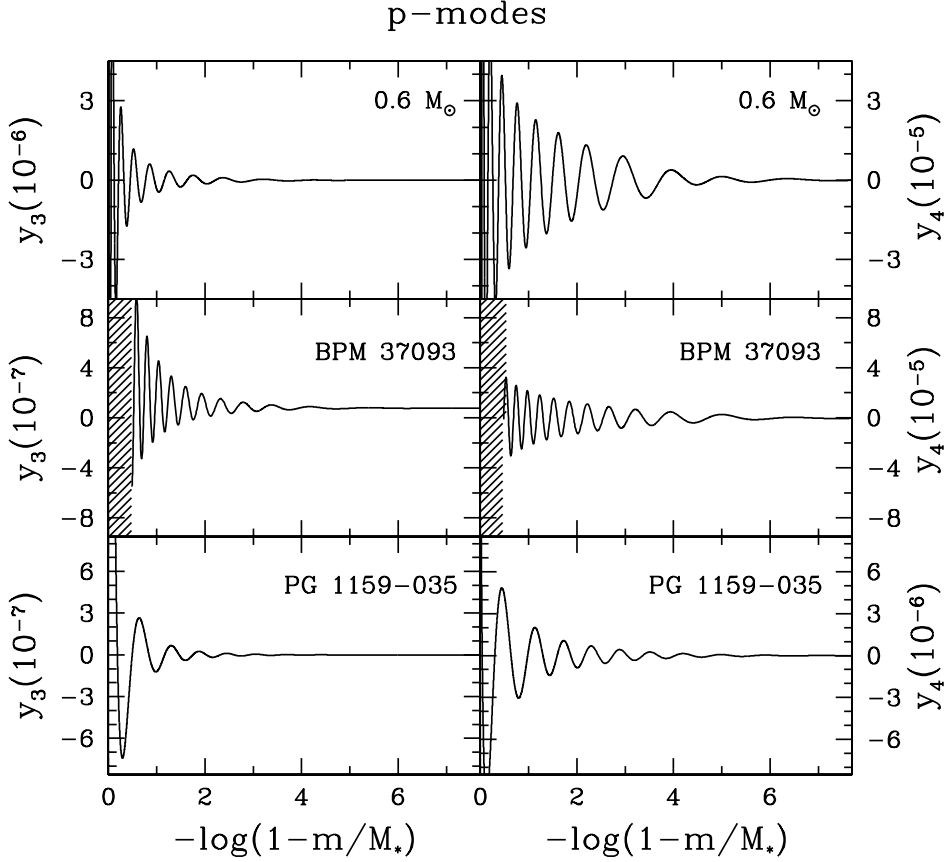


Figure 2.3: Same as Fig. 2.1 for the  $p$ -modes of our  $0.6 M_{\odot}$  fiducial model, for BPM 37093 and for PG 1159–035.

case of BPM 37093. This, in turn, could have important consequences since it could provide one of the possible reasons why these modes have not been observed thus far: if they are excited they are quickly damped by emission of gravitational waves.

Now we turn our attention to the  $p$ -modes. Again, we show the run of the  $y_3$  and  $y_4$  functions of the  $p$ -modes in terms of the mass coordinate for our three models in Fig. 2.3. We have chosen to show the  $k = 25$  mode for all three cases. Their respective periods are  $P = 0.56$  s for our fiducial  $0.6 M_{\odot}$  model,  $P = 0.11$  s for BPM 37093 and  $P = 2.26$  s for PG 1159–035. The amplitudes of the  $y_3$  and  $y_4$  functions for  $p$ -modes are much smaller than those of the corresponding  $f$ -modes, and comparable to the corresponding  $g$ -modes studied before. In addition, in contrast to the situation for the  $f$ -modes, the amplitudes of  $y_3$  and  $y_4$  are almost negligible in regions close to the

surface of the white dwarf. However, because the pulsation frequencies of  $p$ -modes are considerably higher than those of the  $f$ - and  $g$ -modes, the dimensionless strains — see Table 2.2 — are consequently large and the corresponding gravitational wave luminosities are very large as well, although roughly one order of magnitude smaller than those obtained for the  $f$ -modes.

### 2.3.2 Detectability

In order to check whether LISA would be able to detect the pulsating white dwarfs studied here we have assumed that the integration time of LISA will be one year. The signal-to-noise ratio,  $\eta$ , is given by:

$$\eta^2 = \int_{-\infty}^{+\infty} \frac{\tilde{h}^2(\sigma) d\sigma}{S(\sigma) 2\pi} \quad (2.9)$$

where  $S(\sigma) = S_h(\sigma)\tau$  is the sensitivity of LISA,  $\tau$  is the integration period,  $\tilde{h}(\sigma)$  is the Fourier Transform of the dimensionless strain, and  $\sigma$  has been previously defined. It can easily be shown that for a monochromatic gravitational wave  $\eta = h(\sigma)/S_h^{1/2}(\sigma)$ . We have adopted a signal-to-noise ratio  $\eta = 5$ . We have furthermore used the integrated sensitivity of LISA as obtained from <http://www.srl.caltech.edu/~shane/sensitivity>. The results of this procedure are shown in Figs. 2.4, 2.5 and 2.6 for our fiducial model ( $0.6 M_\odot$  carbon-oxygen white dwarf), for BPM 37093 and for PG 1159–035, respectively. In all three figures the  $g$ -modes are shown as circles, the  $f$ -mode is shown as a square and the  $p$ -modes are displayed as triangles. As done previously, for our fiducial model we have adopted a distance of 50 pc, for PG 1159-035 we have assumed a distance of 400 pc, and for BPM 37093 we have used its measured distance (16.8 pc). As can be seen, for none of the three cases studied here will LISA be able to measure the dimensionless strains of the  $g$ -modes, even at a reduced signal-to-noise ratio. Most of the  $p$ -modes will not be observed as well, either because their frequencies are too high to be observed by LISA or because they are too weak. Moreover, given that these modes radiate huge amounts of energy in the form of gravitational waves they become quickly damped and, consequently, it will be very difficult to detect them. Particularly, and given that for the  $p$ -modes studied here the time-averaged dissipation rates of pulsations due to radiative (photons) heat leakage and neutrino losses are much smaller than the luminosity radiated as gravitational waves, an estimate of the damping timescale,  $\tau_d$ , can be easily obtained by considering the kinetic energy of the mode,  $E_K$ , which can be easily computed from our numerical models:

$$\tau_d \simeq \frac{2E_K}{L_{\text{GW}}} \quad (2.10)$$

For instance, for the  $p$ -mode with  $k = 1$  of BPM 37093 one obtains  $\tau_d \simeq 0.5$  yr, which clearly is too short to allow a detection.

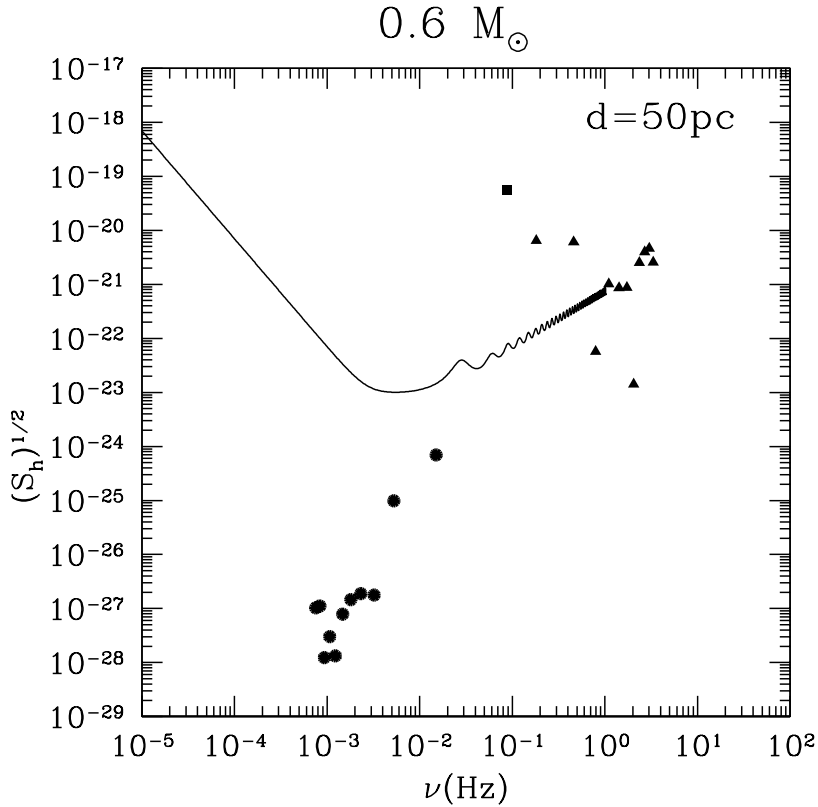


Figure 2.4: A comparison of the signal produced by the quadrupole  $g$ -modes of our fiducial model — circles — by the  $f$ -mode — square — and by the  $p$ -modes — triangles — with the spectral distribution of noise of LISA for a one-year integration period, and assuming that the source is located at 50 pc.

Finally, the three  $f$ -modes of the models presented here lay in the appropriate range of frequencies and, additionally, they are well over the sensitivity curve of LISA. However, as was the case for the  $p$ -modes, they also radiate very large amounts of gravitational waves and, hence, they will be quickly damped, hampering the possibility of detection. In this case we obtain a damping timescale  $\tau_d \simeq 2.9$  yr for the  $f$ -mode of BPM 37093. Although the luminosity radiated away in the form of gravitational waves is larger for the  $f$ -mode than for the  $p$ -mode considered previously, the damping timescale is larger. This is so because the kinetic energies involved are quite different:  $E_K = 1.54 \times 10^{49}$  erg for the  $f$ -mode and  $E_K = 6.42 \times 10^{47}$  erg for the  $p$ -mode with  $k = 1$ . For the sake of completeness we present in Table 2.2 all the relevant information for the  $p$ - and  $f$ -modes that may be detected.

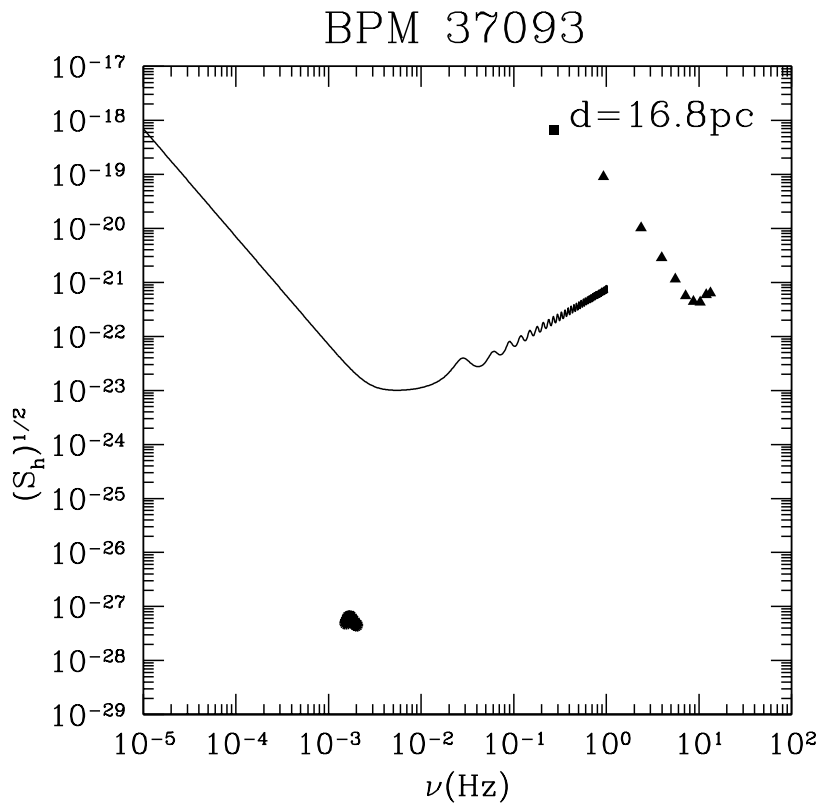


Figure 2.5: Same as Fig. 2.4 for the case of BPM 37093. The distance in this case is known,  $d = 16.8$  pc.

## 2.4 Discussion and conclusions

In this chapter we have computed the gravitational wave emission of pulsating white dwarfs. We have started by computing the gravitational wave radiation of white dwarfs undergoing nonradial  $g$ -mode pulsations, which are currently observed in a handful of pulsating white dwarfs. We have focused on three model stars. Our fiducial model corresponds to an otherwise typical  $0.6 M_{\odot}$  model white dwarf with a carbon-oxygen fluid core and a hydrogen envelope. We have also paid attention to two additional white dwarf models, corresponding to two stars for which quadrupole  $g$ -modes have been observed so far, namely, BPM 37093 and PG 1159–035. We have shown that in these cases the gravitational wave signal is too weak to be observed by future space-borne interferometers, like LISA. We have found that the luminosities in the form of gravitational waves radiated away by these stars and the corresponding dimensionless strains are very small in all the cases, in agreement with the pioneering

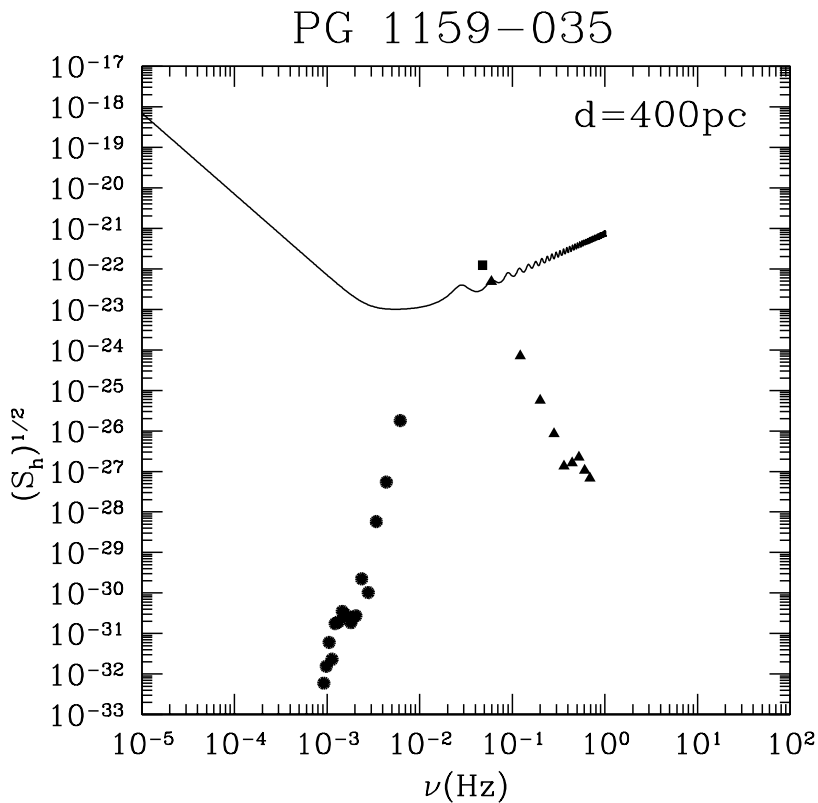


Figure 2.6: Same as Fig. 2.4 for the case of PG 1159–035. Since the distance to PG 1159–035 is not accurately known we have adopted  $d = 400$  pc, which is a reasonable estimate.

work of Osaki & Hansen (1973). Hence, all these sources contribute to the Galactic noise and no individual detections are expected, despite the proximity of the sources. For completeness we have computed the gravitational wave emission of white dwarfs undergoing nonradial  $f$ - and  $p$ -mode oscillations, even if these modes have not been observationally detected. We have found that for white dwarfs undergoing this kind of pulsation the luminosities in the form of gravitational waves radiated away are very large in all the cases, in line with the earlier results of Osaki & Hansen (1973). Consequently, these modes, if excited, should be very short-lived, thus hampering their eventual detection.

It may seem that for the case of pulsating white dwarfs undergoing  $g$ -mode oscillations there could still be a possibility of *indirect detection* by measuring the secular rate of change of the period of the observed modes. However, this is not the case. The secular rate of change of the period of a pulsating white dwarf is given by

$$\frac{\dot{P}}{P} = -a \frac{\dot{T}}{T} + b \frac{\dot{R}_*}{R_*} \quad (2.11)$$

where  $T$  is the temperature of the isothermal core and  $a$  and  $b$  are constants of order unity which depend on the chemical composition, thicknesses of the H atmosphere and He buffer, equation of state, and other ingredients involved in the modeling of white dwarfs. For DA white dwarfs in the ZZ Ceti instability strip, the second term of the right hand side of Eq. (2.11) is usually negligible and, thus, the secular rate of change of the period only reflects the speed of cooling — see, for instance, Isern et al. (1992) and references therein — whereas for GW Vir stars this term is relevant, but can be accounted for by the theoretical models and, hence, the speed of cooling can also be derived. However, any additional source of cooling — like gravitational waves — would eventually translate into an anomalous rate of period change (Isern et al. 1992)

$$\frac{\dot{P}_o}{\dot{P}_c} - 1 = \frac{L_{\text{GW}}}{L + L_\nu} \quad (2.12)$$

where  $P_o$  is the observed period,  $P_c$  is the computed period without taking into account the emission of gravitational waves,  $L_\nu$  is the neutrino luminosity — which is important for hot white dwarfs — and the rest of the symbols are as previously defined. The rate of secular period change has been measured for some pulsating white dwarfs. Particularly, for G117-B15A (Kepler et al. 2000) it has been possible to measure the secular variation of the main observed period of 215.2 s,  $\dot{P} = (2.3 \pm 1.4) \times 10^{-15} \text{ s s}^{-1}$ , with unprecedented accuracy. This white dwarf is the most stable optical clock known, and has been used to pose tight constraints on the mass of the axion (Córscico et al. 2001b) and the rate of variation of gravitational constant (Benvenuto et al. 2004). Other pulsating white dwarfs — like L 19-2 and R 548 — also have determinations of the secular rate of period change but are not as accurate as that of G117-B15A. Note, however, that for a  $0.6 M_\odot$  white dwarf undergoing quadrupole  $g$ -mode oscillations with a period of  $P \sim 200$  s the right hand side of Eq. (2.12) is  $2 \times 10^{-10}$  and  $P_c \sim 10^{-15} \text{ s s}^{-1}$ . In other words the gravitational radiation will produce a change in  $\dot{P} \sim 10^{-25} \text{ s s}^{-1}$ , making impossible such an indirect detection even if accurate observational data and reliable theoretical models eventually become available. Again, the only case of interest here would be the case in which  $L_{\text{GW}} \sim L + L_\nu$ , which may be true for the  $f$ - and  $p$ -mode pulsators.



## Chapter 3

# Gravitational wave radiation from the coalescence of white dwarfs

In this chapter we compute the emission of gravitational radiation from the merging of a close white dwarf binary system. This is done for a wide range of masses and compositions of the white dwarfs, ranging from mergers involving two He white dwarfs, mergers in which two CO white dwarfs coalesce to mergers in which a massive ONe white dwarf is involved. In doing so we follow the evolution of binary system using a Smoothed Particle Hydrodynamics code. Even though the coalescence process of the white dwarfs involves considerable masses, moving at relatively high velocities with a high degree of asymmetry we find that the signature of the merger is not very strong. In fact, the most prominent feature of the coalescence is that in a relatively small time scale (of the order of the period of the last stable orbit, typically a few minutes) the sources stop emitting gravitational waves. We also discuss the possible implications of our calculations for the detection of the coalescence within the framework of future space-borne interferometers like LISA.

### 3.1 Introduction

As already mentioned, one of the most promising sources of gravitational waves are galactic binary systems containing at least one compact object. Galactic binaries, such as neutron stars binaries, cataclysmic binaries or close white dwarf binaries, are guaranteed sources for LISA (Mironowski 1965; Evans et al. 1987), provided that the sources are at sufficiently close distances. In fact, emission from Galactic close white dwarf binary systems is expected to be the dominant contribution to the background noise in the low frequency region, which ranges from  $\sim 10^{-3}$  up to  $\sim 10^{-2}$  Hz (Bender 1998). Additionally, from very simple considerations about the initial mass function,

it is easy to see that galactic close white dwarf binaries must be quite common (Hils et al. 1990) and, consequently, if the amplitude of the gravitational waves is large enough we should be able to eventually detect them during the operation of LISA. Moreover, the merging of two white dwarfs by emission of gravitational radiation will be the final destiny of a good fraction of this type of binary systems. Since during the merging process a sizeable amount of gravitational waves is expected to be produced (Guerrero et al. 2004) it is important to characterize which would be the gravitational wave emission of such process and to assess the feasibility of detecting them.

The process of formation of close white dwarf binaries involves two mass transfer episodes of the progenitor stars when each of the components of the binary system evolves off the main sequence. Depending on when during the lives of the binary components the mass transfer episodes occur the components may have different core compositions. In particular, we may have He-He systems with a total mass  $M_{\text{tot}} \leq 0.75 M_{\odot}$ , He-CO for those systems with masses within the range  $0.75 M_{\odot} \leq M_{\text{tot}} \leq 1.45 M_{\odot}$ , CO-CO for masses larger than  $M_{\text{tot}} \sim 1.45 M_{\odot}$  and even He-ONe or CO-ONe systems when one of the white dwarfs is a massive one. Although the astrophysical scenarios in which a merger of two white dwarfs in a close binary system can occur and their relative frequencies have been relatively well studied — see, for instance, Yungelson et al. (1994), and Nelemans et al. (2001a,b), and references therein — the process of merging itself has received little attention until very recently. Indeed, one of the probable reasons for this lack of theoretical models is the heavy computational demand involved in the simulation of an intrinsically three-dimensional phenomenon. However, in sharp contrast, the coalescence of two neutron stars has been extensively studied — see, for instance, Rosswog et al. (2000), Rosswog & Davies (2002), and Rosswog & Liebendörfer (2003), and references therein, for some of the most recent works on this subject.

In a recent paper (Guerrero et al. 2004) the merging of white dwarf binary systems was thoroughly studied for a wide range of masses and compositions. In doing this an up-to-date *Smoothed Particle Hydrodynamics* code was used. This method was first proposed by Lucy (1977) and, independently, by Gingold & Monaghan (1977). The fact that the method is totally Lagrangian and does not require a grid makes it specially suitable for studying an intrinsically three-dimensional problem like the coalescence of two white dwarfs. In this chapter we will not discuss the simulations presented there, and we defer the description of the SPH code to chapter 4. Also, a full description of SPH techniques can be found in appendix A. Instead, in this chapter we will concentrate on the expected gravitational emission from the merging of two white dwarfs using the results of the SPH calculations of Guerrero et al. (2004).

### 3.2 Gravitational wave emission in SPH

We compute the gravitational wave emission in the slow-motion, weak-field quadrupole approximation (Misner et al. 1973). The dimensionless wave strain,  $h$ , in the transverse-traceless gauge is given by:

$$h_{jk}^{\text{TT}}(t, \mathbf{x}) = \frac{2G}{c^4 d} \frac{\partial^2 Q_{jk}^{\text{TT}}(t - R)}{\partial t^2} \quad (3.1)$$

where  $t - R = t - d/c$  is the retarded time,  $d$  is the distance to the observer and  $Q_{jk}^{\text{TT}}(t - R)$  is the reduced quadrupole moment of the mass distribution, which is given by:

$$Q_{jk}^{\text{TT}}(t - R) = \int \rho(\mathbf{x}, t - R) \left( x^j x^k - \frac{1}{3} x^2 \delta_{jk} \right) d^3 x \quad (3.2)$$

The rest of the symbols have their usual meaning. It is useful to express the time derivative of the quadrupole moment in the following way (Nakamura & Oohara 1989):

$$\ddot{Q}_{jk}^{\text{TT}}(t - R) = P_{ijkl}(\mathbf{N}) \int d^3 x \rho [2v^k v^l - x^k \partial^l \phi - x^l \partial^k \phi] \quad (3.3)$$

where

$$\begin{aligned} P_{ijkl}(\mathbf{N}) &\equiv (\delta_{ij} - N_i N_j)(\delta_{kl} - N_k N_l) \\ &\quad - \frac{1}{2}(\delta_{ij} - N_i N_j)(\delta_{kl} - N_k N_l) \end{aligned} \quad (3.4)$$

is the transverse-traceless projection operator onto the plane orthogonal to the outgoing wave direction,  $\mathbf{N}$ , and  $\phi$  is the gravitational potential. Now, one can express Eq. (3.1) in the following way:

$$h_{jk}^{\text{TT}}(t, \mathbf{x}) = \frac{G}{c^4 d} (A_+(t, \mathbf{x}) \mathbf{e}_{+jk} + A_\times(t, \mathbf{x}) \mathbf{e}_{\times jk}) \quad (3.5)$$

where the polarization tensor coordinate matrices are defined as:

$$\begin{aligned} \mathbf{e}_{+jk} &= \frac{1}{\sqrt{2}} [(\mathbf{e}_x)_j (\mathbf{e}_x)_k - (\mathbf{e}_y)_j (\mathbf{e}_y)_k] \\ \mathbf{e}_{\times jk} &= \frac{1}{\sqrt{2}} [(\mathbf{e}_x)_j (\mathbf{e}_y)_k + (\mathbf{e}_y)_j (\mathbf{e}_x)_k], \end{aligned} \quad (3.6)$$

the dimensionless amplitudes  $h_+ \equiv A_+/d$  and  $h_\times \equiv A_\times/d$  are the two independent modes of polarization in the transverse-traceless gauge, and the amplitudes are respectively given by

$$A_+(t, \mathbf{x}) = \ddot{Q}_{xx} - \ddot{Q}_{yy}, \quad A_\times(t, \mathbf{x}) = +2\ddot{Q}_{xy} \quad (3.7)$$

for  $i = 0$ , and

$$A_+(t, \mathbf{x}) = \ddot{Q}_{zz} - \ddot{Q}_{yy}, \quad A_\times(t, \mathbf{x}) = -2\ddot{Q}_{yz} \quad (3.8)$$

for  $i = \pi/2$ .

In our case we have a collection of  $n$  individual SPH particles. Consequently, Eq. (3.3) must be discretized and it is computed according to the following expression:

$$\begin{aligned} \ddot{Q}_{jk}^{\text{TT}}(t - R) \approx & P_{ijkl}(\mathbf{N}) \sum_{p=1}^n m(p) [2\mathbf{v}^k(p)\mathbf{v}^l(p) \\ & + \mathbf{x}^k(p)\mathbf{a}^l(p) + \mathbf{x}^l(p)\mathbf{a}^k(p)] \end{aligned} \quad (3.9)$$

Where  $m(p)$  is the mass of each SPH particle, and  $\mathbf{x}(p)$ ,  $\mathbf{v}(p)$  and  $\mathbf{a}(p)$  are, respectively, its position, velocity and acceleration.

### 3.3 Calibration and consistency checks

We have done two tests, gravitational wave emission from a single, isolated star, and gravitational wave emission from a close white dwarf binary system in a circular orbit. For both cases there exist analytical solutions to which we can compare our numerical results. In the first case, we have followed the time evolution of an isolated  $1 M_\odot$  star using  $2 \times 10^4$  SPH particles of the same mass. For the second test we have followed the evolution of a binary system made of two white dwarfs of the same mass ( $1 M_\odot$ ) in a circular orbit. Each one of the white dwarfs was simulated using  $2 \times 10^4$  SPH particles of the same mass.

The first of our tests was designed to set the zero point of our calculations. Since in SPH simulations the particles are allowed to move freely under the action of their own gravitational potential and of the pressure forces, and since the mass of each particle is relatively large it is not obvious *a priori* whether or not a stable relaxed configuration radiates gravitational waves. Figure 3.1 shows the dimensionless strains for the case of an isolated white dwarf. We only show times larger than 60 s, for which the star is already relaxed to its final configuration. The relaxation procedure consisted in allowing the initial configuration (which consisted in randomly distributing the SPH particles according to the density profile of a zero temperature white dwarf of the same mass) to evolve for a long enough time until the oscillations of the resulting configuration were completely negligible. In this way we check whether or not the numerical noise produces a negligible emission of gravitational waves. And this is indeed the case. As it can be seen the emission of gravitational

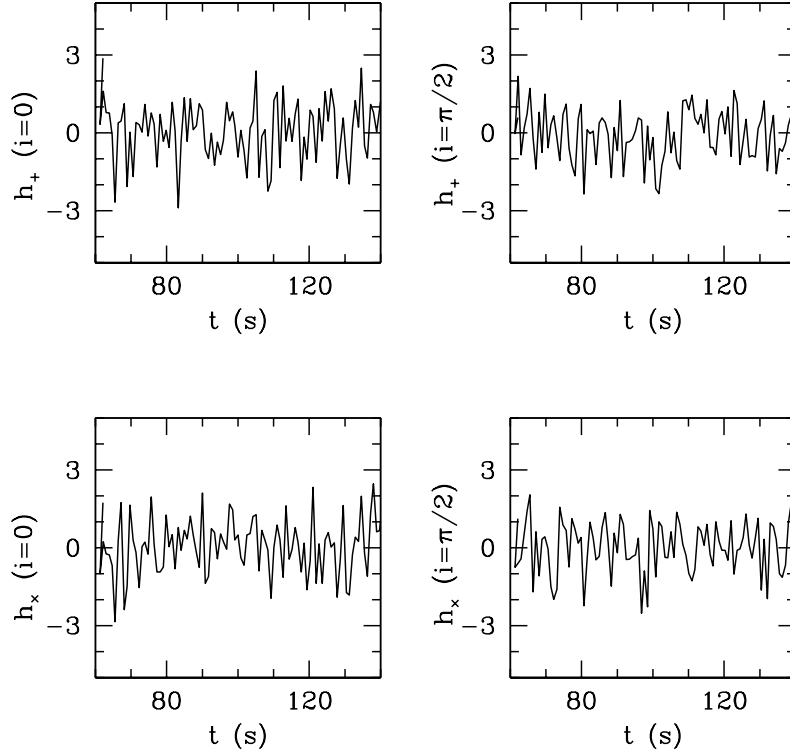


Figure 3.1: Gravitational wave emission from an isolated, spherical star. The dimensionless strains  $h_+$  and  $h_\times$  are measured in units of  $10^{-25}$ . The source is located at a distance of 10 kpc.

waves is negligible, as it should be, given that the relaxed configuration presents spherical symmetry — see Eq. (3.2).

With regard to the second test, it is worth recalling that the emission of gravitational waves from a binary system, can be obtained quite easily by assuming that both stars are point-like mass distributions. By doing so, from Eqs. (3.1) and (3.2) one obtains

$$h_+ = \sqrt{2} \frac{\mu}{d} \frac{G^{\frac{5}{3}}}{c^4} (\omega M_{\text{tot}})^{\frac{2}{3}} (1 + \cos^2 i) \cos 2\omega t \quad (3.10)$$

and

$$h_\times = 2\sqrt{2} \frac{\mu}{d} \frac{G^{\frac{5}{3}}}{c^4} (\omega M_{\text{tot}})^{\frac{2}{3}} (\cos i) \sin 2\omega t, \quad (3.11)$$

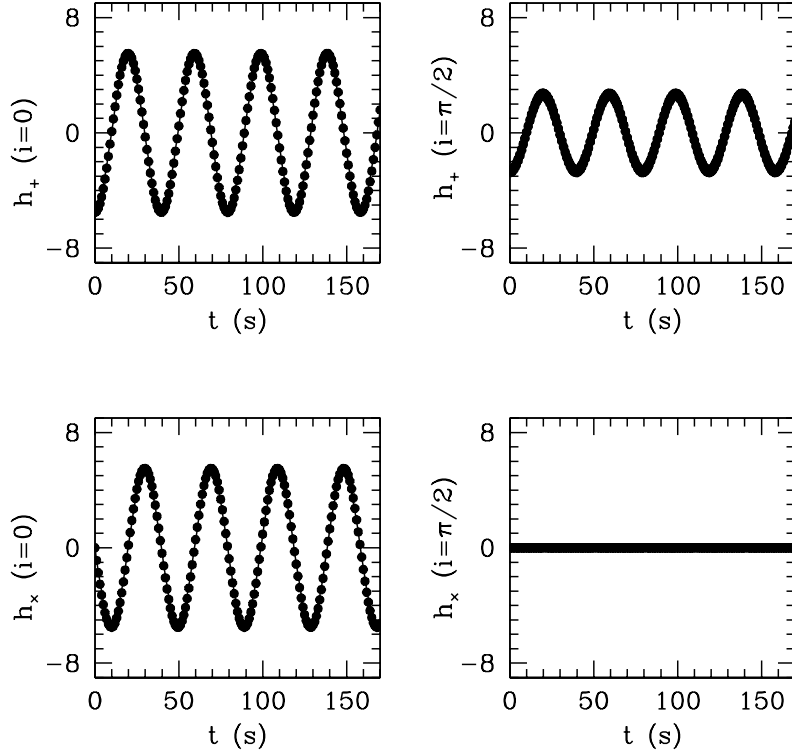


Figure 3.2: Gravitational wave emission from a close white dwarf binary system. The dimensionless strains  $h_+$  and  $h_\times$  are measured in units of  $10^{-22}$ . The solid line corresponds to the theoretical solution whereas the dots correspond to our numerical solution. Again, the source is assumed to be at a distance of 10 kpc.

where  $\omega$  is the angular velocity of the stars,  $\mu$  is the reduced mass,  $M$  is the mass of the white dwarfs, and  $i$  is the observation angle with respect to the orbital plane.

In our SPH simulations we have chosen the binary system to have a separation of  $0.05 R_\odot$  or, equivalently,  $\omega = 7.94 \times 10^{-2} \text{ s}^{-1}$ . The two white dwarfs describe circular orbits and no mass is transferred between both components. Moreover, the two white dwarfs preserve their initial spherical symmetry. Hence, and according to Eqs. (3.10) and (3.11), we should expect to obtain dimensionless strains which are sinusoidal functions with a period equal to half of the orbital period. As it can be seen from Figure 3.2, the numerical solution matches very well the theoretical one. In particular, both the amplitude and the frequency ( $\nu \simeq 0.025 \text{ Hz}$ ) show an excellent agreement between theory and simulations. To further illustrate this overall excellent agreement, in Figure 3.3 we show the residuals between the theoretical solution and

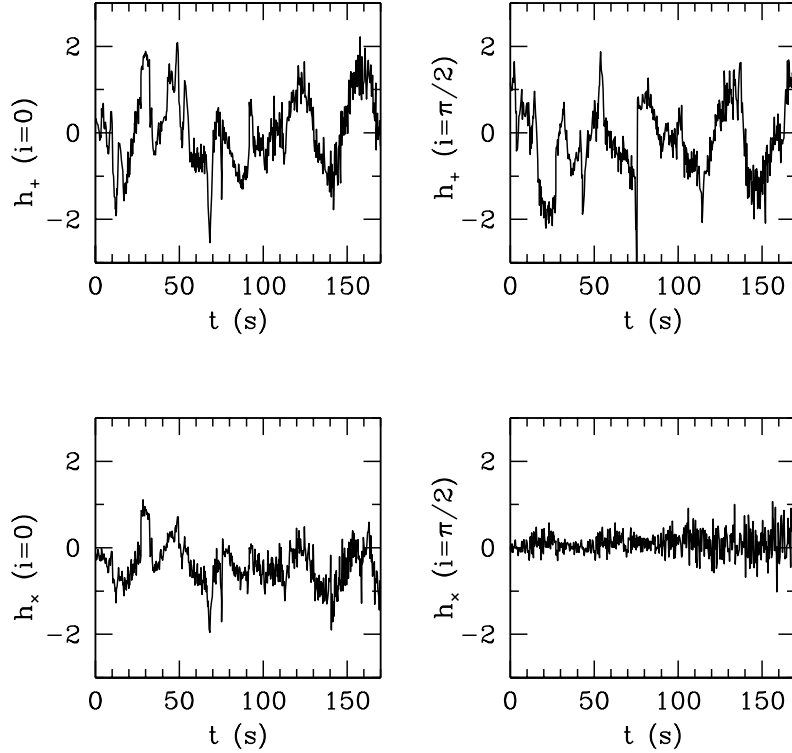


Figure 3.3: Residuals between the theoretical solution and the gravitational wave emission from the close white dwarf binary system of Fig. 3.2. Note that the dimensionless strains  $h_+$  and  $h_x$  are measured in units of  $10^{-23}$ , one order of magnitude smaller than the scale of Fig. 3.2.

the gravitational wave emission of the close white dwarf binary system in circular orbit. Note that the scale in this case is one order of magnitude smaller than that of Figure 3.2. Hence, we conclude that our SPH simulations can accurately compute the emission of gravitational waves from coalescing white dwarfs.

## 3.4 Results

### 3.4.1 Gravitational wave emission

We have computed the emission of gravitational waves resulting from the merging of several close white dwarf binary systems. In particular, the radiation of gravitational waves from a  $0.4+0.4 M_\odot$  He-He system, a  $0.4+1.2 M_\odot$  He-ONE close binary,

Table 3.1: Summary of the simulations discussed in this chapter. The number of SPH particles for the simulations of the first section of the table is  $4 \times 10^4$ , whereas for the last simulation is  $4 \times 10^5$ .

Run	$M_{\text{tot}} (M_{\odot})$	Composition	$R_0 (R_{\odot})$	$t$ (s)
1	0.4+1.2	He/ONe	0.040	180
2	0.4+0.4	He/He	0.042	600
3	0.6+0.6	CO/CO	0.041	180
4	0.6+1.0	CO/CO	0.038	725
5	0.6+0.8	CO/CO	0.033	600
6	0.8+1.0	CO/CO	0.028	1000
7	0.6+0.6	CO/CO	0.040	90

a 0.6+0.8 double white dwarf, a 0.6+1.0 system and a 0.8+1.0  $M_{\odot}$  CO-CO binary system was computed. All the simulations performed so far are listed in Table 3.1, where the mass of both components of the binary system, their respective composition, the initial separation ( $R_0$ ) and the simulation time can be found. For the sake of conciseness we will only discuss in some detail the results of the 0.4+0.4  $M_{\odot}$  He-He system and of the 0.8+1.0  $M_{\odot}$  CO-CO merger. In all the cases the initial separation was larger than the corresponding Roche lobe radius of the less massive component. For instance, for the case in which a 0.4+0.4  $M_{\odot}$  He-He merger is considered the initial separation was  $\simeq 0.042 R_{\odot}$ , and in the case of a 0.8+1.0  $M_{\odot}$  CO-CO system the initial separation was  $\simeq 0.027 R_{\odot}$ .

Instead of computing self-consistently the chirping phase we have chosen to add a very small artificial radial acceleration term which decreases the separation of both components until the last stable orbit is reached. This acceleration term is proportional to the velocity, never amounts to more than a 5% of the real orbital acceleration and is added once the stars have already done a full orbit, then we let the system relax during another orbit and the whole procedure is repeated again until the secondary fills its Roche lobe. Once the secondary fills its Roche lobe this acceleration term is suppressed and the system is allowed to evolve freely. Nevertheless, we have checked (see §2.3.2) that the amplitude of the gravitational waves during the initial phase of the coalescence agrees with that of the chirping phase. Finally, it is important to mention here that in all the simulations studied in the present work the number of particles for each white dwarf is  $2 \times 10^4$  in all cases. However, and in order to check the sensitivity of our results to the number of particles, we have run an additional simulation in which the number of particles was significantly increased to  $2 \times 10^5$  for each star, this simulation is listed in the last entry of table 3.1 and discussed below.

In Fig. 3.4 we show the temporal evolution of the positions of the SPH particles projected on to the orbital plane as a function of time for the 0.8 + 1.0  $M_{\odot}$  system.

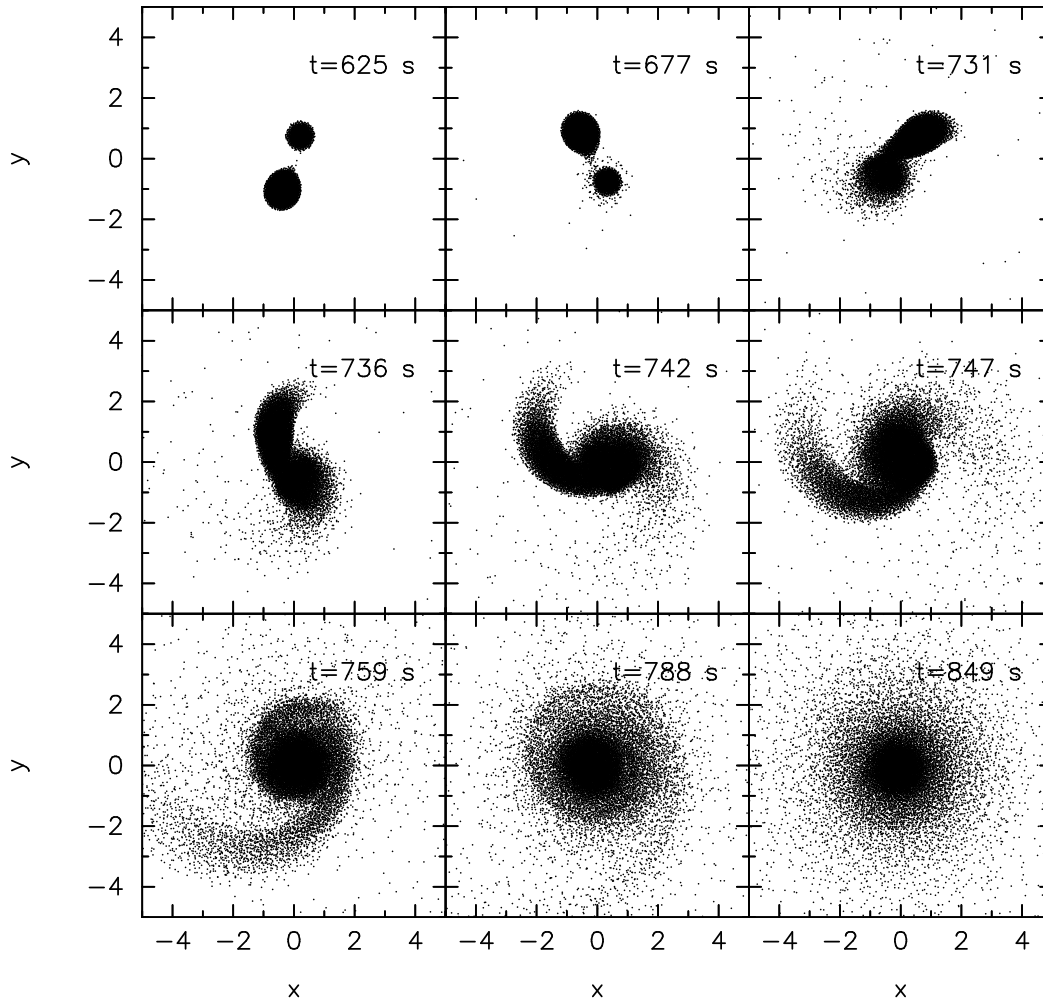


Figure 3.4: Temporal evolution of the  $0.8+1.0 M_{\odot}$  CO-CO close white dwarf binary system during the most important phases of the merger. The SPH particles have been projected in the orbital plane. The units of positions are  $10^9$  cm. See text for additional details.

The initial configuration of the two stars was completely spherically symmetric. After some time the secondary is tidally deformed and begins to overflow its Roche lobe (top left panel). As a consequence, an accretion stream forms (top middle panel). This accretion stream is directed towards the primary, forming an arm. The particles flowing from the secondary onto the primary are redistributed over the surface of the primary (top right panel) and the arm twists as time increases (central panels), leading to the formation of a heavy accretion disk with cylindrical symmetry (bottom right panel). The whole process lasts for about 3.8 minutes. The merging process can be understood in terms of the positive feedback experienced

by the secondary: as the coalescence proceeds the secondary loses mass and, thus, becomes less dense and expands leading to an enhanced mass-loss rate which, in turn, leads to a decrease of the average density of the secondary. Very few particles achieve velocities larger than the escape velocity and, hence, a very small fraction of the total mass is ejected from the system (about  $6.5 \times 10^{-3} M_{\odot}$  in this case). An important feature of the simulation is that the accretion disk is supported by its own rotational velocity. However, it is important to realize that in the final configuration a weak spiral pattern can still be found. This pattern should become less and less apparent as time increases, reaching cylindrical symmetry during the very late stages of the simulation. However, following the long term evolution of this heavy accretion disk would require a heavy computational load which is well beyond our current possibilities. Additionally, the accretion rate onto the primary becomes negligible during this phase. Hence, our final configuration consists in a central rotating spherically symmetric compact star surrounded by a keplerian and almost cylindrically symmetric accretion disk. As discussed in Guerrero et al. (2004) the rotational velocity of the central star has been probably overestimated due to the large shear introduced by SPH methods. We have used the artificial viscosity of Balsara (1995), which does not produce an excessive shear and, consequently, reduces somewhat (but not completely) these problems. Therefore, some properties of the merged object could be affected by the excess of rotation of the primary. However, since even in this case the star preserves spherical symmetry we consider that the calculations described below provide a good approximation to the emission of gravitational waves. All the cases studied present more or less the same features except those in which two white dwarfs of equal mass are involved. In such a case the final configuration is a single spheroidal central object — see, for instance, Fig. 5 of Guerrero et al. (2004).

In figure 3.5 the coalescence of a binary system of  $0.6+0.6 M_{\odot}$  in which each of the stars was modelled using  $2 \times 10^5$  particles is displayed. As in figure 3.4 we have chosen to represent the temporal evolution of the SPH particles projected in the orbital plane. Note, however, that in this case only one out of four particles has been represented. In this case, however, the simulation only covers times larger than that at which the last stable orbit of the system occurs. As it can be seen, the results are essentially the same and, thus, we are confident in the main results and general trends of our numerical simulations. We will, however, come back later to this issue at the end of this section, when discussing the emission of gravitational waves.

An example of our results is shown in figures 3.6 and 3.7, where the dimensionless strains  $h_+$  and  $h_{\times}$  as a function of time for different inclinations are respectively shown for the  $0.8+1.0 M_{\odot}$  CO-CO and the  $0.4+0.4 M_{\odot}$  He-He systems. The beginning and the final time of the merging itself are shown in both figures as thin dotted lines. In figure 3.6 it can be seen that before the coalescence proceeds the emission of gravitational waves still has a sinusoidal pattern, but with an increasing frequency. That is, the close white dwarf binary system chirps as a consequence

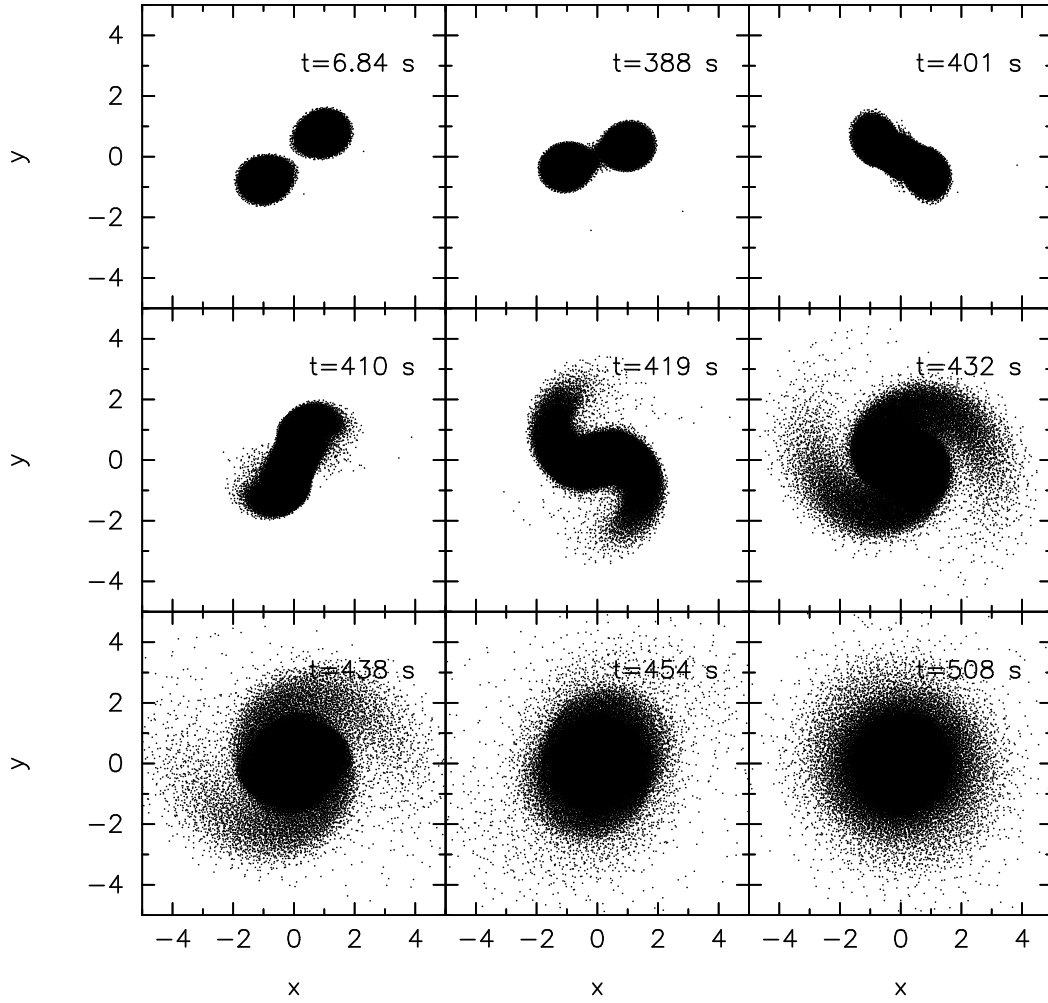


Figure 3.5: Same as figure 3.4 for the  $0.6+0.6 M_{\odot}$  CO-CO close white dwarf binary system in which  $2 \times 10^5$  SPH particles were used. The units of positions are  $10^9$  cm.

of the spiral trajectory of the stars towards the center of mass. Note that  $h_{\times}$  for  $i = \pi/2$  is zero because the orbital plane is parallel to the line of sight. When the two white dwarfs start to coalesce, the amplitude of the dimensionless strains somehow increase first, but only during the first (and most violent) stage of the merger. This corresponds to the phase in which a spiral arm is formed. After the second maximum is achieved the amplitude decreases dramatically. In fact, only two more clear maxima can be apparently distinguished before the system reaches its final configuration. It is interesting to note that once the merger has already finished one of the dimensionless strains still is significant,  $h_{+} \simeq -5 \times 10^{-22}$  at  $d = 10$  kpc for  $i = \pi/2$ . This residual emission is due to the inhomogeneities of the accretion

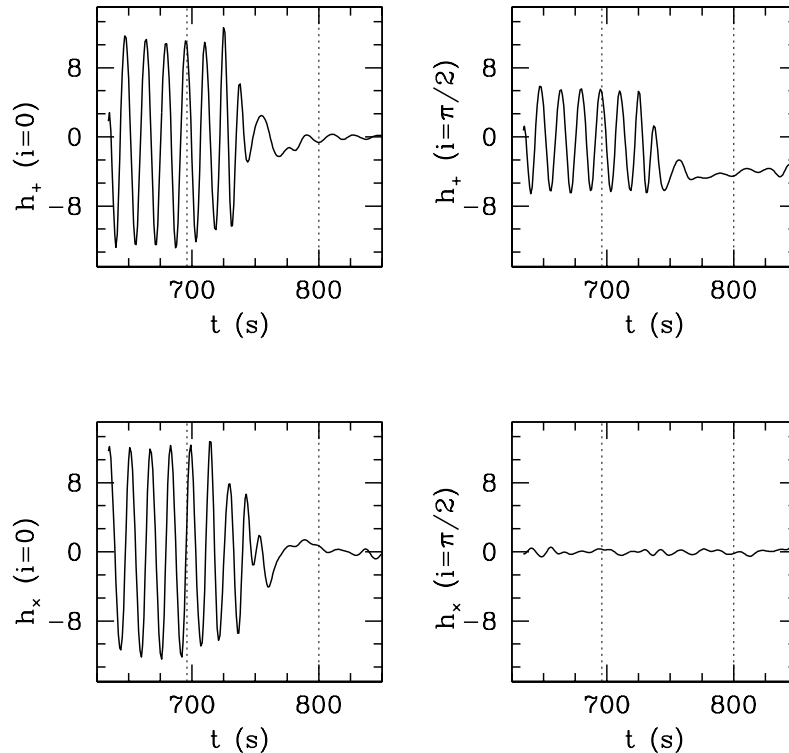


Figure 3.6: Gravitational wave emission from the merger of a  $0.8+1.0 M_{\odot}$  CO-CO close white dwarf binary system. The dimensionless strains  $h_+$  and  $h_{\times}$  are measured in units of  $10^{-22}$ . The leftmost thin dotted line corresponds to the time at which the two white dwarfs start to merge and the rightmost thin dotted line corresponds to the time at which an approximate cylindrical configuration has been already achieved. Again, the source is assumed to be at a distance of 10 kpc.

disk previously discussed. Each one of the very small maxima appearing at very late times corresponds to successive crossings of the edge of the weak spiral arm in front of the line of sight. Note as well that this residual emission tends to disappear asymptotically, as a consequence of the ongoing rehomogenization of the accretion disk. It is important to realize that these inhomogeneities could be either an artifact due to the resolution used in our SPH simulations or a consequence of the adopted artificial viscosity, since it is well known that the artificial viscosity of Balsara (1995) induces a considerable shear viscosity.

In figure 3.7 it can be seen that although during the first part of simulation the same chirping pattern is found, once the merger proceeds the gravitational wave

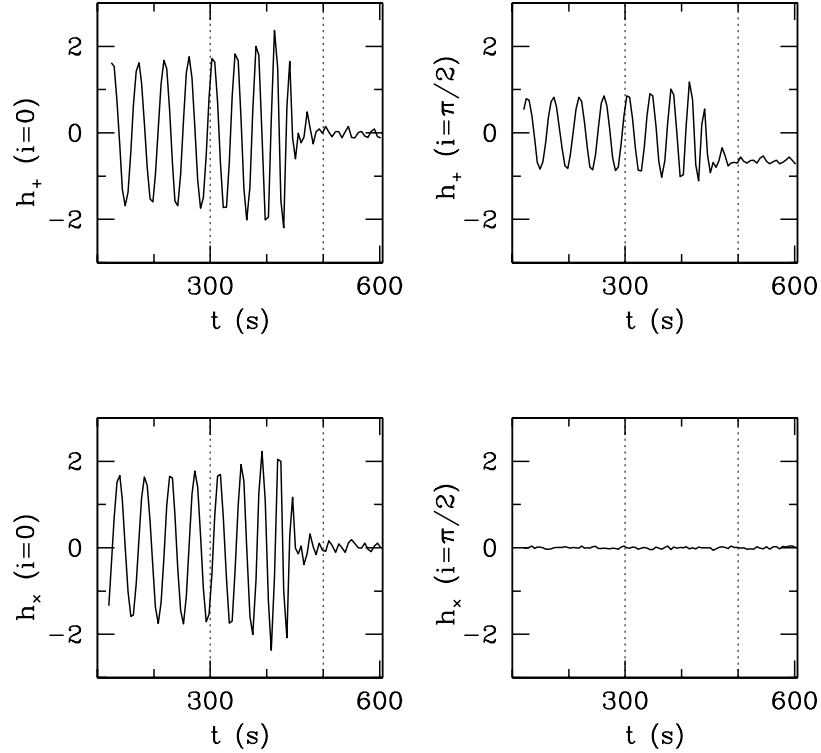


Figure 3.7: Same as Fig. 3.6 but for the case of a  $0.4+0.4 M_{\odot}$  He-He close white dwarf binary system.

signal suddenly disappears on a short time scale, comparable to the orbital period. This is due to the fact that in this case the two stars have equal masses and, therefore, there is not a prominent spiral accretion stream. Instead the two components of the binary system are disrupted around the center of masses, where a shocked region forms as a consequence of the impact between two streams. The typical Mach numbers in the shocked region are  $\text{Ma} \sim 1$ . The streams are slightly asymmetric, depending on the orbital phase at which they form. By the end of the simulation — see again Fig. 5 of Guerrero et al. (2004) — both streams become entangled and the final configuration of the resulting object consists in a central shocked region surrounded by a less dense rotating spheroid, in which a certain degree of asymmetry is still present. Hence, the coalescing process does not present a rather symmetric behavior during the initial phases and, consequently, we see three consecutive maxima. After this, once the streams become entangled the emission of gravitational waves is heavily suppressed and, by the end of the merging process, the emission

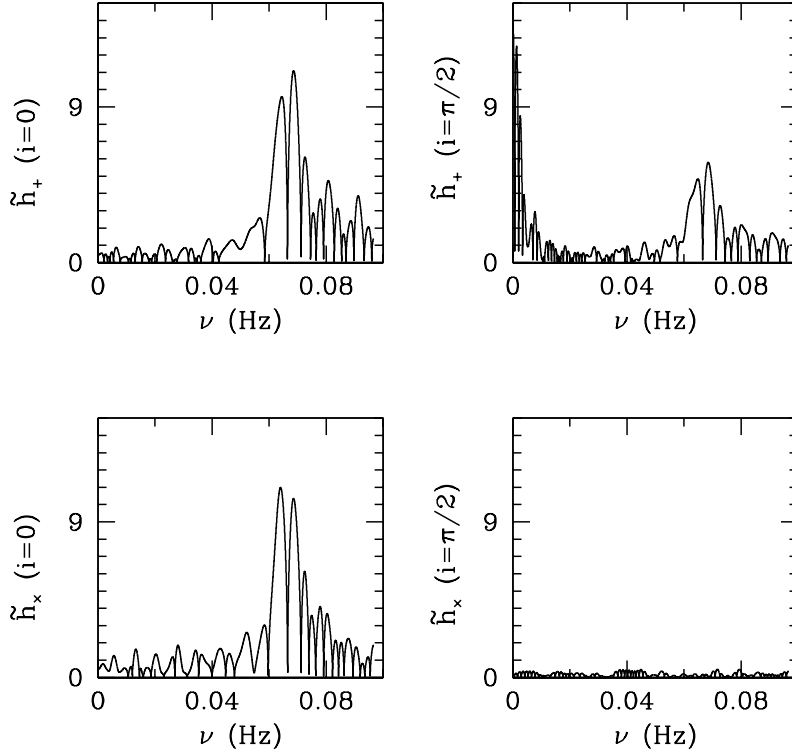


Figure 3.8: Modulus of the Fast Fourier Transform of the adimensional strains  $h_+$  and  $h_x$  of Fig. 3.6.

of gravitational waves is negligible. However, note as well that in this case a small residual emission is also observed in the dimensionless strain  $h_+ = -0.8 \times 10^{-22}$  at  $d = 10$  kpc for  $i = \pi/2$ , although considerably smaller than in the previous case. This is again due to our limited computational resources. The impossibility of following the very late phases of the coalescence episode does not allow us to compute the rehomogenization of the external spheroid and, hence, to compute the long-term behavior of  $h_+$  accurately. The same information is displayed in figures 3.8 and 3.9, but in a different format. As can be seen there, the dominant frequency is given by the orbital period. However, as the components of the binary system approach each other, the dominant frequency is shifted to larger values and, during the merger, high frequencies show up, although with very low amplitudes.

Finally, and in order to check the sensitivity of our results to the resolution of the SPH simulations described above we have computed the emission of gravitational waves for both our run “7”, in which  $2 \times 10^5$  particles were used for each star, and

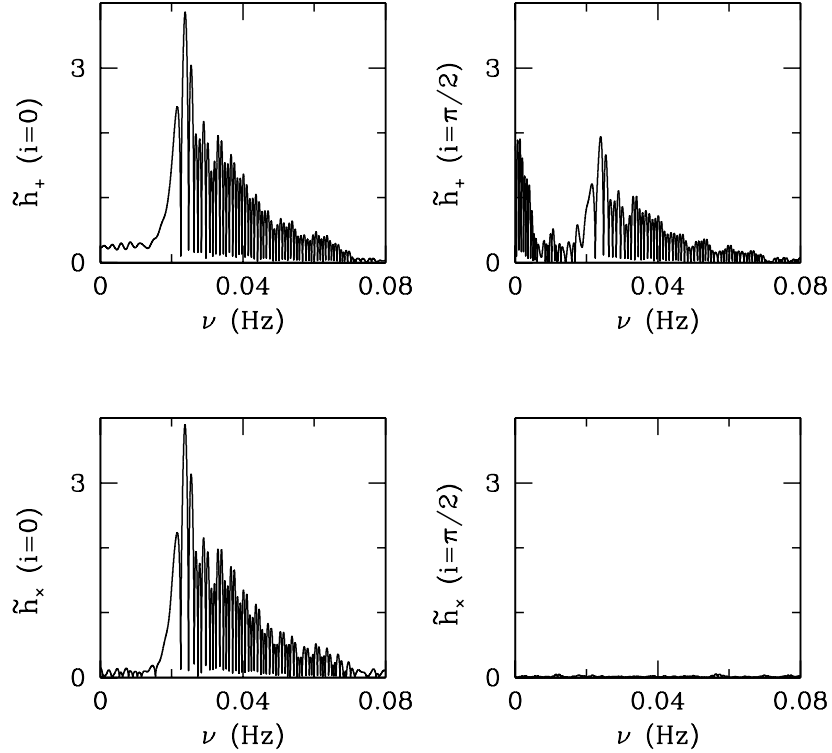


Figure 3.9: Modulus of the Fast Fourier Transform of the adimensional strains  $h_+$  and  $h_x$  of Fig. 3.7.

our run number 3, in which a resolution 10 times poorer was adopted. The results are displayed in Fig. 3.10. As in the previous figures the vertical thin lines denote the moment at which the last stable orbit is achieved. Note, nevertheless, that the high resolution simulation was started, as previously mentioned, when the system was already at the last stable orbit. That is the reason why the chirping phase does not appear. Consequently, the time origin of this simulation has been shifted accordingly to match that of the low resolution simulation. As it can be seen the emission of gravitational waves is very similar in both cases, and, hence, our results are robust.

### 3.4.2 Detectability

In order to check whether or not LISA would be able to detect a close white dwarf binary system we have proceeded as follows. We have already shown that the most

Table 3.2: Maximum distance at which LISA will detect the close white dwarf binary systems discussed in this paper, see text for details.

Run	$M_{\text{tot}}$ ( $M_{\odot}$ )	$\nu_0$ (mHz)	$M$ ( $M_{\odot}$ )	$d_{\text{max}}$ (kpc)	$\eta$ (10 kpc)	$h_{\text{max}}$ ( $10^{-22}$ )	$E$ ( $10^{41}$ erg)
1	0.4+1.2	32	0.59	21	10.5	11.4	6
2	0.4+0.4	21	0.35	10	5.0	2.4	0.1
3	0.6+0.6	13	0.53	26	13.0	6.0	0.6
4	0.6+1.0	34	0.67	29	14.5	6.8	2
5	0.6+0.8	40	0.60	31	15.6	6.1	1
6	0.8+1.0	58	0.77	33	16.6	12.8	7
7	0.6+0.6	13	0.53	26	12.8	5.9	0.6

prominent feature of the emitted signal is its sudden disappearance in a couple of orbital periods and that the gravitational wave emission during the coalescence phase does not increase noticeably. Hence, the gravitational wave emission is dominated by the chirping phase. Thus, we have assumed that the orbital separation of the two white dwarfs is exactly that of our binary system *when mass transfer starts*. We have done so because, as explained before, we have added a small artificial acceleration term to the initial configuration in order to avoid an excessive computational demand at the very beginning of our simulations. This acceleration term is suppressed once the secondary begins to transfer mass onto the primary. Note, however, that the mass transfer starts when the secondary fills its Roche lobe and, consequently, this orbital separation is physically sound. We have further assumed that the integration time of LISA will be one year. We have checked that during this period the variation of the orbital separation is negligible (see also figures 3.6 and 3.7). Of course, should the integration time be smaller the signal-to-noise ratio derived below would be smaller. Consequently, our results should be regarded as an upper limit.

The signal-to-noise ratio,  $\eta$ , is given by

$$\eta^2 = \int_{-\infty}^{+\infty} \frac{\tilde{h}^2(\omega) d\omega}{S(\omega) 2\pi} \tag{3.12}$$

where  $S(\omega) = S_h(\omega)\tau$  is the sensibility of LISA,  $\tau$  is the integration period, and  $\tilde{h}(\omega)$  is the Fourier Transform of the dimensionless strain. It can be easily shown that for a monochromatic gravitational wave  $\eta = h(\omega)/S_h^{1/2}(\omega)$ . The maximum distance,  $d_{\text{max}}$ , at which LISA would be able to detect a close white dwarf binary system is then:

$$d_{\text{max}} \approx 17 \left(\frac{5}{\eta}\right) \left(\frac{M}{M_{\odot}}\right)^{5/3} \left(\frac{\nu_0}{1 \text{ mHz}}\right)^{2/3} \left(\frac{10^{-23}}{\sqrt{S_h(\nu_0)}}\right) \text{ kpc} \tag{3.13}$$

where  $\nu_0$  is the frequency of gravitational wave, and  $M$  is the chirping mass.

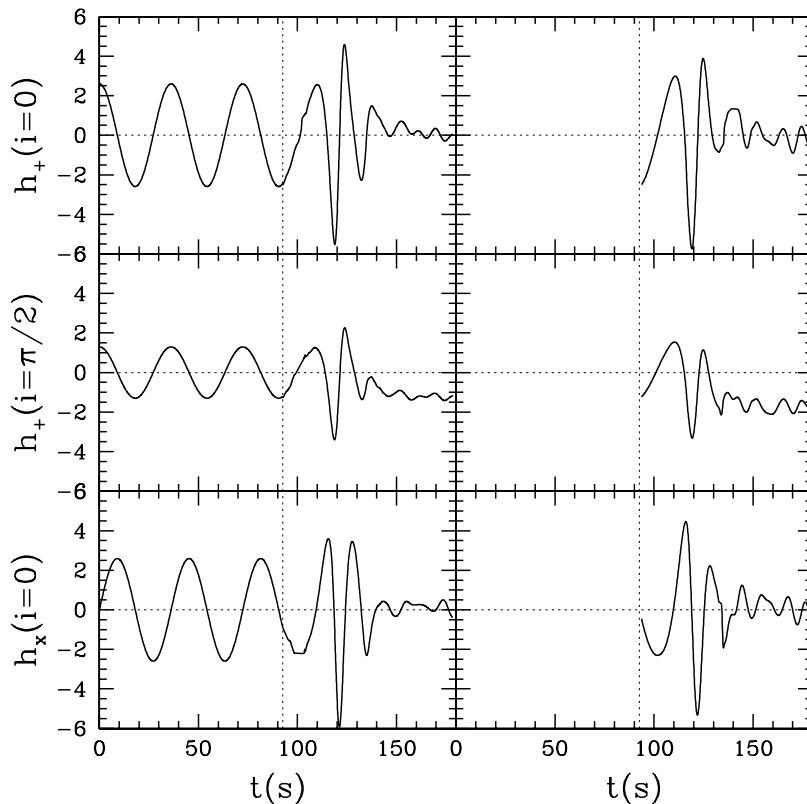


Figure 3.10: A comparison of the computed emission of gravitational waves when the resolution of our SPH simulations is changed. The left panels show the emission of gravitational waves for a simulation in which a low resolution ( $2 \times 10^4$  SPH particles) was used. The right panels show the same quantities when a high resolution was adopted ( $2 \times 10^5$  SPH particles). See text for further details.

$$M = (\mu M_{\text{tot}}^{2/3})^{3/5} \quad (3.14)$$

being  $\mu = m_1 m_2 / M_{\text{tot}}$  the reduced mass, and  $M_{\text{tot}} = m_1 + m_2$  the total mass.

In order to evaluate the maximum distance at which LISA would be able to detect the close white dwarf binary systems studied here we have adopted  $\eta = 5$ . We have furthermore used the integrated sensibility of LISA as obtained again from <http://www.srl.caltech.edu/~shane/sensitivity>. The results are given in Table 3.2, where the frequency of the close white dwarf binary system when the secondary overflows its Roche lobe, the chirping mass, the maximum distance at which LISA would detect them for a signal-to-noise ratio of 5 and one year integration, and the signal-to-noise ratio at 10 kpc for one year integration are shown. Also shown in

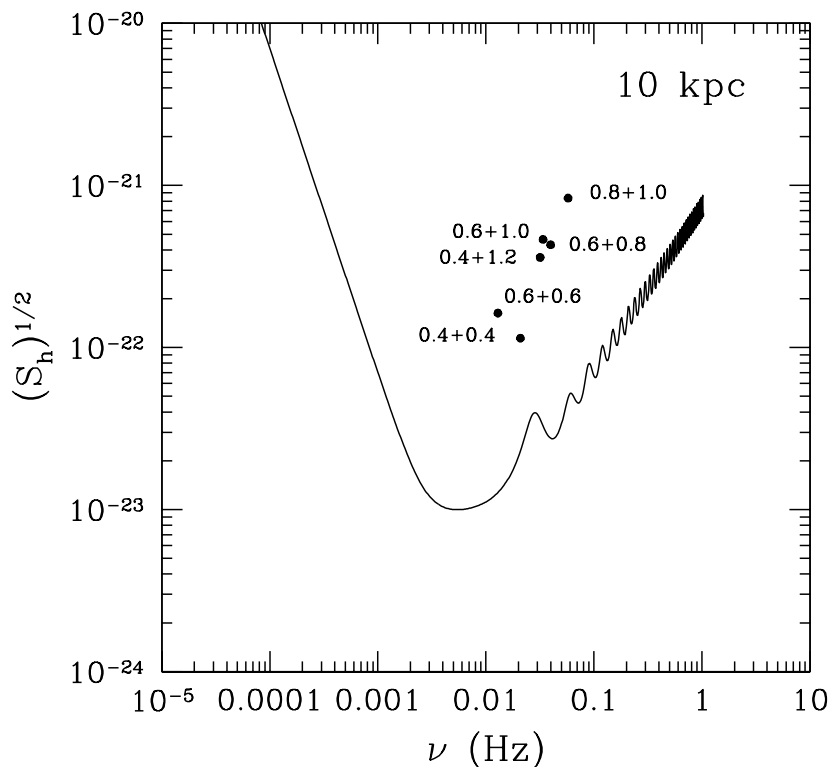


Figure 3.11: A comparison of the signal produced by the close white dwarf binary systems studied here, when a distance of 10 kpc is adopted, with the spectral distribution of noise of LISA for a one year integration period.

Table 3.2 are the peak amplitude at 10 kpc of the dimensionless strain (in units of  $10^{-22}$ ) and the total radiated energy in the form of gravitational waves. We stress that if the merger occurs during the one year integration period the signal-to-noise ratio would be smaller. It is worth noticing as well that the energy radiated away from the binary system during the coalescence in the form of gravitational waves is of the order of  $\sim 10^{41}$  erg, much smaller than the total energy of the system and, hence, totally negligible in the energy budget, so no back reaction should be taken into account and the procedure used here is robust. Note as well, that for the case of  $0.6 + 0.6 M_{\odot}$  system, in which two resolutions were used the maximum distance at which LISA would be able to detect the coalescence is very similar for both the high resolution simulation, 12.8 pc, and the low resolution simulation, 13.0 pc. The energy released during the coalescence is very similar as well in both cases,  $0.63$  and  $0.64 \times 10^{41}$  erg, respectively.

Finally, in Fig. 3.11 we compare the signal produced by the close white dwarf binary systems studied in this paper, when a distance of 10 kpc is adopted, with the spectral distribution of noise of LISA for a one year integration period. As it can be seen, all of them will be eventually detected, at different signal-to-noise ratios, ranging from  $\sim 5.0$  for the  $0.4+0.4 M_{\odot}$  system to  $\sim 16.6$  for the  $0.8+1.0 M_{\odot}$  system.

### 3.5 Discussion and conclusions

We have computed the emission of gravitational waves of merging white dwarf binaries, for a wide range of masses and compositions of the components of the binary system. For that purpose we have used the results of a SPH code which allowed us to follow the temporal evolution of the coalescing white dwarfs. We have shown that the most noticeable feature of the emitted signal is a sudden disappearance of the gravitational strains. By contrast the chirping phase will be easily detectable by future space-borne interferometers like LISA. In fact, it can be said that the most relevant signature of the merger will be the absence of any signature and the sudden disappearance of the source. Since the frequency coverage of LISA will range from  $10^{-1}$  to  $10^{-4}$  Hz, the detection of chirping close white dwarf binary systems is guaranteed (Farmer & Phinney 2003; Nelemans et al. 2001b). Moreover, at frequencies of  $\sim 3 \times 10^{-3}$  Hz most close white dwarf binary systems will be spectrally resolved (Cornish & Larson 2003). Typically, LISA will be able to detect  $\sim 3000$  binaries at these frequencies (Seto 2002). Additionally, it has been recently shown (Cooray et al. 2004) that the typical error box of LISA for these kind of systems will be  $\delta\Omega \sim 5 \text{ deg}^2$ , and that, given that many of the detected sources will be eclipsing binaries with a period equal to that of the gravitational waves, optical follow-up campaigns will allow us to further constrain the location of the sources. Hence, by combining optical observations and gravitational wave data, and taking into account that the gravitational wave signal for such mergers suddenly vanishes — or, equivalently, that during the integration period the signal-to-noise ratio stops growing — we should be able to gain insight into the physics of merging and to obtain precise information of the properties of the progenitor systems. Moreover, it should be taken into account that for a typical merger — namely, the  $0.6+0.8 M_{\odot}$  case — the volume accesible to LISA is  $V_{\text{LISA}} \sim 1.2 \times 10^{14} \text{ pc}^3$ . Since the volume of the Galaxy is  $V \sim 3 \times 10^{11} \text{ pc}^3$ , LISA would be able to detect all the mergers occuring in our Galaxy during its operation period. However, the typical rate of white dwarf mergers is  $r \sim 8.3 \times 10^{-3} \text{ yr}^{-1}$  (Nelemans 2003) and, hence, although there is an uncertainty of a factor of 5 in the rate of white dwarf mergers, the expected detection rate is consequently small.



## Chapter 4

# High-resolution SPH simulations of the merger of white dwarfs

The merger of two white dwarfs is the final outcome of a sizeable fraction of binary systems. Moreover, white dwarf mergers have been proposed to explain several interesting astrophysical phenomena. In this chapter we present the results of a set of high-resolution simulations of the merger of two white dwarfs. We use an up-to-date Smoothed Particle Hydrodynamics code which incorporates very detailed input physics and an improved treatment of the artificial viscosity. Our simulations have been done using a large number of particles ( $\sim 3 \times 10^5$ ) and cover the full range of masses and chemical compositions of the coalescing white dwarfs.

### 4.1 Introduction

The merger of a binary system made of two white dwarfs is thought to be one of the most common endpoints of the evolution of binary systems. Consequently, the study of the coalescence process is an interesting issue, with many potential applications. Although the astrophysical scenarios in which the coalescence of two white dwarfs in a close binary system can occur and their relative frequencies have been well studied — see, for instance, Yungelson et al. (1994), Nelemans et al. (2001a), Nelemans et al. (2001b), and the recent review of Postnov & Yungelson (2006) — the merging process has received little attention until recently. The pioneering works of Mochkovitch & Livio (1989, 1990) who used an approximate method — the so-called Self-Consistent-Field method (Clement 1974) — and the full Smoothed Particle Hydrodynamic (SPH) simulations of Benz et al. (1989a), Benz et al. (1989b), Benz et al. (1990) and Segretain et al. (1997) were the only exceptions. Most of these early works had several drawbacks. For instance, some of them did not include a detailed nuclear network or the network was very simplistic, other used a very small number of SPH particles ( $\sim 10^3$ ) and, finally, other did not discuss the properties of the merger configuration.

Additionally, all these early works studied a reduced set of masses and chemical compositions and used the classical expression for the artificial viscosity (Monaghan & Gingold 1983). This is an important issue since it is well known that SPH induces a large shear viscosity, which is more pronounced when the classical expression for the artificial viscosity is used. However, the situation has changed recently. Guerrero et al. (2004) opened the way to more realistic simulations. They used a SPH code to study a considerable range of masses and chemical compositions of the merging white dwarfs. Moreover, these simulations employed a sizeable number of particles ( $\sim 4 \times 10^4$ ) and a formulation of the artificial viscosity which reduces considerably the excess viscosity (Balsara 1995). Nevertheless, there are more recent viscosity formulations which reduce even more the excess of shear and, in addition, the available computing power has considerably increased since then. More recently, Yoon et al. (2007) have studied in detail the coalescence of a binary system composed of two white dwarfs of masses 0.6 and  $0.9 M_{\odot}$  using  $2 \times 10^5$  SPH particles. However, only one simulation was presented in this work. It is thus clear that a thorough parametric study in which several white dwarf masses and chemical compositions are explored using a larger number of SPH particles and a more elaborated treatment of the artificial viscosity remains to be done.

Possible applications of this kind of simulations include the formation of Type Ia supernovae in the double degenerate scenario (Webbink 1984; Iben & Tutukov 1984) and the formation of magnetars (King et al. 2001). Also three hot and massive white dwarfs members of the Galactic halo, could be the result of the coalescence of a double white dwarf binary system (Schmidt et al. 1992; Segretain et al. 1997). Additionally, the origin of hydrogen-deficient carbon and R Corona Borealis stars (Izzard et al. 2007; Clayton et al. 2007) and of extreme helium stars (Pandey et al. 2005) is thought to be the merger of two white dwarfs. Finally, the large metal abundances found around some hydrogen-rich white dwarfs with dusty disks around them can be explained by the merger of a CO and a He white dwarf (García-Berro et al. 2007). Last but not least, the coalescence of a double white dwarf close binary system has been shown to be a powerful source of gravitational waves which would be eventually detectable by LISA (Lorén-Aguilar et al. 2005).

In fact, the fate of double white dwarf binary systems is a merging process due to the loss of angular momentum through gravitational wave radiation. Stars will orbit each other at decreasing orbital separations until the less massive one overfills its Roche lobe and mass transfer begins. Depending on the initial conditions mass transfer proceeds either in an stable or a dynamically unstable regime. The stability of mass transfer is an important issue. If the mass transfer process is stable, mass will flow at relatively low accretion rates and the whole merging process could last for several million years. On the contrary, if mass transfer proceeds in an unstable way, the whole merging process finishes in a few minutes. The difference between the two cases relies on the ability of the binary system to return enough angular momentum back to the orbit. In fact, there are two competing processes. On the

one hand the donor star is supported by the pressure of degenerate electrons and, hence, it will expand as it loses mass, thus enhancing the mass-transfer rate. On the other, if orbital angular momentum is conserved the orbit will expand as the donor star loses mass thus reducing the mass-transfer rate. The precise trade-off between both physical processes determines the stability of mass transfer. Guerrero et al. (2004) found that all the systems merged in a few hundred seconds, corresponding to mass transfer rates of  $\sim 10^{-2} M_{\odot} \text{ s}^{-1}$ . Since the Eddington rate is of the order of  $10^{-5} M_{\odot} \text{ yr}^{-1}$  the most massive white dwarf cannot incorporate the material of the disrupted secondary in such a short timescale and, thus, the secondary forms a hot atmosphere and a heavy keplerian disk around the primary. This has been challenged by the simulations of Motl et al. (2002) and D’Souza et al. (2006). These authors used a grid-based three-dimensional finite-difference Eulerian hydrodynamical code and found that when the stars are co-rotating mass transfer is stable. Nevertheless, it should be noted that these simulations were done using simplified physical inputs. For instance, they used a polytropic equation of state. More importantly, grid-based methods are known to poorly conserve angular momentum. In any case, it is clear that to assess the stability of mass transfer large spatial resolutions are required given the degenerate nature of the donor star, since once mass transfer begins the radius of the secondary increases very rapidly thereby increasing the mass-loss rate.

In this chapter we study the coalescence of binary white dwarfs employing an enhanced spatial resolution ( $3 \times 10^5$  SPH particles) and a formulation of the artificial viscosity which very much reduces the excess of shear. This is done for a broad range of initial masses and chemical compositions of the coalescing white dwarfs. In particular we study the following cases:  $0.3 + 0.5 M_{\odot}$ ,  $0.4 + 0.8 M_{\odot}$ ,  $0.6 + 0.6 M_{\odot}$ ,  $0.6 + 0.8 M_{\odot}$ ,  $0.6 + 0.8 M_{\odot}$ , and  $0.6 + 1.2 M_{\odot}$ . Although we have computed a large number of mergers we will only discuss in detail the results of the merger of a  $0.6 + 0.8 M_{\odot}$  binary system. The main results of the rest of the simulations are only given in tabular form, but we can provide them upon request of the interested reader. The large number of particles used here allows to compare the results of our hydrodynamical calculations with the theoretical expectations. Consequently, we will devote most of the chapter to compare the results of this set of simulations with those of our previous paper (Guerrero et al. 2004) and with those of the available high-resolution simulations (Yoon et al. 2007). The chapter is organized as follows. In section 4.2 a general description of our SPH code is given. In section 4.3 we describe the results of the simulations and we compare them with the results of other authors. In section 4.4 we discuss these simulations. Specifically, we pay special attention to discuss the stability of mass transfer. This is done in section 4.4.1, whereas in sections 4.4.2 and 4.4.3 the possible observational signatures arising from the merging process are studied. In particular, we consider the gravitational wave pattern of the several mergers studied here (section 4.4.2) and the X-ray emission that might be expected from the early phases of the disk evolution (section 4.4.3), while in section 4.4.4 the long-term evolution of the result of the merger is discussed. Finally, in section 4.5

we summarize our major findings, we elaborate on the possible implications of our work and we draw our conclusions.

## 4.2 Input physics and method of calculation

We follow the hydrodynamic evolution of the binary system using a Lagrangian particle numerical code, the so-called Smoothed Particle Hydrodynamics. This method was first proposed by Lucy (1977) and, independently, by Gingold & Monaghan (1977). The fact that the method is totally Lagrangian and does not require a grid makes it specially suitable for studying an intrinsically three-dimensional problem like the coalescence of two white dwarfs. We will not describe in detail the most basic equations of our numerical code, since this is a well-known technique. Instead, the reader is referred to Benz (1990) where the basic numerical scheme for solving the hydrodynamic equations can be found, whereas a general introduction to the SPH method can be found in the excellent review of Monaghan (2005). However, and for the sake of completeness, we shortly describe the most relevant equations of our numerical code.

We use the standard polynomial kernel of Monaghan & Lattanzio (1985). The gravitational forces are evaluated using an octree (Barnes & Hut 1986). Our SPH code uses a prescription for the artificial viscosity based in Riemann-solvers (Monaghan 1997). Additionally, to suppress artificial viscosity forces in pure shear flows we also use the viscosity switch of Balsara (1995). In this way that the dissipative terms are essentially absent in most parts of the fluid and are only used where they are really necessary to resolve a shock, if present. Within this approach, the SPH equations for the momentum and energy conservation read respectively

$$\frac{d\vec{v}_i}{dt} = - \sum_j m_j \left( \frac{P_i}{\rho_i^2} + \frac{P_j}{\rho_j^2} - \alpha \frac{v_{ij}^{\text{sig}}}{\bar{\rho}_{ij}} \vec{v}_{ij} \cdot \hat{e}_{ij} \right) \vec{r}_{ij} F_{ij} \quad (4.1)$$

$$\frac{du_i}{dt} = \frac{P_i}{\rho_i^2} \sum_j m_j \vec{v}_{ij} \cdot \vec{r}_{ij} \bar{F}_{ij} - \frac{1}{2} \sum_j m_j \alpha \frac{v_{ij}^{\text{sig}}}{\bar{\rho}_{ij}} (\vec{v}_{ij} \cdot \hat{e}_{ij})^2 |\vec{r}_{ij}| \bar{F}_{ij} \quad (4.2)$$

where  $\bar{\rho}_{ij} = (\rho_i + \rho_j)/2$  and  $\bar{F}_{ij} \equiv (F_i + F_j)/2$ , and  $F$  is a positive definite function which depends only on  $|\vec{r}|$  and on the smoothing kernel  $h$ , used to express gradient of the kernel  $\vec{\nabla} W_{ij} = \bar{F}_{ij} \vec{r}_{ij}$ . The signal velocity is taken as  $v_{ij}^{\text{sig}} = c_i + c_j - 4\vec{v}_{ij} \cdot \hat{e}_{ij}$  and the rest of the symbols have their usual meaning. We have found that  $\alpha = 0.5$  yields good results.

However, we have found that it is sometimes advisable to use a different formulation of the equation of energy conservation. Accordingly, for each timestep we compute the variation of the internal energy using Eq. (4.2) and simultaneously calculate the variation of temperature using:

$$\frac{dT_i}{dt} = - \sum_{j=1}^N \frac{m_j}{(C_v)_j} \frac{T_j}{\rho_i \rho_j} \left[ \left( \frac{\partial P}{\partial T} \right)_{\rho_j} \right] \vec{v}_{ij} \cdot \vec{\nabla}_i W(|\vec{r}_{ij}|, h) + q_{\text{visc}} \quad (4.3)$$

where  $q_{\text{visc}}$  includes the contribution of viscous dissipation, which is computed in a way analogous to that of Eq. (4.2). For regions in which the temperatures are lower than  $6 \times 10^8$  K or the densities are smaller than  $6 \times 10^3$  g/cm<sup>3</sup> Eq. (4.2) is adopted, whereas Eq. (4.3) is used in the rest of the fluid. Using this prescription we find that energy is best conserved.

The equation of state adopted for the white dwarf is the sum of three components. The ions are treated as an ideal gas but taking into account the Coulomb corrections. We have also incorporated the pressure of photons, which turns out to be important only when nuclear reactions become relevant. Finally the most important contribution is the pressure of degenerate electrons which is treated integrating the Fermi-Dirac integrals. The nuclear network adopted here (Benz et al. 1989b) incorporates 14 nuclei: He, C, O, Ne, Mg, Si, S, Ar, Ca, Ti, Cr, Fe, Ni and Zn. The reactions considered are captures of  $\alpha$  particles, and the associated back reactions, the fusion of two C nuclei, and the reaction between C and O nuclei. All the rates are taken from Rauscher & Thielemann (2000). The nuclear energy release is computed independently of the dynamical evolution with much smaller time-steps, assuming that the dynamical variables do not change much during these time-steps. Finally, neutrino losses have been also included according to the formulation of Itoh et al. (1996).

Regarding the integration method we use a predictor-corrector numerical scheme with variable time step (Serna et al. 1996), which turns out to be quite accurate. With this procedure the energy and angular momentum of the system are conserved to a good accuracy. In order to achieve an equilibrium initial configuration we relaxed each individual model star separately. In all cases the initial system is composed of the two white dwarfs in a circular orbit at a distance slightly larger than that of the Roche lobe radius of the less massive component. In this way mass transfer in the system will immediately start and we avoid using numerical artifacts like adding artificial acceleration terms in order to decrease the separation of the stars. We adopt this instant as our time origin. This is done because we cannot follow in a physically consistent way the orbital evolution of the binary system during the inspiralling phase due to gravitational wave emission because the corresponding timescales are very large. The systems are not synchronized because, at least in the stage previous to the coalescence itself, the time scale for loss of angular momentum due to the emission of gravitational radiation is so small that it remains quite unlikely that there exists any dissipation mechanism able to ensure synchronization (Segretain et al. 1997). However, as already stated, synchronized systems will be studied in a forthcoming future.

The chemical compositions of the coalescing white dwarfs depend on the mass of

Table 4.1: Summary of hydrodynamical results. Masses and radii are in solar units, times in seconds and energies in ergs.

Run	$M_{\text{WD}}$	$M_{\text{disk}}$	$M_{\text{acc}}$	$M_{\text{ej}}$	$T_{\text{peak}}$	$T_{\text{max}}$	$R_{\text{disk}}$	$H$	$\Delta t$	$E_{\text{nuc}}$	$E_{\nu}$	$E_{\text{GW}}$
0.3+0.5	0.62	0.18	0.12	$10^{-3}$	$6.0 \times 10^8$	$6.0 \times 10^8$	0.2	$6.1 \times 10^{-3}$	300	$1 \times 10^{42}$	$4 \times 10^{21}$	$9 \times 10^{38}$
0.4+0.8	0.92	0.28	0.12	$10^{-3}$	$6.5 \times 10^8$	$6.0 \times 10^8$	0.2	$6.0 \times 10^{-3}$	166	$1 \times 10^{44}$	$5 \times 10^{24}$	$4 \times 10^{39}$
0.6+0.6	1.10	0.10	0.50	$10^{-3}$	$6.3 \times 10^8$	$6.2 \times 10^8$	0.07	$5.5 \times 10^{-3}$	514	0	$3 \times 10^{24}$	$1 \times 10^{41}$
0.6+0.8	1.10	0.30	0.30	$10^{-3}$	$2.0 \times 10^9$	$8.7 \times 10^8$	0.2	$5.0 \times 10^{-3}$	164	$1 \times 10^{41}$	$3 \times 10^{28}$	$6 \times 10^{40}$
0.6+1.2	1.50	0.30	0.30	$10^{-3}$	$1.0 \times 10^{10}$	$1.0 \times 10^9$	0.2	$4.4 \times 10^{-3}$	122	$2 \times 10^{44}$	$8 \times 10^{36}$	$5 \times 10^{40}$

each star. White dwarfs with masses smaller than  $0.45 M_{\odot}$  have pure He cores. For white dwarfs with masses within this value and  $1.1 M_{\odot}$  we adopt the corresponding chemical composition, namely, carbon and oxygen, with mass fractions  $X_C = 0.4$  and  $X_O = 0.6$  uniformly distributed through out the core. Finally, white dwarfs more massive than  $1.1 M_{\odot}$  have ONe cores of the appropriate composition (Ritossa et al. 1996).

### 4.3 Results

Figs. 4.1 and 4.2 show the temporal evolution of the logarithm of density for the coalescence of the  $0.6 + 0.8 M_{\odot}$  double white dwarf binary system. In Fig. 4.1 the positions of the SPH particles have been projected onto the equatorial plane and in Fig. 4.2 onto the polar plane. Time (in seconds) is shown on the right upper corner of each panel. As can be seen in the uppermost left panels, the initial configurations of both white dwarfs are rather symmetric. Soon after, the less massive white dwarf fills its Roche lobe and mass transfer begins, as can be seen in top central panel of this figure. The top right panel of Fig. 4.1 shows that, after some time, the matter outflowing the secondary hits the surface of the primary white dwarf and spreads on top of it. Note as well that since the radius of white dwarfs scales as  $\sim M^{-1/3}$ , as the secondary loses mass its radius increases and, hence, the mass-loss rate of the secondary increases, thus leading to a positive feedback of the process. As a consequence of this positive feedback an accretion arm is formed which extends from the remnant of the secondary white dwarf (central panels in Fig. 4.1) to the surface of the primary white dwarf. This accretion arm becomes entangled as a consequence of the orbital motion of the coalescing white dwarfs and adopts a spiral shape (bottom left panel). Ultimately, the secondary is totally disrupted and a heavy disk is formed around the primary (bottom central panel of Fig. 4.1). The bottom right panel of Fig. 4.1 shows that at time  $t = 152$  s the disk is still not well formed and the remnant of a spiral arm still persists. We followed the evolution of this merger for some more time and we found that the final configuration has cylindrical symmetry, that all the orbits of the SPH particles belonging to the secondary have been circularized and that the spiral pattern has totally disappeared. At the end of the simulations the radial extension of the disk is  $\sim 0.2 R_{\odot}$ , whereas its height is  $\sim 5.0 \times 10^{-3} R_{\odot}$ .

The temporal evolution of the temperature for the merger of a  $0.6 + 0.8 M_{\odot}$  binary system is shown in Fig. 4.3. As can be seen in this figure the material of the secondary is first heated by tidal torques. As the secondary begins the disruption process this material is transferred to the surface of the primary and, consequently, it is compressed and its temperature increases. The peak temperatures ( $T_{\text{peak}}$ ) achieved during the coalescence are displayed in Table 4.1 for each one of the runs presented in this paper. For the  $0.6 + 0.8 M_{\odot}$  simulation the peak temperature is  $T_{\text{peak}} \sim 2.0 \times 10^9$  K, clearly larger than the carbon ignition temperature  $T_{\text{ign}} \sim 10^9$  K, and occurs

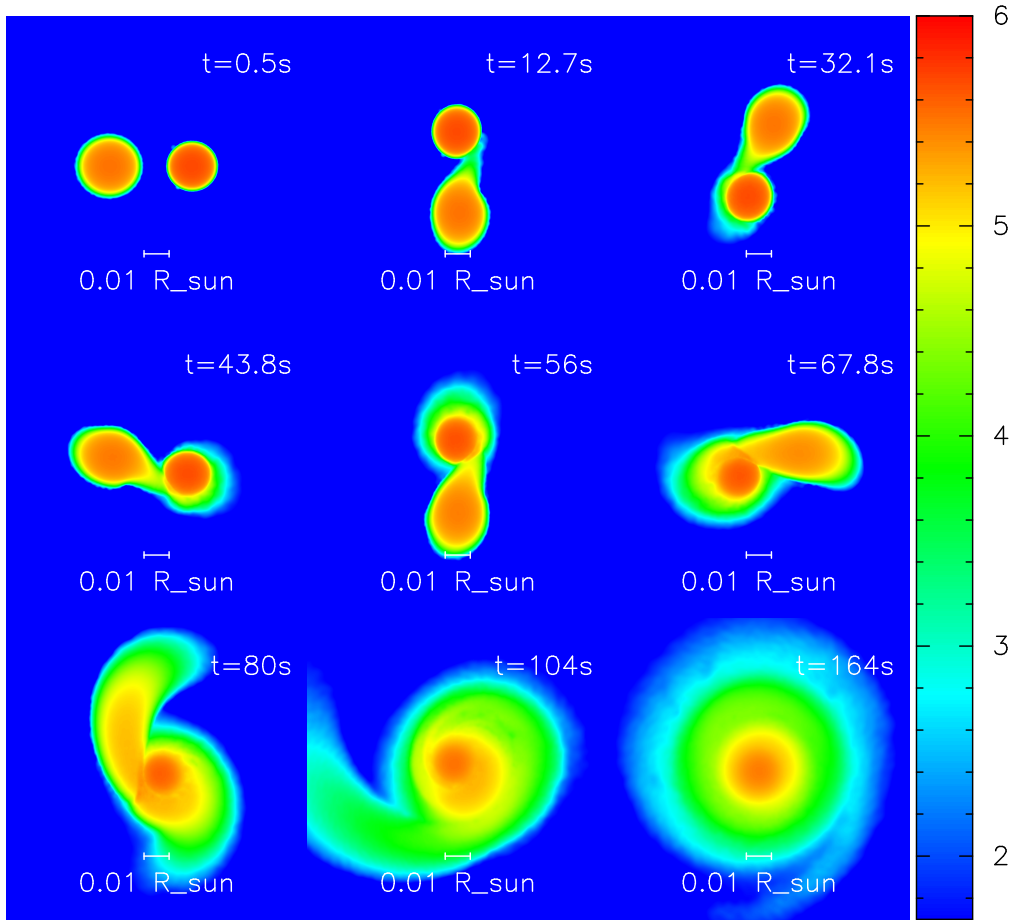


Figure 4.1: Temporal evolution of the density for the coalescence of the  $0.6 + 0.8 M_{\odot}$  double dwarf binary system. The positions of the particles have been projected onto the  $xy$  plane. The units of positions and densities are, respectively, solar radii and  $10^9 \text{ g/cm}^3$ . Times are shown in the right upper corner of each panel. These figures have been done using the visualization tool SPLASH (Price 2007).

during the first and most violent part of the merger. However, a strong thermonuclear flash does not develop because although the temperature in the region where the material of the secondary first hits the primary increases very rapidly, degeneracy is rapidly lifted, leading to an expansion of the material, which, in turn, quenches the thermonuclear flash. This is in agreement with the results of Guerrero et al. (2004) and Yoon et al. (2007). Thus, since these high temperatures are attained only during a very short time interval thermonuclear processing is very mild for this simulation. It is also interesting to compare the equatorial and polar distribution

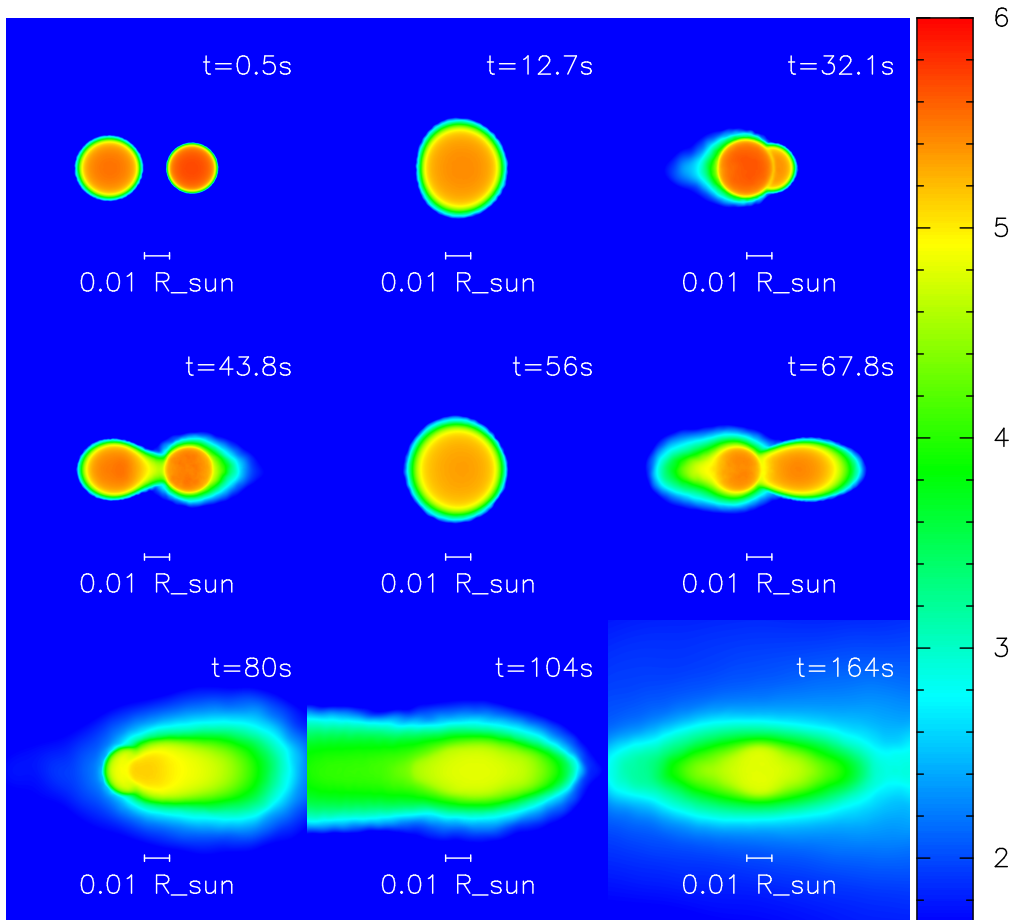


Figure 4.2: Temporal evolution of the density for the coalescence of the  $0.6 + 0.8 M_{\odot}$  double dwarf binary system. The positions of the particles have been projected onto the  $xz$  plane. The units of positions and densities are, respectively, solar radii and  $10^9 \text{ g/cm}^3$ . Times are shown in the right upper corner of each panel. These figures have been done using the visualization tool SPLASH (Price 2007).

of temperatures shown in the central panels of Figs. 4.3 and 4.4. This comparison reveals that the heated material is rapidly redistributed on the surface of the primary and, as a consequence, a hot corona forms around the primary. The spiral structure previously described can be more easily appreciated in the bottom right panels of figure 4.3. In fact, this spiral structure persists for some more time.

In all the cases studied here a self-gravitating structure forms after a few orbital periods, in agreement with our previous findings (Guerrero et al. 2004) and with those of Yoon et al. (2007). The time necessary for its formation depends on

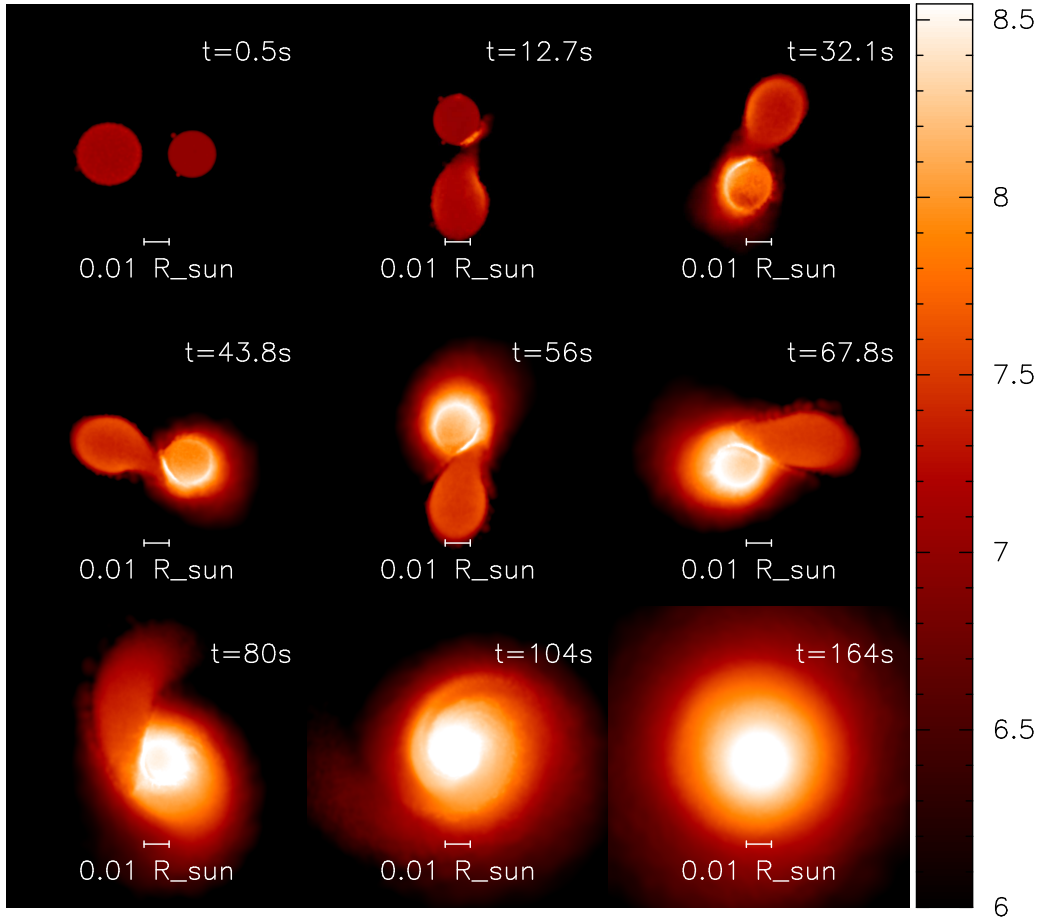


Figure 4.3: Temporal evolution of the temperature (in units of  $10^8$  K) for the coalescence of the same binary system shown in Fig. 4.1. The positions of the particles have been projected onto the  $xy$  plane. These figures have been done using the visualization tool SPLASH (Price 2007).

the system being studied, and ranges from  $\sim 120$  seconds to  $\sim 520$  seconds. This self-gravitating structure consists in all the cases but that in which two equal-mass white dwarfs are involved of a compact central object, surrounded by a heavy keplerian disk of variable extension. In the case in which two  $0.6 M_{\odot}$  white dwarfs are involved the configuration is rather different. In this last case the symmetry of the systems avoids the formation of a clear disk structure, giving rise instead to a rotating ellipsoid around the central compact object, surrounded by a considerably smaller disk. In table 4.1 we summarize the most relevant parameters of all the mergers studied here. Columns two, three, four and five list, respectively, the mass

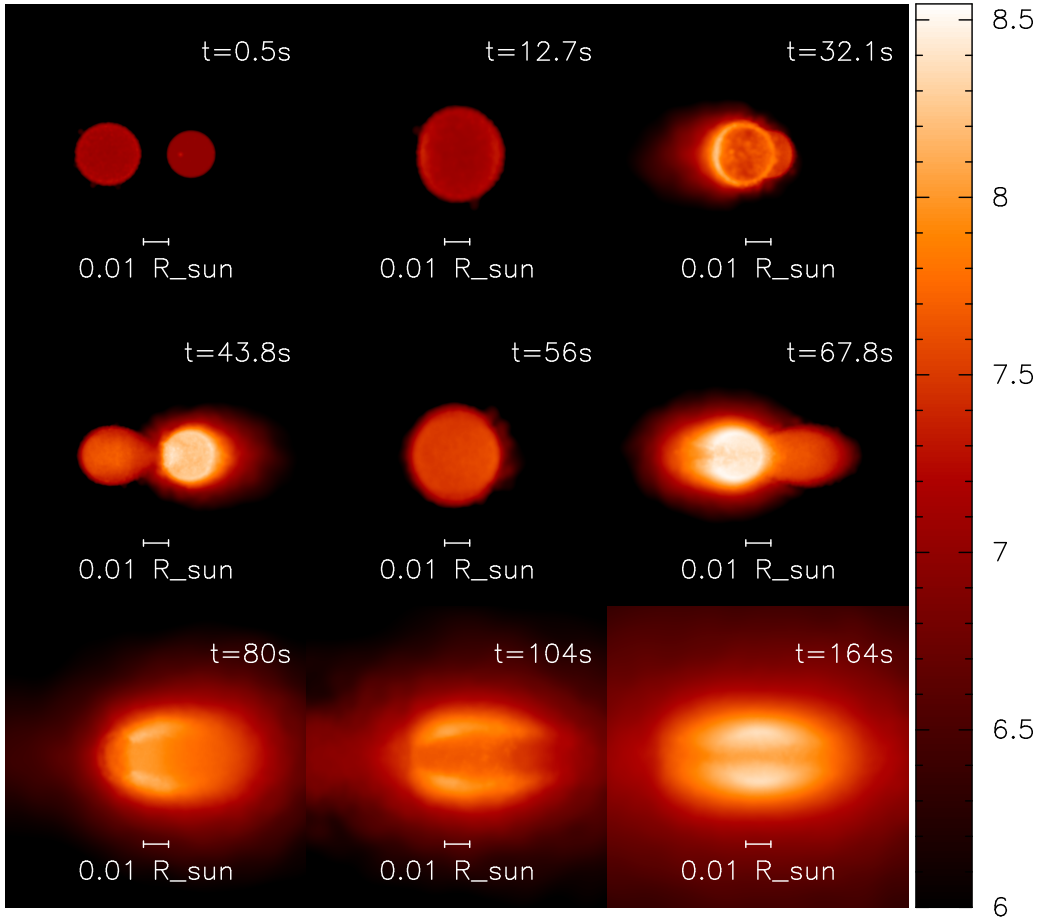


Figure 4.4: Temporal evolution of the temperature (in units of  $10^8$  K) for the coalescence of the same binary system shown in Fig. 4.1. The positions of the particles have been projected onto the  $xz$  plane. These figures have been done using the visualization tool SPLASH (Price 2007).

of the central white dwarf obtained after the disruption of the secondary, the mass of the keplerian disk, the accreted and the ejected mass. All the masses are expressed in solar units. In column six we show the peak temperatures achieved during the coalescence. In column seven we display the temperature of the hot corona around the central object by the end of our simulations, whereas in column eight the radius of the disk is shown. In column nine we list the disk half-thickness. Finally column ten displays the duration of the coalescence process and columns eleven, twelve and thirteen display the energetics of the process. In particular we show the thermonuclear energy released during the coalescence process ( $E_{\text{nuc}}$ ), the neutrino

energy ( $E_\nu$ ) and the energy radiated in the form of gravitational waves ( $E_{\text{GW}}$ ). As can be seen, for the first two simulations the accreted mass is approximately the same and the same occurs for the last two simulations. As already commented, the simulation in which two equal-mass white dwarfs are involved is rather special and in this case we do not have properly speaking a disk, although a very flattened region with cylindrical symmetry forms around the central object of ellipsoidal shape. The mass of this region is  $\sim 0.1 M_\odot$ . In all five cases the mass ejected from the system (those particles which acquire velocities larger than the escape velocity) is very small ( $\sim 10^{-3} M_\odot$ ), and thus the merging process can be considered as conservative. The maximum temperatures of the coronae increase as the total mass of the binary system increases. It should be noted that for the case of the  $0.6 + 0.6 M_\odot$  binary system the maximum temperature occurs at the center of the merged configuration. We have found that these temperatures are somewhat smaller than those obtained in our previous simulations (Guerrero et al. 2004). This is a direct consequence of the improved treatment of the artificial viscosity. It is worth noting that the radial extension of the disks is roughly the same for all but one the simulations presented here and it is considerably smaller for the case in which two equal-mass white dwarfs are involved. This is a natural behavior since in this last case the central object is rather massive. Finally, it is as well interesting to realize that all the disks are rather thin, being the typical half-thickness of the order of  $\sim 10^{-3} R_\odot$ , much smaller than the typical disk radial extension,  $\sim 0.2 R_\odot$ .

The chemical composition of the disk formed by the disrupted secondary can be found for all the simulations presented in this paper in Table 4.2. In this table we show, for each of the mergers computed here, the averaged chemical composition (by mass) of the heavily rotationally-supported disk — left section of table 4.2 — and the hot corona — right section — described previously. For the mergers in which two carbon-oxygen white dwarfs are involved the disk is mainly formed by carbon and oxygen and the nuclear processing is very small (see the peak temperatures shown in column ten of Table 4.1). This is not the case for the simulations in which a lighter He white dwarf is involved. Since in these cases the Coulomb barrier is considerably smaller, the shocked material is nuclearly processed and heavy isotopes form. This is more evident for the case in which a massive He white dwarf of  $0.4 M_\odot$  is disrupted by a massive CO white dwarf of  $0.8 M_\odot$  — third and eight columns in Table 4.2. In this case the abundances in the disk and the hot corona are rather large. Note as well that the abundances of heavy nuclei in the hot corona are much larger than those of the disk, indicating that most of the nuclear reactions occur when the accretion stream hits the surface of the primary. Nevertheless, although the disk is primarily made of the He coming from the disrupted secondary the abundances of C and O are sizeable and, moreover, the disk is contaminated by heavy metals. This has important consequences because it is thought that some of the recently discovered metal-rich DA white dwarfs with dusty disks around them — also known as DAZd white dwarfs — could be formed by accretion of a minor planet. The origin of such

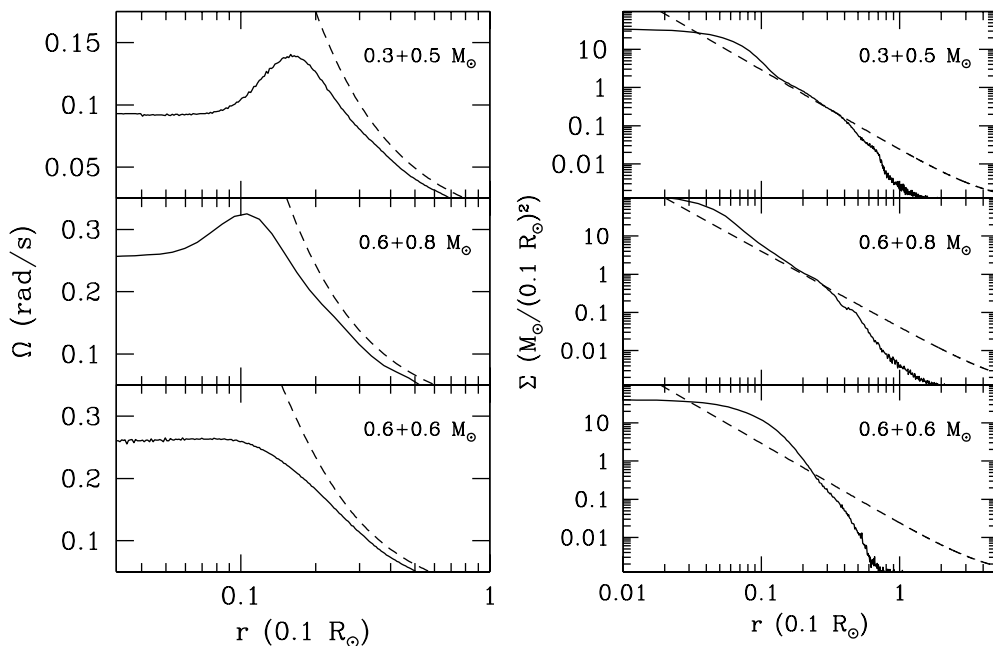


Figure 4.5: Left panels: rotational velocity of the merger products as a function of the radius. For the sake of comparison the keplerian velocity is also shown as a dashed line. Right panels: surface density profiles compared with the theoretical thin disk model profiles (dashed lines).

minor planets still remains a mystery, since asteroids sufficiently close to the white dwarf would have not survived the AGB phase (Villaver & Livio 2007). However, planet formation in these metal-rich disks is expected to be rather efficient, thus providing a natural environment where minor planetary bodies could be formed and, ultimately, tidally disrupted to produce the observed abundance pattern in these white dwarfs (García-Berro et al. 2007). Nuclear reactions are also important in the case in which a regular  $0.6 M_\odot$  carbon-oxygen white dwarf and a massive oxygen-neon white dwarf of  $1.2 M_\odot$  are involved. In this case the peak temperature achieved during the coalescence is rather high  $T_{\text{peak}} \simeq 1.0 \times 10^{10}$  — see Table 4.1 — enough to power carbon burning. Consequently, the chemical abundances of the keplerian disk and of the hot corona are largely enhanced in oxygen and neon, which are the main products of carbon burning.

In figure 4.5 we explore the final characteristics of the merged configuration. We start discussing the left panels of figure 4.5 which show the rotational velocity of the merger as a function of the distance to the center of the merged object. Clearly in all the cases there is a central region which rotates as rigid solid. This behavior was already found in Guerrero et al. (2004) and Yoon et al. (2007), and it is a consequence of the conservation of angular momentum. On top of this region

a differentially rotating layer is present. This rapidly rotating region is formed by material coming from the disrupted secondary, which has been accumulated on top of the primary and thus carries the original angular momentum of the secondary. Finally, for sufficiently large radius a rotationally-supported disk is found. The exact location where the disk begins can be easily found by looking at the left panels of Fig. 4.5, where the keplerian velocity is also shown as a dashed line. The change in the slope of the profile of the rotational velocity clearly marks the outer edge of the compact inner object and the beginning of the disk. All the disks extend up to some solar radii — see column eight in Table 4.1. The stratification of surface densities of these disks can be seen in the left panels of Fig. 4.5, where we have plotted the surface density as a function of the distance. For the sake of comparison the theoretical surface density of a thin disk analytical model (Lorén-Aguilar et al. 2005) is also shown as a dashed line. Within this model the surface density of the disk should be of the form  $\Sigma \propto R^{-\beta}$ . We have used  $\beta = 7/4$  to produce the dashed lines in the right panels of Fig. 4.5, very close to the value adopted by Lorén-Aguilar et al. (2005),  $\beta = 3/2$ . As can be seen in this figure for the first two fiducial mergers studied here there is a region where the analytical model and the numerical results are in good agreement. However, at large enough distances the SPH density profile falls off more rapidly than that of the theoretical model. In the case of the merger of two equal-mass  $0.6 M_{\odot}$  white dwarfs the agreement is poor. In this case, the symmetry of the system avoids the formation of a clear disk structure, giving rise instead to a rotating ellipsoid around the central compact object. Moreover, it can be shown that the angular momentum of the disk can be expressed in terms of the disk radius  $R_{\text{disk}}$  and the disk mass  $M_{\text{disk}}$  as  $J_z = \xi M_{\text{disk}} (GM_{\text{WD}} R_{\text{disk}})^{1/2}$ , where  $\xi = (2 - \beta)/(5/2 - \beta) = 1/3$ . The theoretical angular momenta obtained using this equation agree very well with the results of our SPH simulations.

In Fig. 4.6 we show the temperature profiles at the end of the simulations for some of the mergers studied here. We have averaged the temperatures of those particles close to the orbital plane. The average was done using cylindrical shells and the size of these shells was chosen in such a way that each of them contained a significant number of particles. As can be seen, for the  $0.3 + 0.5 M_{\odot}$  and the  $0.4 + 0.8 M_{\odot}$  systems, the region of maximum temperatures occurs off-center, at the edge of the original primary, in the region of accreted and shocked material, whereas for the merger in which two equal-mass  $0.6 M_{\odot}$  white dwarfs coalesce the maximum temperature occurs at the center of the merged object, as it should be expected. These maximum temperatures are listed in the seventh column of Table 4.1. In fact, the temperature profiles shown in this figure clearly show that the cores of the primaries in the first two simulations remain almost intact and, hence, are rather cold. These cores, in turn, are surrounded by a hot envelope which corresponds to the shocked material coming from the disrupted secondary. Nuclear reactions are responsible for the observed heating of the accreted matter, initially triggered in the shocked regions. The case in which two  $0.6 M_{\odot}$  white dwarfs coalesce is somewhat

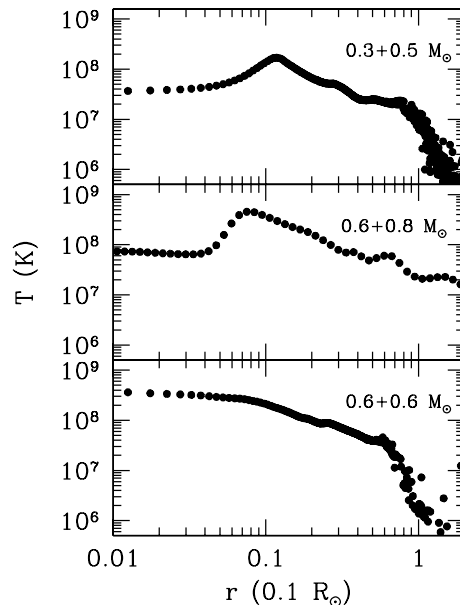


Figure 4.6: Radially averaged temperature profiles as a function of radius.

different. In this case there is not a hot envelope around central object — although a local maximum of temperatures can indeed be appreciated at the edge of the rapidly spinning central object, as shown in the bottom panel of Fig. 4.6 — and, instead, the central region of the compact object is formed by the cores of the merging white dwarfs. Most of the temperature increase in this case is due to viscous heating since nuclear reactions are negligible because the increase in temperature of the shocked material is not enough to ignite carbon. In all the cases it is rather apparent a sizeable dispersion of temperatures in the outermost regions. This dispersion is due in part to the fact that in these regions some of the particles that were ejected during the first and most violent phases of the merger can be found.

## 4.4 Discussion

### 4.4.1 Comparison with theory

To obtain a better understanding of the coalescence process and to compare our results with those theoretically expected, we have numerically solved the equations of the evolution of the binary system during the mass transfer phase. The evolution of a binary system during this phase is determined by three basic physical processes, namely, gravitational wave emission, tidal torques and mass transfer. There is a wealth of literature dealing with this problem. We adopt as our starting point the

analysis of Marsh et al. (2004) and the more recent formulation of Gokhale et al. (2007).

The total angular momentum of the system is given by:

$$J_{\text{tot}} = J_{\text{orb}} + J_1 + J_2 = M_1 M_2 \sqrt{\frac{Ga}{M}} + I_1 \omega_1 + I_2 \omega_2 \quad (4.4)$$

where subscript 1 refers to the accretor star and subscript 2 refers to the donor star,  $I_1$  and  $I_2$  are the moments of inertia of the stars,  $\omega_1$  and  $\omega_2$  are the spin angular frequencies,  $M$  is the total mass of the system and  $a$  is the orbital separation. Following Gokhale et al. (2007) the total variation of the orbital angular momentum can be expressed as:

$$\dot{J}_{\text{orb}} = \dot{J}_{\text{GW}} + (j_2 - j_1) \dot{M}_2 - \frac{I_1}{\tau_1} (\Omega - \omega_1) - \frac{I_2}{\tau_2} (\Omega - \omega_2) \quad (4.5)$$

where  $j_1$  represents the specific angular momentum of the infalling matter onto the accretor,  $j_2$  represents the specific angular momentum of the ejected matter from the donor,  $\Omega$  is the orbital angular frequency and  $\tau_1$  and  $\tau_2$  are the synchronization timescales of the accretor and the donor, respectively. The synchronization timescales have been computed using the expressions of Campbell (1984)

$$\begin{aligned} \tau_1 &= \tau_1^0 \left( \frac{M_1}{M_2} \right)^2 \left( \frac{a}{R_1} \right)^6 \\ \tau_2 &= \tau_2^0 \left( \frac{M_2}{M_1} \right)^2 \left( \frac{a}{R_2} \right)^6 \end{aligned} \quad (4.6)$$

where the normalization factors  $\tau_1^0$  and  $\tau_2^0$  are freely adjustable parameters (Marsh et al. 2004; Gokhale et al. 2007).

The first term in Eq. (4.5) corresponds to the angular momentum losses due to gravitational radiation and is given by (Landau & Lifshitz 1975):

$$\dot{J}_{\text{GW}} = -\frac{32}{5} \frac{G^3}{c^5} \frac{M_1 M_2 M_{\text{tot}}}{a^4} J_{\text{orb}} \quad (4.7)$$

The second term in Eq. (4.5) is the orbital angular momentum loss due to mass transfer between stars. Finally, the last two terms represent tidal torques due to non-synchronization of spin and orbital angular velocities of the stars. Now, in order to find an expression for the time variation of the orbital separation  $a$ , we use the time derivative of the orbital angular momentum of the system — see Eq. (4.4) — for conservative mass transfer:

$$\frac{\dot{J}_{\text{orb}}}{J_{\text{orb}}} = (1 - q) \frac{\dot{M}_2}{M_2} + \frac{1}{2} \frac{\dot{a}}{a} \quad (4.8)$$

where  $q = M_2/M_1$ . Then, the variation of the orbital separation  $\dot{a}$  is given by:

Table 4.2: Averaged chemical composition (by mass) of the heavy rotationally-supported disk and the hot corona obtained by the end of the coalescing process.

Run	Disk					Corona				
	0.3+0.5	0.4+0.8	0.6+0.6	0.6+0.8	0.6+1.2	0.3+0.5	0.4+0.8	0.6+0.6	0.6+0.8	0.6+1.2
He	0.94	0.98	0	0	$5 \times 10^{-5}$	0.72	0.68	0	0	$5 \times 10^{-5}$
C	$2.4 \times 10^{-2}$	$7 \times 10^{-3}$	0.4	0.4	0.39	0.11	0.12	0.4	0.4	0.26
O	$3.6 \times 10^{-2}$	$9 \times 10^{-3}$	0.6	0.6	0.60	0.17	0.18	0.6	0.6	0.66
Ne	$9 \times 10^{-13}$	$6 \times 10^{-10}$	0	0	$3 \times 10^{-3}$	$3 \times 10^{-13}$	$7 \times 10^{-7}$	0	0	0.07
Mg	$4 \times 10^{-14}$	$5 \times 10^{-11}$	0	0	$7 \times 10^{-5}$	$1 \times 10^{-12}$	$1 \times 10^{-5}$	0	0	$8 \times 10^{-5}$
Si	$1 \times 10^{-17}$	$3 \times 10^{-14}$	0	0	$1 \times 10^{-5}$	$1 \times 10^{-11}$	$1 \times 10^{-4}$	0	0	$5 \times 10^{-5}$
S	$2 \times 10^{-23}$	$1 \times 10^{-19}$	0	0	$3 \times 10^{-7}$	$1 \times 10^{-10}$	$2 \times 10^{-4}$	0	0	$5 \times 10^{-5}$
Ar	$< 10^{-30}$	$7 \times 10^{-27}$	0	0	$1 \times 10^{-7}$	$5 \times 10^{-9}$	$9 \times 10^{-4}$	0	0	$4 \times 10^{-5}$
Ca	$< 10^{-30}$	$< 10^{-30}$	0	0	$8 \times 10^{-7}$	$1 \times 10^{-8}$	$5 \times 10^{-4}$	0	0	$1 \times 10^{-4}$
Ti	$< 10^{-30}$	$< 10^{-30}$	0	0	$7 \times 10^{-7}$	$2 \times 10^{-4}$	$1 \times 10^{-2}$	0	0	$1 \times 10^{-4}$
Cr	$< 10^{-30}$	$< 10^{-30}$	0	0	$8 \times 10^{-7}$	$4 \times 10^{-4}$	$2 \times 10^{-3}$	0	0	$2 \times 10^{-4}$
Fe	$< 10^{-30}$	$< 10^{-30}$	0	0	$5 \times 10^{-6}$	$2 \times 10^{-5}$	$1 \times 10^{-5}$	0	0	$6 \times 10^{-4}$
Ni	$< 10^{-30}$	$< 10^{-30}$	0	0	$6 \times 10^{-4}$	$2 \times 10^{-7}$	$4 \times 10^{-8}$	0	0	$1 \times 10^{-2}$
Zn	$< 10^{-30}$	$< 10^{-30}$	0	0	$6 \times 10^{-6}$	$2 \times 10^{-9}$	$6 \times 10^{-10}$	0	0	$2 \times 10^{-5}$

$$\frac{\dot{a}}{2a} = \frac{\dot{J}_{\text{GW}}}{J_{\text{orb}}} - \frac{I_1(\Omega - \omega_1)}{J_{\text{orb}}\tau_1} - \frac{I_2(\Omega - \omega_2)}{J_{\text{orb}}\tau_2} - (q_a - q)\frac{\dot{M}_2}{M_2} \quad (4.9)$$

where

$$q_a \equiv 1 + M_2 \frac{j_2 - j_1}{J_{\text{orb}}} \quad (4.10)$$

In the disk-fed accretion approximation the specific angular momentum of the matter arriving to the accretor,  $j_1$ , can be approximated by:

$$j_1 = \sqrt{GM_1 R_1} \quad (4.11)$$

Finally, the angular momentum of the matter leaving the donor,  $j_2$ , can be expressed as (Gokhale et al. 2007):

$$j_2 \simeq R_2^2 \omega_2 \quad (4.12)$$

As can be seen, the term arising from the emission of gravitational waves will always lead to a decrease of the orbital separation, since  $\dot{J}_{\text{GW}} < 0$ . The tidal terms, that is the ones coming from the spin-orbit coupling, can contribute to increase or to decrease the orbital distance depending on the relation between the spin and orbital velocities. If a star is rotating faster than the binary, angular momentum will be transferred from the star to the orbit, thus leading to an increase in the orbital separation. On the contrary, if the star is rotating slower than the orbit, a transfer of angular momentum from the orbit to the star is produced, thus leading to a decrease of the orbital separation. The last term comes from the variation of angular momentum due to mass transfer, and can produce an increase or a decrease of the orbital separation depending on the specific angular momentum of the accreted material. It can be seen that if the mass-transfer rate leads to a decrease of the orbital separation this will in turn increase the mass transfer rate, thus leading to a runaway process ending with a dynamically unstable merging process. On the contrary if mass transfer leads to an increase of the orbital separation it will lead to a reduction of the mass transfer, thus stabilizing the merging process. As a consequence, it can be seen that it is possible for a system to change its mass-transfer type from stable to unstable or vice versa because  $q$  is a dynamical value. Thus, in order to determine the exact type of mass transfer of the system it is necessary to study how the mass-transfer rate evolves with time. The mass-transfer rate is determined by the Roche Lobe overfill factor  $\Delta$  which is usually defined as:

$$\Delta \equiv R_2 - R_L \quad (4.13)$$

Adopting a polytropic equation of state with  $n = 3/2$  for the donor star, the mass-transfer rate can be approximated by (Paczyński & Sienkiewicz 1972)

$$\dot{M}_2 = -\alpha W(\mu) \left( \frac{\Delta}{R_2} \right)^3 \quad (4.14)$$

being

$$W(\mu) = \frac{\sqrt{\mu}\sqrt{1-\mu}}{(\sqrt{\mu} + \sqrt{1-\mu})^4} \left( \frac{\mu}{R_1} \right)^3 \quad (4.15)$$

where  $\mu = M_2/(M_1 + M_2)$  and  $\alpha$  is a smoothly varying function of the stellar parameters which, following the approach of Gokhale et al. (2007), we have taken as a constant freely adjustable parameter.

Thus, in order to compute the exact value of the mass transfer rate, it is necessary to follow the time evolution of stellar radius  $R_1$  and  $R_2$  and the Roche Lobe radius,  $R_L$ . For the Roche lobe radius we have adopted the expression of Eggleton (1983):

$$R_L = \frac{0.49q^{2/3}}{0.6q^{2/3} + \ln(1 + q^{1/3})} \quad (4.16)$$

whereas its time evolution is given by (Gokhale et al. 2007):

$$\begin{aligned} \frac{\dot{R}_L}{2R_L} = \frac{\dot{J}_{\text{GW}}}{J_{\text{orb}}} &- \frac{I_1(\Omega - \omega_1)}{J_{\text{orb}}\tau_1} - \frac{I_2(\Omega - \omega_2)}{J_{\text{orb}}\tau_2} \\ &- \left( q_a - \frac{\zeta_{R_L}}{2} - q \right) \frac{\dot{M}_2}{M_2} \end{aligned} \quad (4.17)$$

where  $\zeta_{R_L} \approx 0.30 + 0.16q$  which is valid for  $0.01 \leq q \leq 1$  (Gokhale et al. 2007).

The calculation of stellar radius requires some care. Although the equilibrium radius of a white dwarf of a certain mass is well known, it should be taken into account that due to dynamics of the process stars are not in perfect hydrostatic equilibrium, especially in the last stages of our calculations. Consequently, equilibrium values cannot be used, since this might introduce strong errors in the calculations. Hence, we have adopted a different approach. We have computed for each time step the *actual* moment of inertia of each star. In particular, in the case of the primary white dwarf for each computed model we look for the location of the region with maximum temperature (see Fig. 4.3). We then compute the mass interior to this shell and the corresponding moment of inertia. For the case of the donor white dwarf we look for the region which still has an approximate spherical symmetry (see Fig. 4.1) and we follow the same procedure adopted for the accretor. Once we know the moment of inertia of the stars and given the masses we can compute an approximate value for the stellar radius.

With all these inputs the equations for the evolution of the binary system — Eqs. (4.9) and (4.17) — together with the equations for the evolution of the spin angular velocities of each of the components

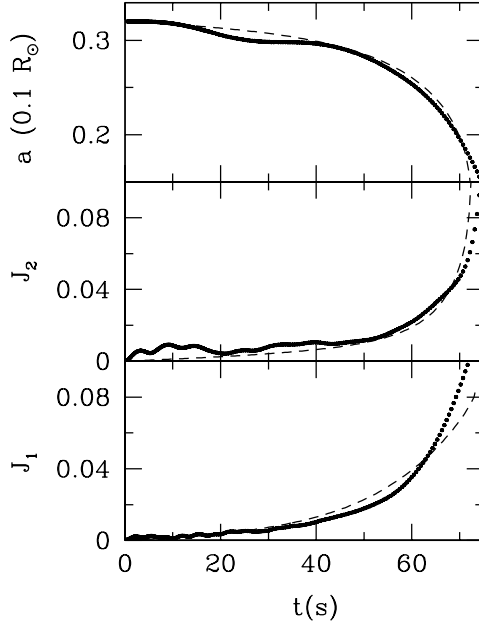


Figure 4.7: A comparison of the SPH values for the orbital distance  $a$  and for the spin angular moments of the donor and the accretor stars for the  $0.6 + 0.8 M_{\odot}$  case and those obtained using a simplified model. The spin angular moments are expressed in units of  $10^{51} \text{ g cm}^2/\text{s}$ .

$$\dot{\omega}_i = \left( \frac{j_i}{I_i} \right) \dot{M}_i - \left( \frac{\dot{I}_i}{I_i} \right) \omega_i + \frac{\Omega - \omega_i}{\tau_i} \quad (4.18)$$

can be integrated. In doing so it has to be taken into account the logical limitations of the theoretical approach. In particular, the SPH results show that mass transfer is not perfectly conservative, although this assumption is fairly good — see Table 4.1. Moreover, stars are not point-like masses and, most importantly, the method adopted for the calculation of the stellar radii presents some difficulties in the last moments of the simulation because of the very large degree of deformation of the secondary star. All these assumptions may produce marked differences between the SPH and the theoretical results.

In figure 4.7 we show a comparison of the theoretical results — shown as a dashed line — and the SPH results — shown as dots — for the time evolution of the orbital separation and of the spin angular moment of the accretor ( $J_1$ ) and donor stars ( $J_2$ ). The three adjustable parameters adopted in the theoretical calculations are, respectively,  $\alpha = 145 M_{\odot} R_{\odot}^3 \text{ yr}$ ,  $\tau_1^0 = 3.50 \times 10^4 \text{ yr}$  and  $\tau_2^0 = 4.7510^{-8} \text{ yr}$ . As can be seen, during the first phases of the merger the agreement is excellent. Note however

that we can only compare the SPH results with the theoretical expectations while the secondary still preserves partially its initial shape. This is why we only show in Fig. 4.7 a reduced time interval, corresponding to the first five panels in Figs. 4.1 and 4.3. For times longer than  $\sim 70$  s, the secondary rapidly dissolves and, hence, the approach followed here is no longer valid. It is worth realizing that  $\tau_1^0 \gg \tau_2^0$ . This means that the synchronization timescale of the primary is much larger than that of the secondary. Accordingly, during this phase of the mass-transfer episode the donor rapidly synchronizes whereas the primary does not. Consequently, orbital angular momentum is transferred from the orbit to the donor in a short timescale, thus reducing the orbital separation. This, in turn, increases the mass-transfer rate and the final result is that the secondary is rapidly disrupted. Since the total angular momentum is conserved the material transferred to the primary must rotate rapidly, thus producing the characteristic rotational profiles shown in the left panels of Fig. 4.5. In summary, the results of the hydrodynamic calculations can be accurately reproduced by a simple model once all the weaknesses of the theoretical approach are correctly taken into account.

#### 4.4.2 Gravitational wave radiation

Gravitational wave radiation from Galactic close white dwarf binary systems is expected to be the dominant contribution to the background noise in the low frequency region, which ranges from  $\sim 10^{-3}$  up to  $\sim 10^{-2}$  Hz (Bender 1998). Moreover, since during the merging process a sizeable amount of mass is transferred from the donor star to the primary at considerable speeds, the gravitational wave signal is expected to be detectable by LISA (Guerrero et al. 2004; Lorén-Aguilar et al. 2005). It is thus important to characterize which would be the gravitational wave emission of the white dwarf mergers studied here and to assess the feasibility of detecting them.

To compute the gravitational wave pattern we proceed as in Lorén-Aguilar et al. (2005). In particular, we use the weak-field quadrupole approximation (Misner et al. 1973):

$$h_{jk}^{\text{TT}}(t, \vec{x}) = \frac{2G}{c^4 d} \frac{\partial^2 Q_{jk}^{\text{TT}}(t - R)}{\partial t^2} \quad (4.19)$$

where  $t - R = t - d/c$  is the retarded time,  $d$  is the distance to the observer, and  $Q_{jk}^{\text{TT}}(t - R)$  is the quadrupole moment of the mass distribution, which is given by

$$\ddot{Q}_{jk}^{\text{TT}}(t - R) = \int \rho(\vec{x}, t - R) \left( x^j x^k - \frac{1}{3} x^2 \delta_{jk} \right) d^3 x \quad (4.20)$$

To calculate the quadrupole moment of the mass distribution using SPH particles, Eq. (4.20) must be discretized according to the following expression

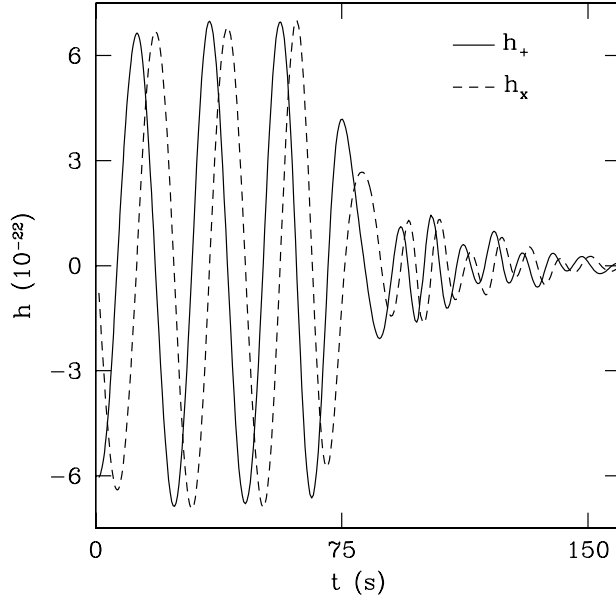


Figure 4.8: Gravitational wave emission from the merger of a  $0.6 + 0.8 M_{\odot}$  close white dwarf binary system. The dimensionless strains  $h_+$  and  $h_{\times}$  are measured in units of  $10^{-22}$ . The source has been assumed to be at a distance of 10 kpc.

$$\begin{aligned} \ddot{Q}_{jk}^{\text{TT}}(t - R) &\approx P_{ijkl}(\vec{N}) \sum_{p=1}^n m(p) [2\vec{v}^k(p)\vec{v}^l(p) \\ &+ \vec{x}^k(p)\vec{a}^l(p) + \vec{x}^l(p)\vec{a}^k(p)] \end{aligned} \quad (4.21)$$

where

$$\begin{aligned} P_{ijkl}(\vec{N}) &\equiv (\delta_{ij} - N_i N_j)(\delta_{kl} - N_k N_l) \\ &- \frac{1}{2}(\delta_{ij} - N_i N_j)(\delta_{kl} - N_k N_l) \end{aligned} \quad (4.22)$$

is the transverse-traceless projection operator onto the plane orthogonal to the outgoing wave direction,  $\vec{N}$ ,  $m(p)$  is the mass of each SPH particle, and  $\vec{x}(p)$ ,  $\vec{v}(p)$  and  $\vec{a}(p)$  are, respectively, its position, velocity and acceleration.

Using this prescription the corresponding strains for the  $0.6 + 0.8 M_{\odot}$ , which is a representative case, are shown in Fig. 4.8. As shown in this figure the gravitational waveforms rapidly vanish in a couple of orbital periods and the gravitational wave emission during the coalescence phase does not have a noticeable large peak.

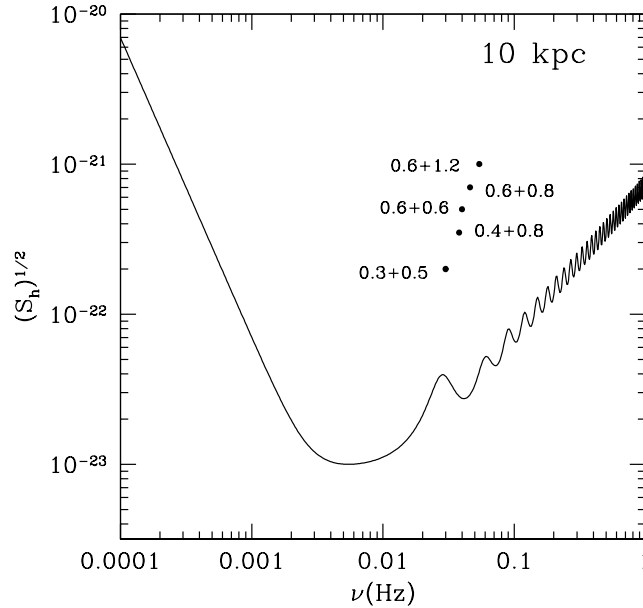


Figure 4.9: A comparison of the signal produced by the close white dwarf binary systems studied here, when a distance of 10 kpc is adopted. The spectral distribution of noise of LISA for a one year integration period is also shown. We have adopted a signal-to-noise ratio  $\eta = 5$ .

Hence, the gravitational wave emission is dominated by the chirping phase, in agreement with the findings of Lorén-Aguilar et al. (2005). Moreover, the gravitational waveforms obtained here are very similar to those computed by Lorén-Aguilar et al. (2005) and, thus, do not depend appreciably on the number of particles used to calculate them. Since the gravitational wave signal is dominated by that of the inspiralling phase, in order to assess the feasibility of detecting it using gravitational wave detectors we have assumed that the orbital separation of the binary system is that of the last stable orbit. Furthermore, we have also assumed that the integration time of LISA will be one year. It is then straightforward to demonstrate that during this time interval the variation of the orbital separation is negligible. With these assumptions the double white dwarf binary system basically radiates a monochromatic wave and it is easy to assess the feasibility of detecting the signal produced by the coalescence of close binary white dwarf systems. This is done in figure 4.9 where we show the strength of the resulting signals and we compare them with the spectral distribution of noise of LISA, when a distance of 10 kpc is adopted. As can be seen in this figure all the systems are well inside the detectability region and, consequently, LISA should be able to distinguish them from Galactic noise.

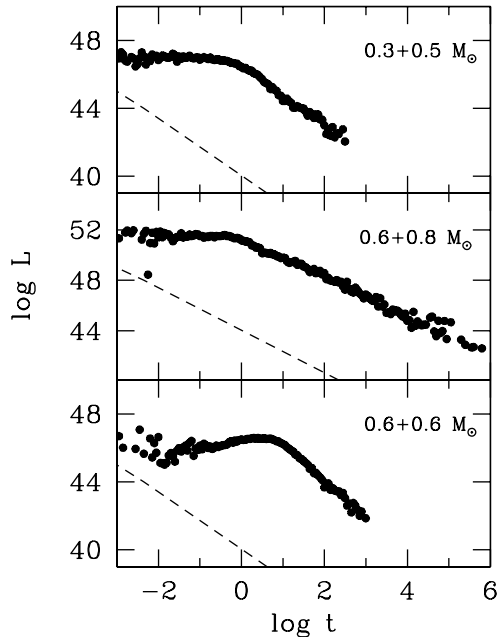


Figure 4.10: Fallback accretion luminosity for our three fiducial double white dwarf mergers. The units of time are seconds, whereas those of luminosities are erg/s. A straight line with slope 5/3 is shown for the sake of comparison.

#### 4.4.3 Fallback luminosities

Another potential observational signature of the mergers studied here is the emission of X-rays from the fallback material in the aftermath of the coalescence itself. We have already shown that as a result of the merger of two white dwarfs of different masses, most of the SPH particles of the disrupted secondary form a keplerian disk. These SPH particles have circularized orbits. However, as it occurs in the mergers of double neutron stars, some material of the secondary is found to be in highly eccentric orbits as well. After some time, this material will most likely interact with the recently formed disk. As discussed in Rosswog (2007) the timescale for this is not set by viscous dissipation but, instead, by the distribution of eccentricities. We follow closely the model proposed by Rosswog (2007) and calculate the accretion luminosity obtained from the interaction of the stellar material with high eccentricities with the newly formed disk by assuming that the kinetic energy of these particles is dissipated within the radius of the debris disk.

In figure 4.10 we have plotted the accretion luminosities as a function of time for our three fiducial cases. We emphasize that these luminosities have been computed assuming that the highly eccentric particles lose all its kinetic energy when interacting with the disk, for which we adopt the radius obtained by the end of our

SPH simulations, which are those shown in Table 4.1. Moreover, only a fraction of this energy will be released in the form of high-energy photons. Thus, the results shown in Fig. 4.10 can be regarded as an *upper limit* for the actual luminosity of high-energy photons. Note that although the luminosities are smaller than those typically obtained for the merger of double neutron stars — which are typically of the order of  $\sim 10^{52}$  erg/s — white dwarfs mergers predict a very similar time dependence ( $\propto t^{5/3}$ ). This is an important result because it shows that observations of high-energy photons can help in detecting the gravitational wave signal radiated by these systems. In fact, the detection of the gravitational waves arising from the merger of white dwarfs is a tough task because, as previously explained, the signal is dominated by the inspiralling phase and the waveforms do not have a prominent peak before the ringdown phase. Thus a combined strategy in which optical, UV, X-ray and gravitational wave detectors are used could be very useful.

#### 4.4.4 Long-term evolution

We have already shown that no explosive nuclear burning takes place during the merging phase. However, this does not necessarily mean that such an explosion could not take place due to mass accretion from the disk at late times. If mass accretion occurs at rates smaller than  $10^{-6} M_{\odot} \text{ yr}^{-1}$  then, central carbon ignition is possible and a SNIa is the most probable outcome. On the other hand, if the accretion rates are larger than this value, then off-center carbon ignition is the most probable outcome, giving rise to an inward propagating burning flame and an ONe white dwarf is likely to be formed (Nomoto & Iben 1985; Garcia-Berro & Iben 1994; Ritossa et al. 1999) which might eventually form a neutron star by accretion-induced collapse (Saio & Nomoto 1985; Woosley & Weaver 1986; Gutierrez et al. 1996; Gutiérrez et al. 2005). However, once the disk has been formed, angular momentum viscous transfer is relevant and the hydrodynamical timescale of the disk becomes very large. Consequently, the subsequent evolution of the disk cannot be followed using a SPH code. However, some estimates of the accretion rate can still be done by considering the typical viscous transport timescales.

The typical viscous transport timescale is (Mochkovitch & Livio 1989, 1990)

$$\tau_{\text{visc}} = \left( \frac{1}{T} \frac{dT}{dt} \right)^{-1} \quad (4.23)$$

where  $T$  is the rotational kinetic energy and

$$\frac{dT}{dt} = - \int \left( \frac{\partial \Omega}{\partial r} \right)^2 r^2 \eta(r) d^3r \quad (4.24)$$

is its rate of change. In this expression  $\Omega$  is the angular velocity,  $r$  is the radial cylindrical coordinate and  $\eta$  is the (physical) viscosity parameter, that depends on the viscous mechanism. If the disk is laminar and the viscosity is that of degenerate

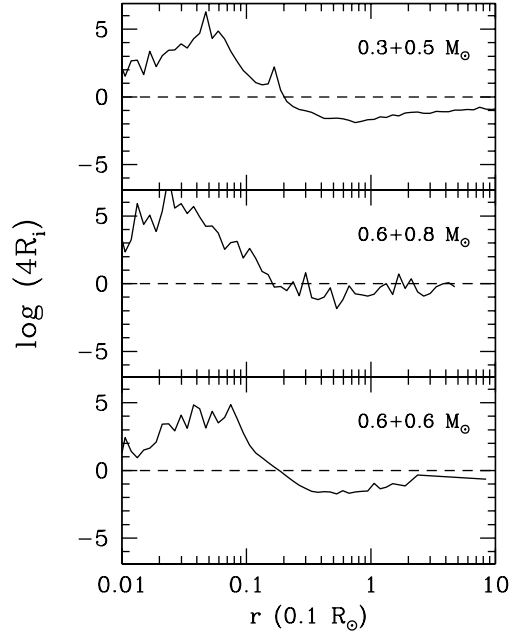


Figure 4.11: Richardson number as a function of the distance. When  $Ri > 1/4$  the disk is turbulent. The horizontal dashed line corresponds to  $Ri=1/4$ .

electrons then  $\eta = 2.0 \times 10^{-5} \rho^{5/3} \text{ g/cm s}$  (Durisen 1973, Itoh et al. 1987) and the associated accretion rates can be obtained taking into account that

$$\dot{T} \sim \frac{GM_* \dot{M}}{R_*} \quad (4.25)$$

where  $M_*$  and  $R_*$  are the mass and radius of the central object. If, instead, the disk is turbulent the classical approximation of Shakura & Syunyaev (1973) is valid. Within this approximation the viscous timescale is given by

$$\tau_{\text{visc}} = \alpha^{-1} \left( \frac{R_{\text{disk}}}{H} \right) \left( \frac{R_{\text{disk}}}{c_s} \right) \quad (4.26)$$

where  $\alpha \sim 0.1$  is the standard viscosity,  $c_s$  is the sound speed,  $R_{\text{disk}}$  is the radius of the disk and  $H$  is the disk half-thickness. Both the radius of the disk and its half-thickness are listed in Table 4.1 for each one of the simulations presented here. The accretion rate is then given by

$$\dot{M} \simeq \frac{M_{\text{disk}}}{\tau_{\text{visc}}} \quad (4.27)$$

In order to check if the disk is turbulent we have computed the Richardson number

Table 4.3: Typical viscous timescales (in years), dissipated kinetic energies (in erg/s), and accretion rates (in  $M_{\odot} \text{ yr}^{-1}$ ) for the case in which the laminar viscosity is used. Columns 5 and 6 show the corresponding viscous timescales and accretion rates obtained when the classical Shakura & Syunyaev (1973) expression is employed.

Run	Laminar			Turbulent	
	$\tau$	$\dot{T}$	$\dot{M}$	$\tau$	$\dot{M}$
0.3+0.5	$3 \times 10^{11}$	$1 \times 10^{29}$	$2 \times 10^{-14}$	$7.6 \times 10^{-4}$	43
0.4+0.8	$1 \times 10^{11}$	$5 \times 10^{29}$	$8 \times 10^{-14}$	$1.1 \times 10^{-2}$	63
0.6+0.6	$1 \times 10^{11}$	$6 \times 10^{29}$	$1 \times 10^{-13}$	$2.0 \times 10^{-4}$	560
0.6+0.8	$5 \times 10^{10}$	$3 \times 10^{30}$	$4 \times 10^{-13}$	$1.2 \times 10^{-2}$	62
0.6+1.2	$3 \times 10^8$	$7 \times 10^{32}$	$8 \times 10^{-11}$	$1.0 \times 10^{-2}$	75

$$\text{Ri} = \frac{\left(\frac{g^{\text{eff}}}{c_s}\right) \left(1 - \frac{\gamma}{\Gamma}\right)}{\left(r \frac{d\Omega}{dr}\right)} \quad (4.28)$$

In this expression  $g^{\text{eff}}$  is the effective gravity, that is the real gravity minus the centrifugal force,  $\gamma$  is the logarithmic derivative of the pressure with respect to the density,  $\Gamma$  is the adiabatic and the rest of the symbols have their usual meaning. We have chosen  $\gamma = 1.4$  and  $\Gamma = 5/3$ . If the Richardson number is smaller than  $1/4$  stability against turbulence is guaranteed. If this is not the case the disk may be turbulent, since this is only a necessary condition, but  $\text{Ri} > 1/4$  is a good indication for turbulence to occur. In figure 4.11 we show the Richardson number as a function of the radial coordinate for the three fiducial cases described here. As can be seen in this figure the condition  $\text{Ri} > 1/4$  is satisfied in the innermost regions of the disk, up to distances  $\sim 0.2 R_{\odot}$ . Thus, the innermost regions of the disk are turbulent and it is likely that the accretion rate is that given by Eq. (4.27). Nevertheless, Eq. (4.23) provides a safe upper limit for the typical transport timescale of the disk. The total rotational kinetic luminosity dissipated,  $\dot{T}$ , and the corresponding timescales using this approach are given in the left section of table 4.3. For the case in which the laminar viscosity is used the resulting accretion rates turn out to be  $\leq 10^{-12} M_{\odot}/\text{yr}$ , and consequently central carbon ignition leading to a SNIa is possible. When the classical Shakura & Syunyaev (1973) expression is adopted the accretion rates are shown in the right section of table 4.3. As can be seen these accretion rates turn out to be very large. There are experimental and theoretical reasons to suspect that the central object will not be able to accrete material from the surrounding disk at these very high accretion rates. From a theoretical perspective it is rather clear that these accretion rates exceed the Eddington limit, which is order of  $10^{-5} M_{\odot} \text{ yr}^{-1}$ . Additionally, and from a experimental point of view, there is growing evidence (Ji

et al. 2006) that hydrodynamic turbulence cannot transport angular momentum effectively in astrophysical disks, even at very large Reynolds numbers, leaving as the only possible way to lose angular momentum the magnetorotational instability.

Yoon et al. (2007) have systematically explored the conditions for avoiding off-center carbon ignition in the merged configurations resulting from the coalescence of two CO white dwarfs. They computed the evolution of the central remnant of the coalescence of a  $0.9 + 0.6 M_{\odot}$  binary white dwarf, adopting a realistic initial model, which includes the differentially rotating primary, the hot envelope we also find in our simulations and the centrifugally supported accretion disk. Our final configurations resemble very much those found by these authors and, consequently, the same conclusions obtained in this paper hold. In particular, since in our models the maximum temperature of the hot envelope is smaller than the carbon ignition temperature and the mass-accretion rate from the keplerian disk is possibly smaller than the critical one ( $\dot{M} \simeq 5.0 \times 10^{-6} M_{\odot} \text{ yr}^{-1}$ ) it is probable that at least some of our merged configurations may be considered good candidates for the progenitors of Type Ia supernovae.

## 4.5 Conclusions

We have performed several high-resolution Smoothed Particle Hydrodynamics simulations of coalescing white dwarfs. We have done so for a broad range of masses and chemical compositions of the coalescing white dwarfs, which includes He, CO and ONe white dwarfs. Such a parametric study using a large number of particles ( $4 \times 10^5$  SPH particles) had never been done before. Previous works on the subject used a considerably smaller number — by a factor of 10 — of SPH particles (Guerrero et al. 2004), or did not explore the full range of masses and chemical compositions of interest (Yoon et al. 2007) — only one merger was computed, that of  $0.9 + 0.6 M_{\odot}$  double white dwarf. In addition, we have included a refined treatment of the artificial viscosity. In particular, we have used an artificial viscosity formulation that is oriented at Riemann-solvers (Monaghan 1997) together with time dependent viscosity parameters and an additional switch to suppress the excess of viscosity (Balsara 1995). With this treatment the dissipative terms are only applied in those regions of the fluid in which they are really necessary to resolve a shock. This refined treatment of the artificial viscosity overcomes some of the problems found in our previous simulations (Guerrero et al. 2004).

In all cases, the merged configuration consists of a compact central object surrounded by a hot corona with spheroidal shape and a self-gravitating keplerian disk around it. For the cases in which two white dwarfs of different masses are involved the resulting disk can be considered as a thin disk, whereas for the  $0.6 + 0.6 M_{\odot}$  case we have found that the resulting final configuration resembles a rotating ellipsoid around the central object with a much more modest disk. The peak temperatures

attained during the merger are smaller than those found by Guerrero et al. (2004) and in line with that found by Yoon et al. (2007) for the case of a  $0.9 + 0.6 M_{\odot}$  merger. We also confirm the results obtained in previous works (Guerrero et al. 2004; Lorén-Aguilar et al. 2005; Yoon et al. 2007) and we find that only when one of the merging white dwarfs is a He white dwarf nuclear reactions are relevant. However none of the cases studied here show an explosive behavior during the merging phase. Furthermore, no essential differences are found when the chemical abundances obtained here using an enhanced spatial resolution and a refined prescription for the artificial viscosity and those obtained in previous works (García-Berro et al. 2007) are compared. The chemical composition of the disks formed by the coalescence of a He white dwarf with CO white dwarfs shows an enrichment in heavy elements like Ca, Mg, S, Si and Fe and constitute a natural environment where planets and asteroids can be formed. This could explain the anomalous abundances of metals found in several hydrogen-rich white dwarfs with dusty disks around them and which have been attributed to the impact of asteroids (Jura 2003), since it is quite unlikely that such asteroids could survive the red giant phase.

We have also compared the results of our hydrodynamical calculations with the theoretical expectations and we have found a satisfactory agreement when the synchronization timescale of the disrupted secondary is much shorter than that of the primary. In this case the rate of change of the orbital distance and the corresponding spins of both the donor star and of the accretor are reproduced with a large degree of accuracy. We have shown as well that the emission of gravitational waves from these kind of systems is strong enough to be observable by LISA, and that the corresponding waveforms do not depend appreciably on the resolution employed in the hydrodynamical calculations and, thus, that these waveforms are robust.

We have computed as well the possible X-ray emission produced in the aftermath of the merger. This X-ray emission is a consequence of the interaction of the material with highly eccentric orbits — which is produced during the first and most violent phases of the merger — with the resulting disk — which is formed by particles with circularized orbits — and we have found that the typical luminosities are of the order  $\sim 10^{49}$  erg/s, although the precise value of the peak luminosity depends very much on the masses of the coalescing white dwarfs. The time dependence of the X-ray emission is  $\propto t^{5/3}$ , a behavior also present in the merger of double neutron stars and neutron stars and black holes (Rosswog 2007). The detection of this X-ray burst would eventually help in detecting the gravitational waves supposedly radiated during the merger.

With respect to the long-term evolution of the mergers we have found that all the disks product of the coalescence of two white dwarfs are potentially turbulent. This result implies that very large accretion rates from the disk onto the primary are expected. Despite our crude approximations, it is thus quite likely that these accretion rates would lead to an off-center carbon ignition, although an in depth study remains to be done. However, since our final configurations resemble very

much those found by Yoon et al. (2007), it is as well probable that at least some of our merged configurations may be considered good candidates for the progenitors of Type Ia supernovae. A detailed calculation of the evolution of the resulting disks, including an accurate description of the mechanisms of angular momentum transport, must therefore be done. Unfortunately this task is far beyond the current possibilities of SPH techniques.

## Chapter 5

# Evidence of a merger of binary white dwarfs: the case of GD 362

GD 362 is a massive white dwarf with a spectrum suggesting a H-rich atmosphere which also shows very high abundances of Ca, Mg, Fe and other metals. However, for pure H-atmospheres the diffusion timescales are so short that very extreme assumptions have to be made to account for the observed abundances of metals. The most favored hypothesis is that the metals are accreted from either a dusty disk or from an asteroid belt. Here we propose that the envelope of GD 362 is dominated by He, which at these effective temperatures is almost completely invisible in the spectrum. This assumption strongly alleviates the problem, since the diffusion timescales are much larger for He-dominated atmospheres. In this chapter we compare the results of our simulations to the recent observations of GD 362. We report the abundances of the resulting accretion disk, and we discuss the possibility of explaining both the accretion disk and the high metal abundances found in GD 362 as the coalescence of a double white dwarf binary system. We have explored a significant range of masses for the primary, but we concentrate on secondaries with masses  $M \leq 0.45 M_{\odot}$ , although we also show, for the sake of comparison the emerging chemical composition of the coalescence of a close binary system in which the two components are carbon-oxygen white dwarfs.

### 5.1 Introduction

GD 362 is a massive, rather cool ( $T_{\text{eff}} \simeq 9740 \pm 50$  K), white dwarf with a heavy accretion disk surrounding it (Kilic et al. 2005; Becklin et al. 2005; Gianninas et al. 2004). The dusty disk around GD 362 produces an excess of infrared radiation which amounts to  $\sim 3\%$  of the total stellar luminosity. The chemical composition of GD 362

Run	$M_{\text{WD}}$	$M_{\text{disk}}$	$M_{\text{acc}}$	$M_{\text{ej}}$	$\omega$ (s <sup>-1</sup> )	$J_z^{\text{SPH}}$	$J_z$
0.4+0.8	0.99	0.21	0.19	10 <sup>-3</sup>	0.61	$2.4 \times 10^{-5}$	$2.4 \times 10^{-5}$
0.4+1.0	1.16	0.24	0.16	10 <sup>-3</sup>	1.00	$3.0 \times 10^{-5}$	$2.9 \times 10^{-5}$
0.4+1.2	1.30	0.30	0.10	10 <sup>-3</sup>	1.72	$4.0 \times 10^{-5}$	$3.9 \times 10^{-5}$
0.6+0.6	0.90	0.30	0.90	10 <sup>-2</sup>	0.21	$2.5 \times 10^{-5}$	$3.2 \times 10^{-5}$
0.6+0.8	1.09	0.29	0.29	10 <sup>-3</sup>	0.49	$3.4 \times 10^{-5}$	$3.4 \times 10^{-5}$

Table 5.1: Main results of the SPH simulations of Guerrero et al. (2004) All masses are in solar units, whereas the units of the angular momentum are  $M_{\odot}R_{\odot}^2/\text{s}$ .

is also rather singular, showing very high abundances of Ca, Mg and Fe (Gianninas et al. 2004). Thus, it is classified as a massive DAZ (hydrogen-rich) white dwarf. The origin of such particularly high photospheric abundances —  $\log(N_{\text{Ca}}/N_{\text{H}}) = -5.2$ ,  $\log(N_{\text{Mg}}/N_{\text{H}}) = -4.8$  and  $\log(N_{\text{Fe}}/N_{\text{H}}) = -4.5$  — and of the surrounding dusty disk still remains a mystery and it is the matter of an active ongoing debate. In particular, since the diffusion timescales for metals in H-rich white dwarfs are of only a few years (Koester & Wilken 2006) very extreme assumptions have to be made in order to explain these abundances. At present the most widely accepted scenario is disruption and accretion of a planetary body, although for this scenario to be feasible the planetary system should survive during the advanced stages of stellar evolution, which by no means is guaranteed. The formation of an asteroid would require the previous existence of a disk around this white dwarf (Livio et al. 1992, 2005). Particularly, a recent analysis (Villaver & Livio 2007) has shown that planets around white dwarfs with masses  $M_{\text{WD}} > 0.7 M_{\odot}$  are generally expected to be found at orbital radii  $r > 15$  AU because they cannot survive the planetary nebula phase and that if planets are to be found at smaller orbital radii around massive white dwarfs, they had to form as the result of the merger of two white dwarfs. It is also interesting to note that there have been previous suggestions about white dwarfs that are merger products — see for instance Liebert et al. (2005) — but these claims do not have yet any observational support.

## 5.2 Characteristics of the merger products

One of the possibilities is that this massive white dwarf is the result of the merger of a double white dwarf close binary system. Indeed, the merger of two white dwarfs is one of the outcomes of binary star evolution. This scenario has been recently studied by Guerrero et al. (2004) and Lorén-Aguilar et al. (2005) using an up-to-date Smoothed Particle Hydrodynamics code and employing the adequate spatial resolution. Also, the nucleosynthesis of the merger was carefully studied in these papers. The main results of such simulations is that the less massive white dwarf of the binary system is totally disrupted in a few orbital periods. A fraction of the secondary is directly

Run	0.4+0.8	0.4+1.0	0.4+1.2	0.6+0.6	0.6+0.8
He	0.94	0.93	0.99	0	0
C	$3 \times 10^{-2}$	$2 \times 10^{-2}$	$5 \times 10^{-3}$	0.4	0.4
O	$1 \times 10^{-2}$	$3 \times 10^{-3}$	$3 \times 10^{-3}$	0.6	0.6
Ca	$4 \times 10^{-5}$	$2 \times 10^{-4}$	$9 \times 10^{-6}$	0	0
Mg	$3 \times 10^{-5}$	$3 \times 10^{-5}$	$6 \times 10^{-6}$	0	0
S	$8 \times 10^{-5}$	$2 \times 10^{-4}$	$5 \times 10^{-7}$	0	0
Si	$1 \times 10^{-4}$	$2 \times 10^{-4}$	$3 \times 10^{-5}$	0	0
Fe	$9 \times 10^{-3}$	$7 \times 10^{-3}$	$5 \times 10^{-4}$	0	0

Table 5.2: Averaged chemical composition (by mass) of the heavy-rotationally supported disk obtained by the end of the coalescing process.

accreted onto the primary white dwarf whereas the remnants of the secondary form a heavy, rotationally-supported accretion disk around the primary and little mass is ejected from the binary system. The resulting temperatures are rather high ( $9 \times 10^8$  K) during the most violent phases of the merger process, allowing for extensive nuclear processing. The enhancement of the abundances of the most relevant nuclear isotopes occurs when one of the coalescing white dwarfs is made of pure He. This stems from two facts. First, the Coulomb barrier is much smaller in this case leading to enhanced abundances of Ca, Mg and Fe and, second, the secondary is less compact leading larger kinetic energies of the disrupted secondary and, consequently, to a stronger impact of the accreted matter on the surface of the primary resulting in larger temperatures of the shocked material.

Table 5.1 shows the main results of the SPH simulations discussed in detail in Guerrero et al. (2004). The first column displays the masses of the coalescing white dwarfs, in the second column the mass of the resulting white dwarf is listed. The mass of the rotationally-supported disk emerging from the simulations is tabulated in column three. The fourth column provides the accreted mass, whereas in column five the mass ejected from the system is given. Finally columns six and seven list the rotational velocity of the surface of the central object and the total orbital angular momentum stored in the disk. Note that in this table, as predicted by the standard theory of stellar evolution, white dwarfs with masses smaller than  $0.45 M_{\odot}$  are assumed to be made of pure He, white dwarfs with masses larger than  $1.0 M_{\odot}$  are considered to be ONe white dwarfs and white dwarfs with masses  $0.45 M_{\odot} \leq M \leq 1.0 M_{\odot}$  are considered to be made of carbon and oxygen. As can be seen, in all cases the primary is considerably spun-up during the merger, although — as discussed in Guerrero et al. (2004) — this may be an artifact of the adopted artificial viscosity and should then be considered as a safe upper limit. Also interesting to note is that approximately half of the mass of the disrupted secondary is directly accreted by the primary, whereas most of the remnants of the secondary form an accretion disk with

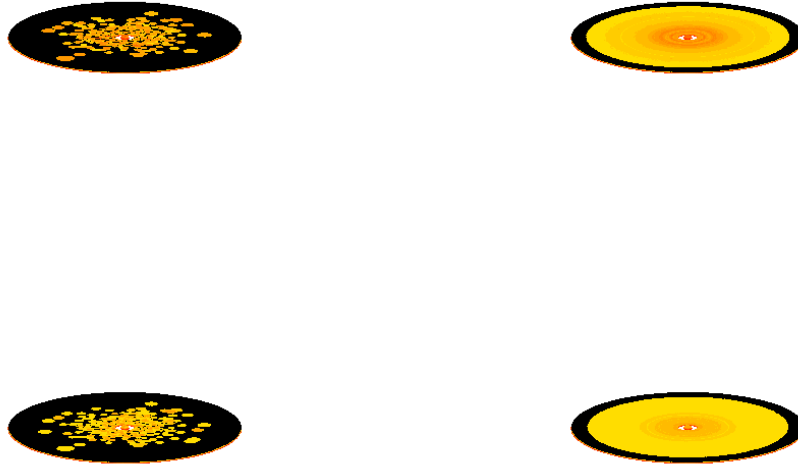


Figure 5.1: Abundances by mass of Ca (top) and Mg (bottom). The left panels show the distribution profile projected on the orbital plane, whereas the right panels show the angular average.

a rather high orbital angular momentum.

Table 5.2 shows the averaged chemical composition of the resulting accretion disk, whereas table 5.3 shows the maximum local chemical composition of the disk. For the cases in which a secondary of mass  $0.4 M_{\odot}$  is adopted the major constituent of the disk is He. For the rest of the cases studied here the most abundant isotopes are C and O. Note that for the case in which a He white dwarf is disrupted the chemical enrichment in Ca, Mg Fe and Si is rather noticeable, leaving open the possibility of explaining the rather high photospheric abundances of these elements found in GD 362 by direct accretion from the disk. To this regard in figures 5.1 and 5.2 we show, respectively, the distribution of the projected abundances of Ca (figure 5.1, top panels), Mg (figure 5.1, bottom panels), Si (figure 5.2, top panels) and Fe (figure 5.2, bottom panels). In both figures the left panels represent the computed distribution of abundances as it results from our SPH calculations, whereas in the right panels we have averaged this abundances over an annulus.

It is worth noticing that the distribution of the different elements in the disk

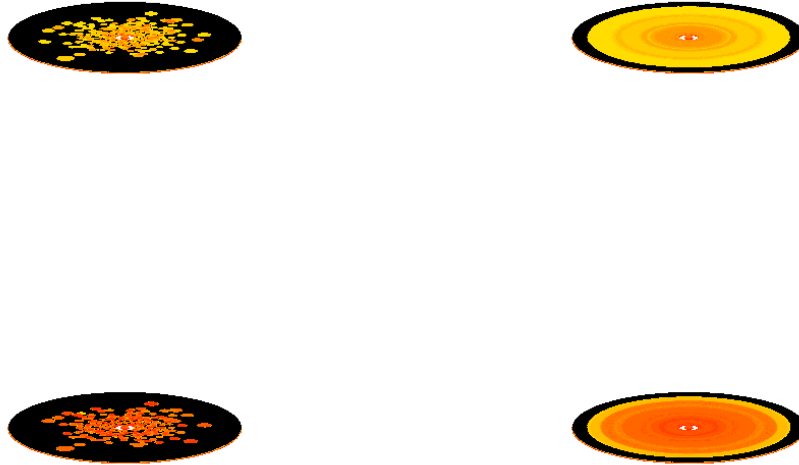


Figure 5.2: Abundances by mass of Si (top) and Fe (bottom). The left panels show the distribution profile projected on the orbital plane, whereas the right panels show the angular average.

is rather inhomogeneous, as already apparent from figures 5.1 and 5.2. Obviously those parts of the disk in which the material of the secondary has been shocked have undergone major nuclear processing. Hence, these regions are C- and O-depleted and Si- and Fe-enhanced. In fact, the innermost regions ( $R < 0.1 R_{\odot}$ ) of the merged object, which have approximately the shape of an ellipsoid, are C- and O-rich. It is expected that this region would be eventually accreted during the first moments of the cooling phase of the central object, leading to a more massive white dwarf. We also find that the abundance of intermediate-mass and iron-group elements is considerably larger than that of C and O in the remnants of the accretion stream which are at larger distances.

In order to correctly address whether or not the high photospheric abundances of GD 362 are the product of a merger of a binary white dwarf system we must first compute the mass of the envelope of GD 362. To this end it is important to realize that during the merger process the (tiny) H envelopes of the merging white dwarfs are completely destroyed as a consequence of the large temperatures achieved in the

Run	0.4+0.8	0.4+1.0	0.4+1.2	0.6+0.6	0.6+0.8
He	1.0	1.0	1.0	0	0
C	$4 \times 10^{-1}$	$3 \times 10^{-1}$	$4 \times 10^{-1}$	$4 \times 10^{-1}$	$4 \times 10^{-1}$
O	$6 \times 10^{-1}$	$6 \times 10^{-1}$	$8 \times 10^{-1}$	$6 \times 10^{-1}$	$6 \times 10^{-1}$
Ca	$4 \times 10^{-3}$	$2 \times 10^{-2}$	$3 \times 10^{-3}$	0	0
Mg	$7 \times 10^{-4}$	$6 \times 10^{-2}$	$2 \times 10^{-3}$	0	0
S	$1 \times 10^{-2}$	$7 \times 10^{-3}$	$7 \times 10^{-3}$	0	0
Si	$3 \times 10^{-2}$	$6 \times 10^{-3}$	$8 \times 10^{-3}$	0	0
Fe	$8 \times 10^{-2}$	$6 \times 10^{-2}$	$2 \times 10^{-1}$	0	0

Table 5.3: Maximum local chemical composition (by mass) of the heavy-rotationally supported disk obtained by the end of the coalescing process.

outermost regions of the remnant white dwarf. Hence, GD 362 must have accreted at least part of its envelope from the ISM. We will come back to this issue in the next section. For the moment it is as well important to study the resulting disks.

Following Livio et al. (2005) the surface density profile of the disk is of the form  $\Sigma \propto R^{-\alpha}$ . Fig. 5.3 shows the resulting density profile of the disk (dots) for the  $0.4 + 1.0 M_{\odot}$  run and the fit obtained using  $\alpha = 7/4$  (line), which is very close to the value adopted by Livio et al. (2005),  $\alpha = 3/2$ . Note that the inner edge of the disk is located at  $\sim 1.0 \times 10^{-2} R_{\odot}$ . Then, it can be shown that the angular momentum of the disk can be expressed in terms of the disk radius  $R_{\text{out}}$  and the disk mass  $M_{\text{disk}}$  as

$$J_z = \xi M_{\text{disk}} (GM_{\text{WD}} R_{\text{out}})^{1/2} \quad (5.1)$$

where  $\xi = (2 - \alpha) / (\frac{5}{2} - \alpha) = 1/3$ . As can be seen in table 5.1 the predicted angular momentum using Eq. 5.1 — last column — agrees very well with the results of our SPH simulations. This provides confidence in our theoretical simulations. In all the cases we have used  $R_{\text{out}} \simeq 0.3 R_{\odot}$ , as it results from our detailed SPH simulations. For illustrative purposes in Fig. 5.4 we also show the temperatures in the disk by the end of our simulations — when the effective temperature is rather high — and we compare them with the theoretical profile (Chiang & Goldreich 1997).

## 5.3 Results

### 5.3.1 The chemical abundances

If the photospheric abundances of GD 362 are to be explained with this scenario the accretion of He-rich material is required. Since He is also accreted onto the surface of GD 362, the photospheric layers may contain significant amounts of He which, at the effective temperature of GD 362 would be spectroscopically invisible.

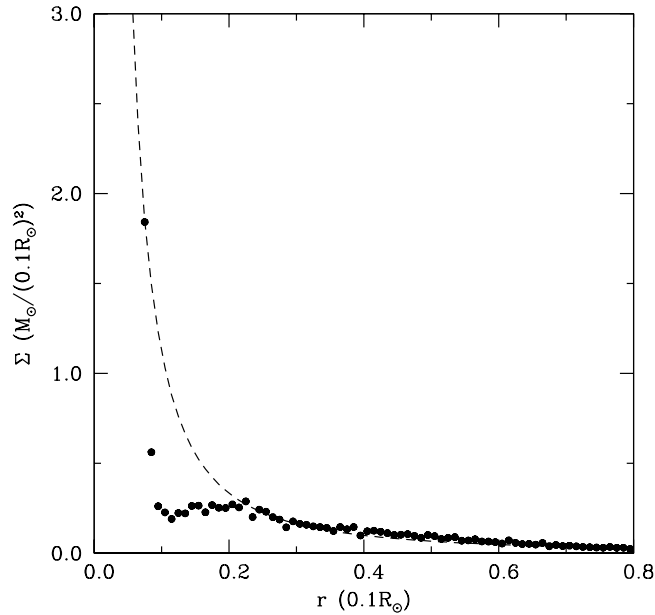


Figure 5.3: Surface density profile of the resulting disk (dots) compared to an exponentially decreasing law with an exponent of  $\alpha = 7/4$ . Only the innermost regions of the disk are shown.

Consequently, the H/He ratio can be regarded as a free parameter. However, the presence of He in a cool hydrogen-rich atmosphere affects the mass determination (Bergeron et al. 1991). For instance, in Fig. 5.5 we show three almost identical synthetic spectra representative of GD 362 with various assumed He abundances. If  $\text{He}/\text{H}=10$  is adopted then  $\log g = 8.25$  is obtained ( $M_{\text{WD}} \simeq 0.8 M_{\odot}$ ) whereas if we adopt  $\text{He}/\text{H}=1$  then the surface gravity turns out to be  $\log g = 8.72$ . This corresponds to a mass of the primary of  $M_{\text{WD}} \simeq 1.0 M_{\odot}$  which can be obtained from the coalescence of a  $0.4 + 0.8 M_{\odot}$  binary system. Additionally, in this case the largest abundances of the relevant elements are obtained. Thus, we choose the  $0.4 + 0.8 M_{\odot}$  simulation as our reference model.

In order to know whether the chemical abundances of GD 362 can be reproduced by direct accretion from the keplerian disk we proceed as follows. First, given the surface gravity and the effective temperature of our model we compute the luminosity, the radius and the cooling time of the white dwarf according to a set of cooling sequences (Salaris et al. 2000). We obtain respectively  $\log(L_{\text{WD}}/L_{\odot}) \sim -3.283$ ,  $\log(R_{\text{WD}}/R_{\odot}) \sim -2.096$ , and  $t_{\text{cool}} \sim 2.2$  Gyr. Hence, in this scenario GD 362 has had enough time from the moment in which the merger occurred to cool down enough for the accretion disk to settle down, loose some mass — even at a very

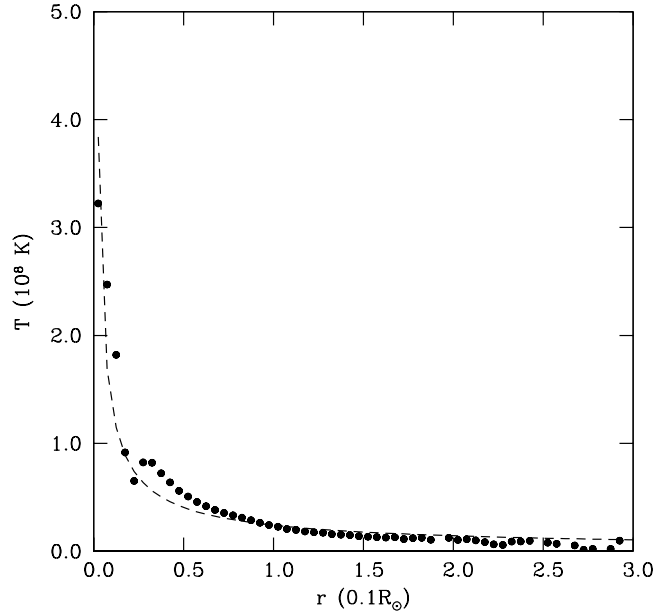


Figure 5.4: Surface temperature profile of the resulting disk (dots) compared to the theoretical relationship of Chiang & Goldreich (1997)

modest mass-loss rate — and form dust. Additionally, the central white dwarf has had time enough to accrete at a rate much smaller than the Bondi-Hoyle accretion rate

$$\dot{M}_{\text{BH}} = 10^{-15} \left( \frac{n}{\text{cm}^{-3}} \right) \left( \frac{v}{10 \text{ km/s}} \right)^{-3} \left( \frac{M_{\text{WD}}}{M_{\odot}} \right)^2 M_{\odot} \text{ yr}^{-1} \quad (5.2)$$

the very small amount of hydrogen from the ISM to show spectroscopic hydrogen features. We further assume that the accretion luminosity:

$$L_{\text{acc}} = \frac{GM_{\text{WD}}\dot{M}_{\text{acc}}}{R_{\text{WD}}} \quad (5.3)$$

is, in the worst of the cases, smaller than the luminosity of the white dwarf. This provides us with an (extreme) upper limit to the accretion rate from the disk, which turns out to be  $1.3 \times 10^{-13} M_{\odot} \text{ yr}^{-1}$ . Next, we assume that the abundance of Ca is the result of the equilibrium between the accreted material and gravitational diffusion:

$$\dot{M}_{\text{acc}} X_{\text{disk}} = \frac{M_{\text{env}} X}{\tau_{\text{diff}}} \quad (5.4)$$

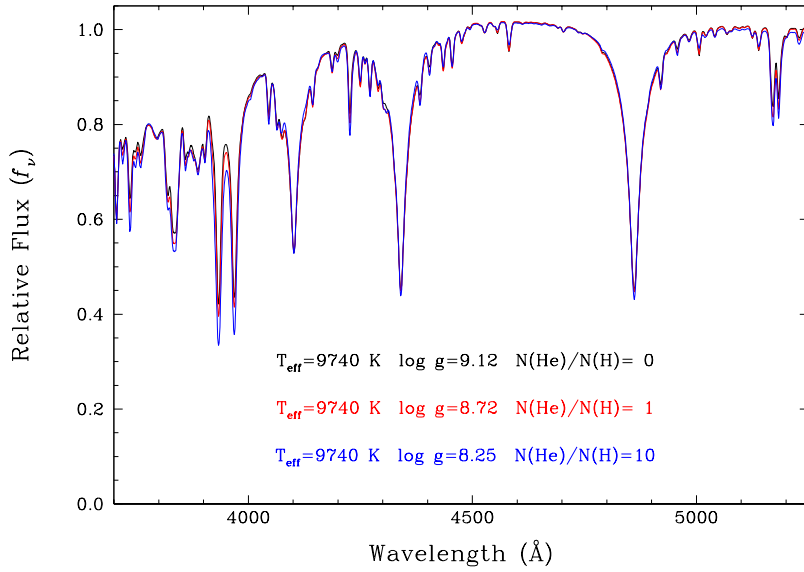


Figure 5.5: Spectrum of GD 362 for three different helium abundances. The black line shows the spectrum of GD 362 when a pure hydrogen atmosphere is assumed, leading to a surface gravity of  $\log g = 9.12$ . For increasing amounts of He — namely  $N(\text{He})/N(\text{H})=1$ , red curve, and  $N(\text{He})/N(\text{H})=10$ , blue curve — the corresponding surface gravities are smaller.

where  $M_{\text{env}}$  is the mass of the envelope of GD 362,  $X$  is the mass abundance in the envelope of the white dwarf of the considered element (either Ca, Mg or Fe),  $\tau_{\text{diff}}$  is the diffusion timescale,  $\dot{M}_{\text{acc}}$  is the required accretion rate and  $X_{\text{disk}}$  is the mass abundance in the disk.

The diffusion timescale of Ca for H-rich atmospheres is of the order of a few years. However, the accreted material is He-rich, so the diffusion timescale is probably more typical of a He-rich envelope, which is much larger (Paquette et al. 1986), of the order of  $\tau_{\text{diff}} \sim 1.5 \times 10^4$  yr. Unfortunately, diffusion timescales for mixed H/He envelopes do not exist. However, the diffusion characteristic times scale as  $\tau_{\text{diff}} \propto \rho T^{-1/2} g^{-2}$  (Alcock & Illarionov 1980). We have computed detailed atmosphere models for pure H, He/H=1 and He/H=10 and scaled the diffusion timescale using the values of the density and the temperature at the base of the convective zones and the appropriate chemical composition. For our fiducial composition (He/H=10) we obtain  $\tau_{\text{diff}} \sim 8.5 \times 10^3$  yr. From this we obtain the mass of the envelope which turns out to be  $M_{\text{env}} \sim 7.2 \times 10^{-9} M_{\odot}$ , which is much smaller than that obtained by accretion from the interstellar medium at the Bondi-Hoyle accretion rate — of the order of  $\sim 1.5 \times 10^{-6} M_{\odot}$ , adopting the typical values for the the velocity of a disk white

dwarf ( $v = 10$  km/s) and for the density of the interstellar medium ( $n = 0.7$  cm $^{-3}$ ) — and larger than that required to prevent convective mixing to occur at the effective temperature of GD 362 ( $\simeq 1.0 \times 10^{-10} M_{\odot}$ ), in which case GD 362 would not appear as a DAZ white dwarf, but as a He-rich DZ star instead. Hence, the photospheric abundances of GD 362 can be successfully explained by direct accretion from the surrounding disk.

### 5.3.2 The infrared excess

Now we assess whether the flux from the accretion disc can be fitted by the results of our SPH simulations. In order to compute the flux radiated away from the system two contributions must be taken into account. The first one is the expected photospheric flux from the star, for which we use the spectral energy distribution ( $B_{\text{WD}}$ ) of a white dwarf of mass  $1 M_{\odot}$ , at  $T_{\text{eff}} = 9740$  K:

$$F_{\text{WD}} = \pi \left( \frac{R_{\text{WD}}}{D_{\text{WD}}} \right)^2 B_{\text{WD}}(T_{\text{eff}}), \quad (5.5)$$

where  $D_{\text{WD}}$  is the distance to the white dwarf and  $R_{\text{WD}}$  is the radius of the white dwarf. Given the luminosity of our model and the apparent magnitude of GD 362 we obtain a distance of  $D_{\text{WD}} = 33$  pc. Becklin et al. (2005) used 22 pc but it should be taken into account that they adopted a mass for the central white dwarf of  $1.2 M_{\odot}$ , with a much smaller radius. Additionally Becklin et al. (2005) used  $R_{\text{WD}} \sim 5.0 \times 10^{-3} R_{\odot}$  in order to fit the flux in the  $J$ -band. This value is excessively large for such a massive white dwarf. A typical value for a  $\sim 1.2 M_{\odot}$  white dwarf is  $R_{\text{WD}} \simeq 2.0 \times 10^{-4} R_{\odot}$  (Althaus et al. 2005a), which is considerably smaller than the value adopted by these authors.

The second component of the spectral energy distribution is the emission of the disk which for a passive flat, opaque dust disk is given (Jura 2003):

$$F_{\text{disk}} \simeq 12\pi^{1/3} \cos i \left( \frac{R_{\text{WD}}}{D_{\text{WD}}} \right)^2 \left( \frac{2k_{\text{B}}T_{\text{s}}}{3h\nu} \right)^{8/3} \left( \frac{h\nu^3}{c^2} \right) \int_{x_{\text{in}}}^{x_{\text{out}}} \frac{x^{5/3}}{e^x - 1} dx \quad (5.6)$$

where  $i$  is the inclination of the disk (which we adopt to be face-on),  $x_{\text{in}} = h\nu/k_{\text{B}}T_{\text{in}}$  and  $T_{\text{in}} = 1200$  K is the condensation temperature of silicate dust. The outer radius is taken from the results of our SPH simulations and turns out to be  $R_{\text{out}} \simeq 1 R_{\odot}$ . The dots are the observational data for GD 362. The result is displayed in Fig. 5.5. As can be seen the agreement with the observational data is excellent.

The proposed scenario has two apparently weak points. The first one is that infrared observations indicate the presence of SiO. This requires that O should be more abundant than C in order to form it. However our simulations show that the ratio of C to O is a function of the distance to the primary and, in some regions of

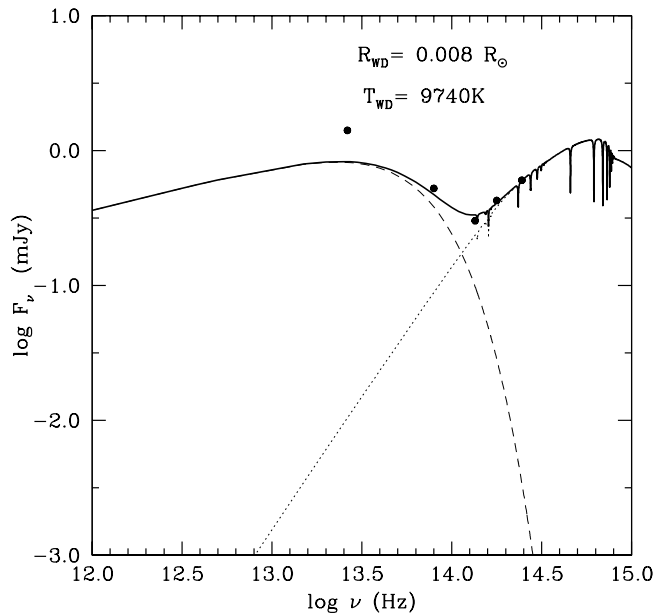


Figure 5.6: Spectral energy distribution for the circumstellar dust around GD 362. The dashed line represents the emission from the newly formed white dwarf, the dotted line is the emission from the disk and the solid line shows the sum of both spectral distributions.

the disk the ratio is smaller than 1, allowing for the formation of SiO in the accretion disk. Furthermore, after 2.2 Gyr of evolution the resulting disk has had time to form planets or asteroids with the subsequent chemical differentiation (see next section).

The second weakness of the model is that the central white dwarf rotates indeed very fast. However, a simple model of magnetic braking, coupling the magnetosphere of the white dwarf with the disk (see §5.3.4) shows that even very weak magnetic fields (of the order of 100 kG) are sufficient to brake down the central star to acceptable velocities.

### 5.3.3 Accretion from planets or asteroids

The mass available for forming planets is the mass contained between  $x_{\text{in}}$  (at  $\sim 0.057 R_{\odot}$ ) and the outer boundary of the disk, which turns out to be  $M \simeq 0.086 M_{\odot}$ . Hence we have enough material to form planets or asteroids ( $\sim 4 \times 10^4$  earth-like planets), which ultimately could be accreted by GD 362. Moreover, the probability of hosting a planet has been found to significantly increase with metallicity, as it is the case for the disks described here. Thus, planet formation in our scenario should also be highly efficient allowing to explain the very high metal abundances of

GD 362 by accretion of planets as initially suggested by Jura (2003). Moreover, after 2.2 Gyr, the disk has cooled enough to allow for the formation of solid bodies leading to an additional chemical differentiation. Since the radiation pressure is rather low, dust grains can be accreted by Poynting-Robertson drag. The timescale is given by (Hansen et al. 2006):

$$\begin{aligned}\tau_{\text{PR}} &= \frac{4\pi}{3} s \rho_s \frac{c^2 a^2}{L_{\text{WD}}} \\ &\approx \left( \frac{\rho_s}{3 \text{ g cm}^{-3}} \right) \left( \frac{s}{10 \mu\text{m}} \right) \left( \frac{R_{\text{out}}}{10^{11} \text{ cm}} \right)^2 \left( \frac{L_{\text{WD}}}{10^{-2} L_{\odot}} \right)^{-1} \text{ yr}\end{aligned}\quad (5.7)$$

where  $s$  and  $\rho_s$  are respectively the average size and density of dust grains. Adopting the values and the parameters that characterize GD 362, we obtain  $\tau_{\text{PR}} \sim 1900$  yr, which is much shorter than the diffusion timescale for the case of a He-rich envelope ( $\tau_{\text{diff}} \sim 15000$  yr). Note as well that since  $\tau_{\text{PR}} \propto R_{\text{out}}^2$  if the asteroids were placed farther away from the star, the timescale would rapidly increase. The mass of the dust necessary to sustain the accretion rate demanded by the observations is then:

$$M_{\text{dust}} = M_{\text{env}} \frac{\tau_{\text{PR}}}{\tau_{\text{diff}}} \frac{X}{X_{\text{dust}}}\quad (5.8)$$

If we assume that the abundance of Ca in the grains is in the range  $0.1 \leq X \leq 1$ , the mass of the disk must be between  $2 \times 10^{18}$  and  $2 \times 10^{19}$  g, which is reasonable. The characteristic timescale for collision between asteroids is (Dominik & Decin 2003):

$$\tau_{\text{col}} \approx 40 \left( \frac{R_{\text{out}}}{10^{11} \text{ cm}} \right)^{3.5} \left( \frac{R}{1 \text{ km}} \right) \left( \frac{M_{\text{disk}}}{10^{22} \text{ g}} \right)^{-1} \text{ yr}\quad (5.9)$$

where  $R$  is the radius of the asteroid and the rest of the symbols have been previously defined. In the case of GD 362, this gives between  $\tau_{\text{col}} \sim 2 \times 10^5$  yr and  $2 \times 10^4$  yr which, given the crude figures used here, indicates that collisions are frequent enough to sustain either a continuous or an intermittent production of dust. Additionally, some of the excess of angular momentum of the disk could be stored in this case in the form of planets (Livio et al. 2005).

### 5.3.4 Magnetic braking

One of the apparent drawbacks of the proposed scenario is that the central white dwarf spins rapidly. Using the observed spectrum of GD 362 it is possible to set an upper limit to the rotation speed which turns out to be  $v \sin i \leq 500 \text{ km s}^{-1}$ , see figure 5.7.

We assume that central white dwarf has a weak magnetic field,  $B$ . The magnetic torques that lead to spin-down are caused by the interaction between the white dwarf

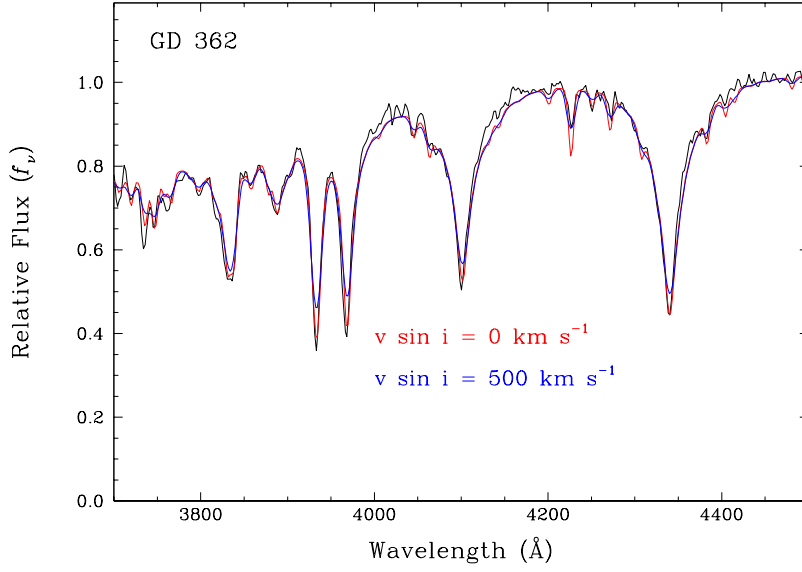


Figure 5.7: Spectrum of GD 362 for two different rotational velocities.

and the surrounding disc. The evolution of the angular velocity due to the coupling of the white dwarf magnetosphere and the disk is given by (Armitage & Clarke 1996; Livio & Pringle 1992; Benacquista et al. 2003):

$$\dot{\Omega} = -\frac{2\mu^2\Omega^3}{3Ic^3} \sin^2 \phi + \frac{\mu^2}{3I} \left( \frac{1}{R_m^3} - \frac{2}{(R_c R_m)^{3/2}} \right) + \frac{\dot{M} R_m^2 \Omega}{I} \quad (5.10)$$

where  $\mu = BR_{\text{WD}}^3$ ,  $R_{\text{WD}}$  is the radius of the white dwarf,  $R_m$  is the magnetospheric radius of the star,  $I$  is the moment of inertia,  $\phi$  is the angle between the rotation and magnetic axes (which we adopt to be  $30^\circ$ ) and

$$R_c = \left( \frac{GM_{\text{WD}}}{\Omega^2} \right)^{1/3} \quad (5.11)$$

is the corotation radius. In Eq. (5.10) the first term corresponds to the magnetic dipole radiation emission, the second one to the field–disk coupling, and the third one to the angular momentum transferred between disk and the central star. After some algebra Eq. (5.10) can be written as:

$$\dot{\Omega} = \alpha\Omega^3 + \beta\Omega + \gamma \quad (5.12)$$

where

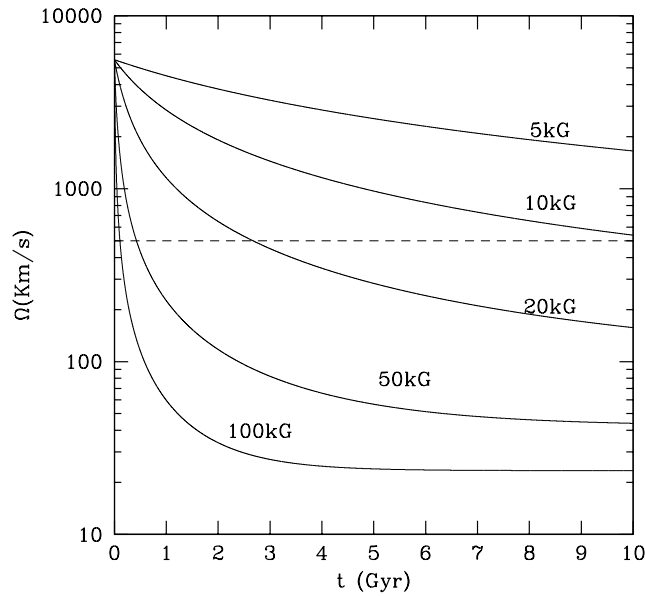


Figure 5.8: Evolution of the rotational velocity for several field strengths, the observational upper limit is shown as a horizontal dashed line.

$$\alpha \equiv -\left(\frac{2R_m^6 \sin^2 \phi}{3I_c^3}\right)B^2 \quad (5.13)$$

$$\beta \equiv \frac{\dot{M}R_m^2}{I} - \frac{2R_{WD}^6 B^2}{3IR_m^{3/2} \sqrt{GM_{WD}}} \quad (5.14)$$

$$\gamma \equiv \frac{R_{WD}^6 B^2}{3IR_m^3} \quad (5.15)$$

As can be seen, in the low velocity regime, the  $\Omega^3$  term in Eq. (5.10) can be neglected and so the field–disk coupling dominates the evolution of the system. Hence, although Eq. (5.10) can be solved numerically it is interesting to explore the linear regime. In this case we solve the simplified equation

$$\dot{\Omega} \simeq \beta\Omega + \gamma \quad (5.16)$$

for which the following solution holds:

$$\Omega(t) = -\frac{\gamma}{\beta} + \left(\Omega_0 + \frac{\gamma}{\beta}\right)e^{\beta t} \quad (5.17)$$

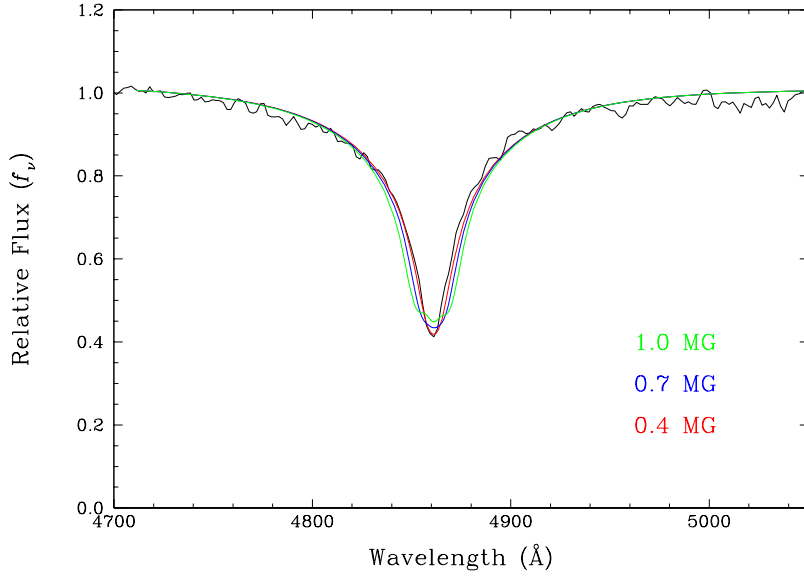


Figure 5.9: Spectrum of GD 362 for different magnetic field strengths.

where  $\Omega_0$  is the initial velocity. We want the star to spin down, so its derivative must be negative

$$\dot{\Omega}(t) = (\beta\Omega_0 + \gamma)e^{\beta t} < 0 \quad (5.18)$$

and, consequently:

$$\beta + \frac{\gamma}{\Omega_0} < 0 \quad (5.19)$$

which, after some manipulation, leads to:

$$\frac{R_m}{R_c} > 2^{-2/3} \approx 0.63 \quad (5.20)$$

Consequently, we adopt  $R_m = R_c$ , which ensures that the magnetic linkage between the star and the disk leads to a spin-down torque on the star, because the magnetospheric radius is large enough relative to the corotation radius.

Solving numerically the differential equation of Eq. (5.10), with the appropriate parameters for our case, the evolution of the rotation velocity is shown in figure 5.8. As can be seen, a weak magnetic field of about 50 kG is able to slow down the white dwarf to velocities below the observational limit. In order to see if this magnetic field is compatible with the spectrum of GD 362 in figure 5.9 we compare its spectrum

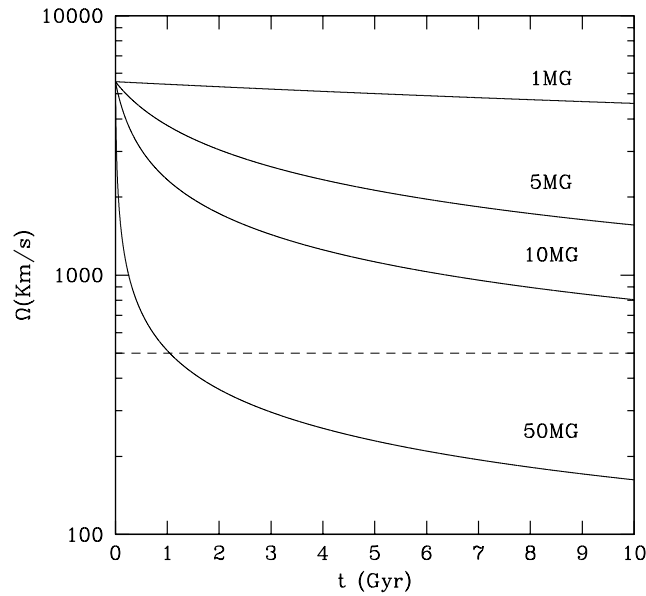


Figure 5.10: Evolution of the rotational velocity for several field strengths when only the dipole emission is taken into account. Again, the observational upper limit is shown as a horizontal dashed line.

with several theoretical spectra for different strengths of the magnetic field. The observations provide an upper limit of about 0.7 MG, much larger than the value needed to slow down the white dwarf to reasonable velocities. We emphasize that the responsible for the braking of the central star is the magnetic coupling between the white dwarf and the surrounding disk. In order to make this clear in figure 5.10 we show the evolution of the rotational velocity when only the dipole emission is included and the coupling between the white dwarf and the disk is ignored. As can be seen, the field strengths are in this case much larger and can be safely ruled out using the spectroscopic data for GD 362.

## 5.4 Discussion and conclusions

We have shown that the anomalous photospheric chemical composition of the DAZ white dwarf GD 362 and of the infrared excess of surrounding disk can be quite naturally explained assuming that this white dwarf is the result of the coalescence of a binary white dwarf system. This scenario provides a natural explanation of both the observed photospheric abundances of GD 362 and of its infrared excess without the need to invoke extreme assumptions, like the accretion of a planet or an asteroid,

---

since direct accretion from the disk surrounding disk provides a self-consistent way of polluting the envelope of the white dwarf with the required amounts of Ca, Mg, Si and Fe. Moreover, this last scenario can be also well accomodated within the framework of our scenario given that the formation of planets and other minor bodies is strongly enhanced in metal rich disks. Hence, GD 362 could be the relic of a very rare event in our Galaxy: the coalescence of a double white dwarf binary system.



## Chapter 6

# Conclusions

The goals of the present thesis were three. Firstly, we were interested in computing the gravitational wave emission of white dwarfs, either if they were members of a binary system or if they were single, field white dwarfs. Secondly, we were also concerned in studying the mergers of white dwarfs with the highest possible resolution and exploring the widest possible range of physical parameters of the double white dwarf binary systems. Finally, we also wanted to improve the computational performance of the previously existing SPH code. This, of course, should include the parallelization of the code which, on the one hand, should allow for an efficient use of the computational resources and, on the other, to make possible the calculation of large sets of initial conditions including, as already mentioned, the largest possible range of physical parameters of the intervening white dwarfs.

With respect to the first issue, the gravitational wave emission of pulsating white dwarfs has been studied for those white dwarfs for which we have good determinations of the physical and astronomical parameters, such as mass, distance, periods of the quadrupole modes, . . . and for a standard  $0.6 M_{\odot}$  white dwarf. These stars are BPM 37093 and PG 1159–035. We have computed the gravitational wave emission of the three kinds of pulsational modes,  $g$ ,  $f$ , and  $p$  for our three model stars and we have shown that none of these white dwarfs will be a good candidate for the LISA mission. In the case of the  $g$ -modes we have found that the signal is too weak to produce a direct detection by the LISA detector. In addition, we have taken into consideration the possibility of an indirect detection by measuring the secular rate of change of the period of the observed modes. Unfortunately we have shown that the rate of change is too small and lies far beyond the current observational possibilities. Despite this, these observationally confirmed pulsational modes are expected to contribute significantly to the gravitational wave background noise and must be taken into account. On the contrary, we have found that for the  $f$ - and  $p$ -modes the signal is high enough to be detected, but the very large luminosities emitted in form of gravitational waves will lead to very short-lived pulsational modes which

will hamper their detection independently of the considered star.

In second place, the emission of gravitational waves from merging white dwarf binaries has been computed for a wide range of masses and compositions of the components of the binary system. For that purpose we have used a SPH code which allowed us to follow the temporal evolution of the coalescing white dwarfs. We have shown that the most noticeable feature of the emitted signal is a sudden disappearance of the gravitational strains. We have additionally shown that the final stages of the chirping phase will be clearly detectable by LISA with a signal to noise ratio larger than 10 in all cases. Unfortunately, and despite the great insight that this kind of observations could give us into the physics of merging and progenitor systems, the actual number of systems that we expect LISA to be able to detect is rather small.

With respect to the second main topic of the thesis, we have performed several high-resolution Smoothed Particle Hydrodynamics simulations of coalescing white dwarfs. We have done so for a broad range of masses and chemical compositions of the coalescing white dwarfs, which includes He, CO and ONe white dwarfs. Several improvements with respect to previous studies have been done. Among these improvements we would like to mention a noticeable increase in the particle resolution, a full coverage of the possible initial masses of the coalescing white dwarfs and a refined treatment of the artificial viscosity. In all the cases, the merged configuration consists of a compact central object surrounded by a hot corona with spheroidal shape and a self-gravitating keplerian disk around it, which can be considered as a thin disk for all the cases except for the  $0.6 + 0.6 M_{\odot}$  case. We have found that nuclear reactions take place only when He is present in one of the stars, typically the secondary, being the only exception the  $0.6 + 1.2 M_{\odot}$  case, where high enough temperatures for the ignition of C have been reached. However, none of the cases studied here shows an explosive behavior during the merging phase. The chemical composition of the disks where relevant nuclear reactions have taken place has been analyzed showing an enrichment in heavy elements like Ca, Mg, S, Si and Fe.

In order to check the code consistency we have also compared the results of our hydrodynamical calculations with the angular momentum and mass transfer theoretical expectations finding a satisfactory agreement in the rate of change of the orbital distance and the corresponding spins of both the donor and the accretor star. We have computed as well the possible X-ray emission produced in the aftermath of the merger due to the interaction of disk material with high eccentricities with the innermost part of the disk where the particles have circularized orbits. This X-ray emission could eventually be used as an observational indication of the merger allowing for a more accurate detection of the gravitational wave signal. We have found that the X-ray luminosities are of the order of  $\sim 10^{49}$  erg/s with a time dependence  $\propto t^{5/3}$ . We have finally tried to elucidate the long-term evolution of the merger remnant. We have found that all the disks product of the coalescence of two white dwarfs are potentially turbulent. This most likely implies a very large accretion rate

---

from the disk onto the primary. If this were the case, an off-center carbon ignition, leading to the formation of a neutron star, seems to be the unavoidable outcome, although an in depth study remains to be done due to the crudeness of the approximations involved in the calculation of the accretion rates. Nevertheless, due to the very strong similarities between our results and those found by other authors (Yoon et al. 2007) it might be possible that at least some of our merged configurations may be considered good candidates for the progenitors of Type Ia supernovae. There are also some recent works (Ji et al. 2006) that suggest that even in cases where the classical indicators might suggest the presence of turbulence, its development does not take place, leading to steady and, consequently, much smaller accretion rates, compatible with those needed to produce a Type Ia supernova. Thus, a detailed calculation of the evolution of the resulting disks, including an accurate description of the mechanisms of angular momentum transport, must be done. Unfortunately this task is far beyond the current possibilities of SPH techniques and, hence, the problem remains still unsolved. In addition, we have shown that some of the observational properties of the DAZ white dwarf GD 362 might be explained assuming that the white dwarf is the result of the coalescence of a binary white dwarf system. The metal-rich disk generated after the merger constitutes a natural environment for the formation of planets and asteroids, which can account for the anomalous photospheric abundances of GD 362, while the resulting disk has proven to be able to account for the observed infrared excess.

Finally, with respect to the third main topic of the present thesis, several improvements have been incorporated into the code, being the most significant ones the new Riemann-based prescription for the artificial viscosity or the code parallelization which is discussed in appendix D. Additionally, as discussed in appendix B, a cluster of computers has been built in order to be able to comfortably run the code in parallel. As a result, we have been able to perform reliable high-resolution simulations in a relatively short periods of time.

There are however, some points that deserve more efforts, which must be undertaken in future works. We have already mentioned that a detailed calculation of the angular momentum transport in the resulting disks must be done. Due to the fact that SPH is not a suitable numerical technique for this purpose, other alternatives must be explored. Additionally, we have mentioned as well that the merger remnant of our simulations is a valid scenario for the formation of planets which can account for the anomalous atmospheric abundances of the DAZ white dwarf GD 362 and other white dwarfs with similar characteristics. This validity of this hypothesis still needs to be definitely proven, since other possibilities are still envisaged. Among these possibilities the most favored one is accretion from a tidally disrupted asteroid. Some simulations can be performed in this direction in order to prove that tidally crushed asteroids are able to reproduce the observed abundances. Additionally, there is work to do in code parallelization, which can still be refined, using perhaps the locally essential tree scheme or incorporating new technologies to our

cluster of computers, like GRAPE technology for the gravitational force calculation and neighbor search. Work in this direction is in progress.

# Appendix A

## Gravitational waves

In this appendix we introduce the basics of the theory of gravitational waves and their sources. The reader is assumed to be familiar with the basic concepts of the Theory of General Relativity. This appendix is organized as follows. In section A.1 we review the most basic aspects of general relativity. It follows section A.2 where the theory of linearized of general relativity is described, whereas in section A.3 we discuss the propagation and the most basic features of gravitational waves. Finally, section A.4 is devoted to briefly summarize how gravitational waves are produced.

### A.1 General relativity

The theoretical basis of gravitational waves relies on General Relativity (Einstein 1916). General Relativity is a relativistic theory of gravity, constructed by Einstein in order to reconcile Newton's theory of gravity with special relativity. Special relativity asserts that we live in a four-dimensional manifold, described entirely by Minkowski's metric tensor  $\eta_{\mu\nu}$ . From this tensor, one can calculate the distance or the interval,  $ds$ , between any two points of space-time

$$ds^2 = \eta_{\mu\nu} dx^\mu dx^\nu = (cdt)^2 - d\vec{x}^2 \quad \mu, \nu = 0, \dots, 3 \quad (\text{A.1})$$

where  $d\vec{x}^2$  is the usual euclidean distance. Therefore,  $\eta_{\mu\nu}$  is a  $4 \times 4$  diagonal matrix with components  $1, -1, -1, -1$ . General relativity goes still further and asserts that we live in a four-dimensional manifold, described by a general symmetrical  $4 \times 4$  metric tensor  $g_{\mu\nu}$ . Again, the four-dimensional distance can be computed as

$$ds^2 = g_{\mu\nu} dx^\mu dx^\nu \quad \mu, \nu = 0, \dots, 3 \quad (\text{A.2})$$

Conceptually speaking, general relativity is very simple. The gravitational field is represented as the departure of the space-time metric from Minkowski's one. In other words, in absence of a gravitational field, the space-time metric is equal to

$\eta_{\mu\nu}$  and bodies follow the trajectories predicted by the laws of special relativity. If a gravitational field is present, the space-time metric becomes the more general  $g_{\mu\nu}$  and bodies freely follow the geodesics of this general space-time. Within this context gravity is not a force, it is only the manifestation of the space-time geometry over the trajectories of bodies. Likewise newtonian theory, in general relativity the gravitational field in a certain space-time region is determined by its matter content, which in any sensible relativistic theory must be represented by the energy-momentum tensor. Thus, in order to determine the space-time metric in any region, a set of equations must be constructed which relates the gravitational field — represented by  $g_{\mu\nu}$  — with its matter content — which will be represented by the energy-momentum tensor  $T_{\mu\nu}$ . These are Einstein's equations:

$$R_{\mu\nu} = -8\pi G \left( T_{\mu\nu} - \frac{1}{2} g_{\mu\nu} T \right) \quad (\text{A.3})$$

which must be complemented with the four-dimensional equation of motion (geodesic) that a body must follow under the influence of a gravitational field:

$$\frac{dx^\lambda}{d\tau^2} + \Gamma_{\mu\nu}^\lambda \frac{dx^\mu}{d\tau} \frac{dx^\nu}{d\tau} = 0. \quad (\text{A.4})$$

Eq. (A.3) determines the geometry of a region of space-time as a function of its matter content. Once we solve it, an expression for the metric tensor is obtained which, in turn, allows to solve Eq. (A.4). However, it must be kept in mind that both  $R_{\mu\nu}$  and  $\Gamma_{\mu\nu}^\lambda$  are functions of  $g_{\mu\nu}$ :

$$\Gamma_{\mu\nu}^\lambda = \frac{1}{2} g^{\lambda\kappa} [\partial_\mu g_{\kappa\nu} + \partial_\nu g_{\kappa\mu} - \partial_\kappa g_{\mu\nu}] \quad (\text{A.5})$$

$$R_{\lambda\mu\nu\kappa} = \frac{1}{2} [\partial_\kappa \partial_\mu g_{\lambda\nu} - \partial_\kappa \partial_\lambda g_{\mu\nu} - \partial_\nu \partial_\mu g_{\lambda\kappa} + \partial_\nu \partial_\lambda g_{\mu\kappa}] \quad (\text{A.6})$$

$$R_{\mu\nu} = R_{\mu\lambda\nu}^\lambda \quad (\text{A.7})$$

Eqs. (A.3) are highly non-linear, which makes very difficult finding exact solutions to them. As it will be shown later, all the astrophysical processes we have studied are well described in terms of weak gravitational fields, and in this regime, the non-linear effects can be neglected. Hence, from now on we concentrate in the study the linear regime only.

## A.2 Linearized general relativity

One of the most remarkable facts about general relativity is that a gravitational field carries away energy and momentum. Accordingly, a gravitational field is also a source of new gravitational fields. This is the reason why general relativity is a

non-linear theory. In order to find a linear approximation to general relativity, the energy and momentum carried away by the gravitational field must be neglected. This is only true for weak gravitational fields. Under these conditions the metric is, consequently, very close to the Minkowski metric  $\eta_{\mu\nu}$ , and we can safely write

$$g_{\mu\nu} = \eta_{\mu\nu} + h_{\mu\nu} \quad (\text{A.8})$$

where  $|h_{\mu\nu}| \ll 1$ . To first order in  $h$ , the Ricci tensor is then

$$R_{\mu\nu} \simeq \partial_\mu \Gamma_{\lambda\mu}^\lambda - \partial_\lambda \Gamma_{\mu\nu}^\lambda + \mathcal{O}(h^2) \quad (\text{A.9})$$

and the affine connection is

$$\Gamma_{\mu\nu}^\lambda = \frac{1}{2} \eta^{\lambda\rho} [\partial_\mu h_{\rho\nu} + \partial_\nu h_{\rho\mu} - \partial_\rho h_{\mu\nu}] + \mathcal{O}(h^2) \quad (\text{A.10})$$

Now, introducing Eqs. (A.9) and (A.10) into Eq. (A.3), after some algebra we obtain the following expression:

$$\square^2 h_{\mu\nu} - \partial_\lambda \partial_\mu h_\nu^\lambda - \partial_\lambda \partial_\nu h_\mu^\lambda + \partial_\mu \partial_\nu h_\lambda^\lambda = -16\pi G \bar{T}_{\mu\nu} \quad (\text{A.11})$$

$$\bar{T}_{\mu\nu} \equiv T_{\mu\nu} - \frac{1}{2} \eta_{\mu\nu} T_\lambda^\lambda \quad (\text{A.12})$$

Where  $T_{\mu\nu}$  is taken to the lowest order in  $h_{\mu\nu}$  — that is, it does not take into account the energy of the gravitational field — and, consequently, satisfies the ordinary special-relativistic conservation equations

$$\partial_\mu T_\nu^\mu = 0 \quad (\text{A.13})$$

Now, we have found a linear field equation, but it is not difficult to see that Eq. (A.11) cannot yield unique solutions. This is a general problem of the theory, similar to what occurs for Maxwell's equations. By construction, the Ricci tensor satisfies the so-called Bianchi identities

$$\nabla_\mu \left( R^{\mu\nu} - \frac{1}{2} g^{\mu\nu} R \right) = 0 \quad (\text{A.14})$$

Where the symbol  $\nabla$  stands for the covariant derivative — i.e., a coordinate-invariant derivative. Thus, despite the fact the Ricci tensor has 10 independent components, in Eq. (A.6) there are only 6 functionally independent equations. Thus, any solution of the field equations will have four degrees of freedom. In other words, if  $g_{\mu\nu}$  is a solution of the field equations, then we can generate new solutions by a general coordinate transformation. This is usually called gauge invariance. In order to solve the linear field equations a certain gauge must be fixed. The most convenient choice is to work in a harmonic coordinate system, for which

$$g^{\mu\nu}\Gamma_{\mu\nu}^{\lambda} = 0 \quad (\text{A.15})$$

Using Eq. (A.10), in the weak field limit this gives

$$\partial_{\mu}h_{\nu}^{\mu} - \frac{1}{2}\partial_{\nu}h_{\mu}^{\mu} = 0 \quad (\text{A.16})$$

Consequently, introducing Eq. (A.15) in Eq. (A.11), the final field equations for the linearized gravitational field are

$$\square^2 h_{\mu\nu} = -16\pi G\bar{T}_{\mu\nu} \quad (\text{A.17})$$

Or alternatively

$$\square^2 \bar{h}_{\mu\nu} = -16\pi GT_{\mu\nu} \quad (\text{A.18})$$

where

$$\bar{h}_{\mu\nu} \equiv h_{\mu\nu} - \frac{1}{2}\eta_{\mu\nu}h. \quad (\text{A.19})$$

It is easy to see that the complete set of linearized field equations in vacuum take the form

$$\square^2 \bar{h}_{\mu\nu} = 0 \quad (\text{A.20})$$

$$\partial_{\mu}\bar{h}_{\nu}^{\mu} = 0 \quad (\text{A.21})$$

Which is simply the conventional relativistic wave equation. This will determine the evolution of a disturbance of the gravitational field in vacuum in the harmonic gauge. These are usually called gravitational waves.

### A.3 Plane waves

If we want to study the propagation of gravitational waves in vacuum, a particularly useful set of solutions to this wave equation are plane waves, which are given by

$$h_{\mu\nu} = e_{\mu\nu} \exp(ik_{\sigma}x^{\sigma}) \quad (\text{A.22})$$

where  $e_{\mu\nu}$  and  $k_{\sigma}$  are constants. Substituting Eq. (A.22) into the set of equations (A.20) and (A.21) we obtain

$$k_{\sigma}k^{\sigma} = 0 \quad (\text{A.23})$$

and

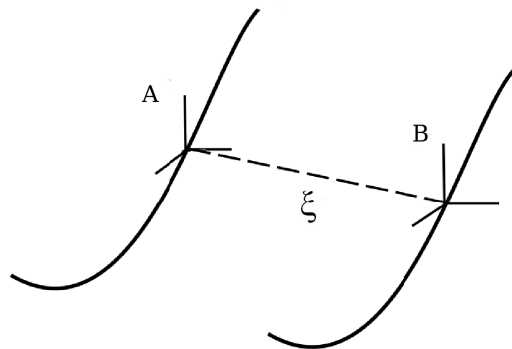


Figure A.1: Two neighbouring particles and its 3-space distance  $\xi$ .

$$k_\mu \mathbf{e}^{\mu\nu} = 0 \quad (\text{A.24})$$

That is,  $k$  is a null vector and it is orthogonal to  $e$ . Eq. (A.23) implies that gravitational waves travel at the speed of light, whereas Eq. (A.24) means that they are transversal waves. Note that the plane wave has 10 independent components, and that the gauge equation, Eq. (A.24), reduces the number of independent equations from 10 to 6. Despite the fact we have imposed the gauge condition there is still some coordinate freedom left. In particular, we still can, by coordinate transformations, generate new solutions to the field equations without leaving the harmonic gauge. By using this remaining freedom we can always demand that  $e_\mu^\mu = 0$  and  $e_{0\nu} = 0$ . Thus, in general, the independent components of a plane wave can be written as:

$$\mathbf{e}_{\mu\nu} = \begin{pmatrix} 0 & 0 & 0 & 0 \\ 0 & e_{xx} & e_{xy} & 0 \\ 0 & e_{xy} & -e_{xx} & 0 \\ 0 & 0 & 0 & 0 \end{pmatrix} \quad (\text{A.25})$$

With this choice of gauge, we have reached a subgauge of the harmonic gauge which is usually called the transverse-traceless gauge. It is easy to see that in this gauge  $h_{\mu\nu}^{\text{TT}} = \bar{h}_{\mu\nu}^{\text{TT}}$ .

Now that we know how a gravitational wave propagates in vacuum, we ask ourselves how this gravitational wave affects matter as it travels through. Imagine that we have two particles A and B at rest, as illustrated in figure A.1. And now imagine that an arbitrary gravitational wave crosses. How will they be affected? In order to answer this question we simply need what is called the geodesic deviation equation, which measures how the distance  $\xi$  between two particles evolves with time as they move along two neighbouring geodesics. The equation of geodesic deviation can be derived from Eq. (A.4) and is given by

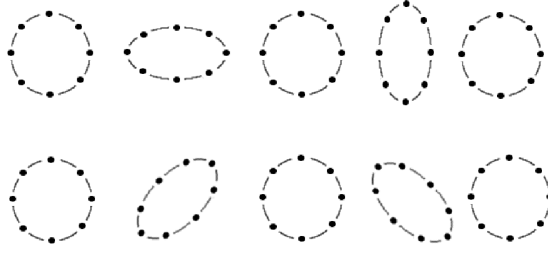


Figure A.2: A ring of test particles under the influence of a gravitational wave. The top panel corresponds to the effect of a “+” polarized gravitational wave, while the bottom panel corresponds to the effect of a “×” polarized gravitational wave.

$$\nabla_{\mu}\nabla_{\nu}\xi^{\rho}=R_{\mu\lambda\nu}^{\rho}v^{\mu}v^{\nu}\xi^{\lambda} \quad (\text{A.26})$$

which is a four-dimensional differential equation. In fact, we are only interested in its three-dimensional part, which reads

$$\frac{d^2\xi^i}{dt^2}=R_{0j0}^i\xi^j=\frac{1}{2}h^{\text{TT}i}_{j,00}\xi^j \quad (\text{A.27})$$

This equation will describe the oscillations of particle B as seen from an observer co-moving with particle A due to space-time distortion produced by the gravitational wave. In this approximation, valid for small curvature gradients, the gravitational wave is seen as a tidal force, perturbing the proper distance between the two particles. The way the particles will be distorted depends essentially on the polarization of the wave. From what we have said before it can be seen that there are only two independent polarization states a gravitational wave can have, the  $e_{xx}$  and the  $e_{xy}$  polarizations, also called the “+” and “×” polarizations. In Fig. A.2 the effect of the two polarizations can be seen.

#### A.4 The sources of gravitational waves

In order to compute the gravitational emission of a certain system the system of equations given by Eq. (A.17) must be solved. This can be done by using Green’s function

$$\bar{h}_{\mu\nu}(x^{\sigma})=-16\pi G\int_{R^4}G(x^{\sigma}-y^{\sigma})T_{\mu\nu}(y^{\sigma})dy^4 \quad (\text{A.28})$$

where  $x^{\sigma}$  is the point where the gravitational wave will be measured,  $y^{\sigma}$  belongs to the radiating space-time region and

$$G(x^\sigma - y^\sigma) = -\frac{1}{4\pi G |\vec{x} - \vec{y}|} \delta |\vec{x} - \vec{y}| \theta(x^0 - y^0) \quad (\text{A.29})$$

It can be easily seen that Eq. (A.29) simply selects the contribution of those radiating regions  $\vec{y}$  which are causally connected with point  $\vec{x}$ . If we restrict ourselves to slow-moving sources and, moreover, to sources whose size is small compared with the observational distance — which will always be the case in astrophysical situations — it can be proven after some algebra that the solution turns out to be:

$$h_{jk}^{\text{TT}}(t, \vec{x}) = \frac{2G}{c^4 d} \ddot{S}_{jk}^{\text{TT}} \left( t - \frac{d}{c} \right) \quad (\text{A.30})$$

where  $R = |\vec{y} - \vec{x}|$  and  $t - R/c$  is the so-called the retarded time — the time at which the gravitational perturbation that is now reaching the observer at  $\vec{x}$  was produced. Finally,  $S$  is given by

$$S_{jk} = \int T^{00} \left( t - \frac{d}{c}, \vec{y} \right) \left( y^j y^k - \frac{1}{3} \delta_{jk} d^2 \right) d^3 y \quad (\text{A.31})$$

Moreover, since

$$T^{00} \left( t - \frac{d}{c}, \vec{y} \right) \approx \rho \left( t - \frac{d}{c}, \vec{y} \right) \quad (\text{A.32})$$

the solution can also be written as

$$h_{jk}^{\text{TT}}(t, \vec{x}) = \frac{2G}{c^4 d} \ddot{Q}_{jk}^{\text{TT}} \left( t - \frac{d}{c} \right) \quad (\text{A.33})$$

where  $Q$  is nothing but the newtonian mass-quadrupole. This is the so called mass-quadrupole emission term and corresponds to the lowest order term in any gravitational radiation emission process. Higher order terms, like current-quadrupole or mass-octupole are usually completely negligible for the phenomena we pretend to study. Consequently, all our calculations will be performed using this approximation. Within the same approximation, the total luminosity radiated in form of gravitational waves is:

$$L = \frac{1}{5} \frac{G}{c^5} \left[ \ddot{\ddot{Q}}^{jk} \ddot{\ddot{Q}}_{jk} \right] \quad (\text{A.34})$$



# Appendix B

## The essence of SPH

### B.1 Introduction

The most commonly used technique to solve the equations of fluid dynamics consists of discretizing and linearizing these equations using finite differences. The main drawbacks of this approach are the errors introduced by the discretization of the equations and the loss of physical perspective. Additionally, finite difference techniques usually result in a heavy computational demand. Therefore, other numerical techniques are sometimes advisable. In the remaining of this chapter it will be shown how to solve numerically the equations of motion of a real fluid in the Lagrangian formulation using an alternative technique: Smoothed Particle Hydrodynamics. Since this is a well known technique we will only summarize here the most important and basic ingredients of this technique and we refer the reader to the recent and excellent review of Monaghan (2005) and to the older review of Benz (1990) for thorough descriptions of the rest of the details.

Smoothed Particle Hydrodynamics is an approximate method to solve the equations of fluid dynamics where the elements are replaced by particles of finite size. The method is gridless, and the forces on the fluid are calculated directly from the particle positions. The SPH method has several attractive features. The first of these is that pure advection is treated exactly. The second advantage is that with more than one material, each one of these materials can be described by a different set of particles and, consequently, interface problems are often very easy to handle using SPH techniques but quite difficult for methods in which finite difference schemes are involved. The third advantage is that particle methods are able to handle quite smoothly and naturally the transition the continuum and fragmentation. A fourth advantage is that the resolution can be made to depend on position and time. This property makes the method very appealing for most astrophysical applications. Fifth, SPH has the computational advantage, particularly in problems involving regions with large voids, that the computation is only done in those places where the

matter is. This, in turn, results in a considerable reduction of storage needs and an effective saving in computing resources. Finally, in SPH codes it is possible to include complex physics in a rather simple way. Perhaps the major drawback of SPH algorithms is that although typical codes give reasonable and sound results for shocks, they are not as accurate as the those codes in which Riemann-solvers and other modern techniques are used. Due to the poorer accuracy of SPH algorithms, in systems where very small perturbations are to be followed it is preferable to use finite difference methods.

The SPH method was originally introduced by Lucy (1977) and Gingold & Monaghan (1977) who applied it to the calculation of dynamical fission instabilities in rapidly rotating stars. Since then, the method has been used in many different types of astrophysical fluid dynamic problems. Planet and star formation, solar system formation, supernova explosions, tidal disruption of stars by massive black holes, large scale cosmological structure formation, galaxy formation, stellar collisions, binary coalescence and the propagation of a thermonuclear flame are some of them. The SPH method was originally designed to deal with astrophysical problems but has also been successfully used for several practical problems involving complex flows like gas dynamics, incompressible flows, elasticity and fracture, liquid metals, conduction problems and others. All these cases have systems sharing the common property that they sometimes present difficulties for finite difference and finite element methods. Particularly when coupled with complex free surface motion.

## B.2 Interpolation

In Smoothed Particle Hydrodynamics the fundamental properties of a fluid element are locally reconstructed by interpolating the properties of the neighboring particles, while the whole system follows the hydrodynamic equations. The SPH method is purely lagrangian and gridless and it works optimally in systems without definite boundaries. Consequently the key concept in SPH is interpolation. Precisely, this section deals with the way in which these properties are interpolated.

As clearly seen from Eqs. (2.1), in the Lagrangian form the equations of fluid dynamics adopt the form

$$\frac{dA}{dt} = f(A, \nabla A, r) \quad (\text{B.1})$$

where  $A$  can be either a scalar or a vector, and

$$\frac{d}{dt} = \frac{\partial}{\partial t} + \vec{v} \cdot \vec{\nabla} \quad (\text{B.2})$$

is the lagrangian derivative. Thus, in fluid dynamics the rates of change of physical quantities require the evaluation of derivatives. While in finite difference methods the derivatives are evaluated at the vertices of a mesh, in SPH the interpolating points are

particles moving with the flow and the interpolation is done using kernel estimation. The kernel is an interpolating function  $W(r - r', h)$ . The SPH interpolation of a quantity, which is a function of the spatial coordinates, is based on the integral interpolant

$$\langle A(r) \rangle = \int A(r') W(r - r', h) dr' \quad (\text{B.3})$$

that reproduces the quantity exactly if the kernel is a delta function. The constant  $h$  is a free parameter which, for obvious reasons, is called the smoothing length. The smoothing length is a measure of the typical size of the “particles”. The kernels are always normalized to unity. In practice they are functions that tend to the delta function as the length scale  $h$  tends to zero. For instance, in one dimension the gaussian kernel has the form

$$W(r, h) = \frac{1}{\pi h^3} \exp(-r^2/h^2) \quad (\text{B.4})$$

whereas the original kernel of Lucy (1977) has the form:

$$W(r, h) = \begin{cases} \frac{105}{16\pi h^3} \left(1 - \frac{r}{h}\right)^3 \left(1 + \frac{3r}{h}\right) & 0 \leq r \leq h \\ 0 & r > h \end{cases} \quad (\text{B.5})$$

The most commonly used kernels are based on spline interpolation (Monaghan, 1985). More specifically, the most widely adopted kernel is the so-called cubic spline (Monaghan & Lattanzio, 1985):

$$W(r, h) = \begin{cases} \frac{1}{4\pi} \left[ \left(2 - \frac{r}{h}\right)^3 - 4 \left(1 - \frac{r}{h}\right)^3 \right] & 0 \leq r \leq h \\ \frac{1}{4\pi} \left(2 - \frac{r}{h}\right)^3 & h \leq r \leq 2h \\ 0 & r > 2h \end{cases} \quad (\text{B.6})$$

which is positive definite. The reason for refraining to use higher order spline kernels is that they do not perform well in real situations, when the particles of the fluid are not equally distributed. The cubic spline kernel has a very valuable property: it is a continuous function with a continuous derivative. Thus, if the quantity to be interpolated is a constant or a linear function the interpolation is exact, otherwise it is an approximation of second order in space to the true value of the function. All kernels fall off rapidly with distance. However, as can be seen from Eqs. (B.4) and (B.6) their properties are rather different. For instance the gaussian kernel is never zero, which means that at a given point in space we have contributions from the rest of particles regardless of their distance. This is not the case of the cubic spline kernel, which is exactly zero for distances  $r \geq 2h$ . Hence, particles at distances larger than  $2h$  do not contribute to the average.

To interpolate the properties of the fluid at a given point we divide in several small mass elements, where element  $a$  will have a mass, a density and a position. The interpolating integral can be written as

$$\langle A(r) \rangle = \int \frac{A(r')}{\rho(r')} \rho(r') dr' = \int \frac{A(r')}{\rho(r')} dm' \quad (\text{B.7})$$

The integral is then substituted by a summation over all particles

$$\langle A(r) \rangle = \sum_b m_b \frac{A_b}{\rho_b} W(r - r_b, h) \quad (\text{B.8})$$

However, since the kernel falls off very rapidly, only the neighboring particles contribute. Typically the smoothing length is close to the particle separation. For instance, if we want to interpolate the density, we would have

$$\langle \rho(r) \rangle = \sum_b m_b W(r - r_b, h) \quad (\text{B.9})$$

If the smoothing length  $h$  is constant the density can be integrated

$$\int \langle \rho(r) \rangle dV = \sum_b m_b = M \quad (\text{B.10})$$

and mass will be conserved exactly. If  $h$  is allowed to vary, the integral no longer yields the total mass of the system, but the total mass is conserved because it is carried by the particles.

### B.3 SPH derivatives

When the smoothing kernel is a differentiable function, the derivatives in SPH can be very easily estimated:

$$\left\langle \frac{\partial A}{\partial x} \right\rangle = \sum_b m_b \frac{A_b}{\rho_b} \frac{\partial W}{\partial x} \quad (\text{B.11})$$

In SPH the derivative is therefore found by an exact derivative of an approximate function. Though, this form of the derivative does not vanish if  $A$  is constant, but there is an easy way solve this problem. Assume that  $\Phi$  is a differentiable function, so that

$$\frac{\partial A}{\partial x} = \frac{1}{\Phi} \left( \frac{\partial(\Phi A)}{\partial x} - A \frac{\partial \Phi}{\partial x} \right) \quad (\text{B.12})$$

the SPH form is then

$$\left\langle \frac{\partial A}{\partial x} \right\rangle = \frac{1}{\Phi_a} \sum_b m_b \frac{\Phi_b}{\rho_b} (A_b - A_a) \frac{\partial W_{ab}}{\partial x_a} \quad (\text{B.13})$$

where

$$W_{ab} = W(x_a - x_b, h) \quad (\text{B.14})$$

which vanishes if  $A$  is constant. Different choices of  $\Phi$  yield different formulations. For instance, the continuity equation

$$\frac{d\rho}{dt} + \rho \vec{\nabla} \cdot \vec{v} = 0 \quad (\text{B.15})$$

can be presented either as

$$\frac{d\rho_a}{dt} = \rho_a \sum_b \frac{m_b}{\rho_b} \vec{v}_{ab} \cdot \vec{\nabla}_a W_{ab} \quad (\text{B.16})$$

or

$$\frac{d\rho_a}{dt} = \sum_b m_b \vec{v}_{ab} \cdot \vec{\nabla}_a W_{ab} \quad (\text{B.17})$$

where  $\vec{v}_{ab} = \vec{v}_a - \vec{v}_b$ . Both expressions vanish when the velocity is constant. However, the former yields better results for problems in which two fluids with a large density contrast are involved, because it involves contributions of the density from both sides of the interface.

## B.4 Errors in the integral interpolant

It is not easy to estimate the errors in the SPH equations from first principles because the particles get disordered during motion. The errors depend on the type of disorder which, in turn, depends on the dynamics. SPH is much more accurate than the interpolation of quantities from randomly disordered particles would suggest. Starting with the integral interpolant in one dimension

$$\begin{aligned} \langle A(r) \rangle &= \int A(x') W(x - x', h) dx' \\ &= A(x) + \int (A(x') - A(x)) W(x - x', h) dx' \end{aligned} \quad (\text{B.18})$$

the error can be estimated by a Taylor series expansion of  $A(x)$ . By assuming that  $W(x - x', h)$  is an even function of  $q$ , the interpolant gives

$$\langle A(x) \rangle = A(x) + \frac{\sigma h^2}{2} \frac{d^2 A(x)}{dx^2} + \dots \quad (\text{B.19})$$

where  $\sigma$  is a constant depending on the kernel. As the third term vanishes due to symmetry, only the fourth term is left. However, all these results assume that the integrals can be extended to the entire volume within the support of the kernel. If this is not possible, close to the boundary for instance, the error is larger. Higher order smoothing kernels are not positive definite, which is an undesired property, since the density may become negative close to a strong shock.

## B.5 SPH Euler equations

The Euler equations are the equations for the rates of change of velocity, density and position, namely

$$\frac{d\vec{v}}{dt} = -\frac{1}{\rho} \vec{\nabla} P + g \quad (\text{B.20})$$

$$\frac{d\rho}{dt} = -\rho \vec{\nabla} \cdot \vec{v} \quad (\text{B.21})$$

$$\frac{d\vec{r}}{dt} = \vec{v} \quad (\text{B.22})$$

The equation for the rate of change of the density has been discussed earlier, so we start with the equation for the acceleration:

$$\frac{d\vec{v}_a}{dt} = -\frac{1}{\rho_a} \sum_b m_b \frac{P_b}{\rho_b} \vec{\nabla}_a W_{ab} \quad (\text{B.23})$$

However, it can be easily seen that this equation does not conserve linear and angular momentum, since

$$\frac{m_a m_b P_a}{\rho_a \rho_b} W_{ab} \neq \frac{m_a m_b P_b}{\rho_a \rho_b} W_{ab} \quad (\text{B.24})$$

Thus, the force on particle  $a$  due to  $b$  is not equal and opposite to that on  $a$  due to  $b$ . However, we can take advantage of the fact that

$$\frac{\vec{\nabla} P}{\rho} = \vec{\nabla} \left( \frac{P}{\rho} \right) + \frac{P}{\rho^2} \vec{\nabla} \rho \quad (\text{B.25})$$

which gives

$$\frac{d\vec{v}_a}{dt} = -\sum_b m_b \left( \frac{P_b}{\rho_b^2} + \frac{P_a}{\rho_a^2} \right) \vec{\nabla}_a W_{ab} \quad (\text{B.26})$$

that has the correct behavior. Thus, linear and angular momentum are conserved exactly, even if the smoothing length is allowed to vary. Finally, the SPH formulation of Eq. (2.22) is rather obvious:

$$\frac{d\vec{r}_a}{dt} = \vec{v}_a \quad (\text{B.27})$$

To this set of equations most SPH codes add another equation, namely, the equation of energy conservation. Strictly speaking the Euler equations do not require the time rate of change of thermal energy to be calculated. However it is advisable to keep track of energy. We start with the First Law of Thermodynamics

$$Tds = du + PdV = du - \frac{P}{\rho^2}d\rho \quad (\text{B.28})$$

where all the symbols have their usual meaning. Thus, we have:

$$\frac{du}{dt} = \frac{P}{\rho^2} \frac{d\rho}{dt} = -\frac{P}{\rho^2} \vec{\nabla} \cdot \vec{v} \quad (\text{B.29})$$

in the absence of transport. Then, it is possible to use the previous procedure to obtain for each particle the following expression

$$\frac{du_a}{dt} = \frac{P_a}{\rho_a^2} \sum_b m_b \vec{v}_{ab} \cdot \vec{\nabla}_a W_{ab} \quad (\text{B.30})$$

However, it turns out that the expression

$$\frac{du_a}{dt} = \frac{P_a}{\rho_a} \sum_b \frac{m_b}{\rho_b} \vec{v}_{ab} \cdot \vec{\nabla}_a W_{ab} \quad (\text{B.31})$$

yields better results. It is also useful to add the kinetic energy

$$e = \frac{1}{2}v^2 + u \quad (\text{B.32})$$

to obtain the equation of conservation of energy

$$\frac{de}{dt} = -\frac{1}{\rho^2} \vec{\nabla} \cdot (P\vec{v}) \quad (\text{B.33})$$

Once again following the former procedure gives

$$\frac{de_a}{dt} = -\sum_b m_b \left( \frac{P_a \vec{v}_b}{\rho_a^2} + \frac{P_b \vec{v}_a}{\rho_b^2} \right) \cdot \vec{\nabla}_a W_{ab} \quad (\text{B.34})$$

Calculations of shock phenomena with finite difference methods often use the thermokinetic energy equation rather than the thermal energy equation, because it ensures conservation of the energy. In SPH codes this is done as well.

## B.6 Resolution varying in space and time

In the original formulation of SPH the smoothing length was kept constant. In fact, in the original calculations of Gingold & Monaghan (1977), each particle had the same  $h$

$$h \propto \sqrt{\langle r^2 \rangle - \langle r \rangle^2} \quad (\text{B.35})$$

where  $\langle r^2 \rangle$  was computed according to the expression

$$\langle r^2 \rangle = \frac{\sum_b m_b r_b^2}{\sum_b m_b} \quad (\text{B.36})$$

During a simulation,  $h$  is then increased when the particle system expands and decreases when it contracts. Nowadays, a variable smoothing length as a function of density is used. Gingold & Monaghan (1983) considered it preferable to allow the smoothing length to change according to

$$h_a = \sigma \left( \frac{m_a}{\rho_a} \right)^{1/d} \quad (\text{B.37})$$

where  $d$  is the number of dimensions and  $\sigma \approx 1.3$  is a constant. In this way the smoothing length, and thus the resolution, varies both in space and time. If the density is determined by summation, the density for a given particle can be written as

$$\rho_a = \sum_b m_b W_{ab}(h_a) \quad (\text{B.38})$$

The usual approach in the literature is either to calculate the smoothing length at any time using the current value of the density (estimated from the SPH summation), or to calculate it from the density according to the expression

$$\frac{d \ln h}{dt} = -\frac{1}{d} \frac{d \ln \rho}{dt} \quad (\text{B.39})$$

Various techniques may then be used to adjust the value of  $h$ . For instance, Steinmetz & Mueller (1993) average the local density and use this to change  $h$ . Another often used method is to adjust it so that each particle has a constant number of neighbours Hernquist & Katz (1989). Ideally,  $h_a$  should be determined from the summation equations so that it is consistent with the density obtained from the summation, but this requires solving for each  $h_a$  iteratively and is not usually done. In some problems it might be necessary to replace the expression for  $h_a$  by a formula that limits how large or small  $h_a$  can become. For example, an upper bound on  $h_a$  is desirable when the density becomes very small, to prevent strong interactions

between a very low and a very high density region. This can be achieved if the expression for  $h_a$  is replaced by

$$h_a = \sigma \left( \frac{m_a}{A + \rho_a} \right)^{1/d} \quad (\text{B.40})$$

## B.7 Artificial viscosity

Lucy (1977) first introduced an artificial bulk viscosity to prevent a slow build-up of integration errors in SPH simulations. A different and more effective viscosity, which conserves linear and angular momentum was suggested and tested by Gingold & Monaghan (1983). It is important to realize that in problems involving strong shocks, SPH does not give the widths of shock fronts as accurately as the methods based on Riemann-solvers with similar resolution. However, no current method gives the width of a shock front accurately, since the width of real shock fronts is only a few molecular free mean paths. Typical resolutions in numerical simulations are a factor  $10^4$  greater. However, the key issue is that SPH yields the pre- and post-shock values of any physical quantity very accurately with a reasonable number of particles.

Nevertheless, in two and three dimensions it is more difficult for SPH to match the accuracy of modern finite difference codes. Its advantage is that it is independent of the special properties of the ideal gas equation, which are built into the finite difference codes. For this reason SPH can be used when the equation of state is complicated and Riemann solutions are unavailable. In reality, for astrophysical fluids the physical viscosity is extremely small. Thus, to handle shocks, a so-called artificial viscosity is introduced.

The artificial viscosity bears no relation to real viscosities. It is designed to allow shock phenomena to be simulated, or simply to stabilize a numerical algorithm. Artificial viscosities are often constructed analogously to real gas viscosities, replacing the mean free path with the resolution length. The Navier-Stokes equation for viscous flow has the form

$$\frac{dv_1}{dt} = -\frac{1}{\rho} \frac{\partial P}{\partial x_i} + \frac{1}{\rho} \left[ \frac{\partial}{\partial x_k} \left( \eta \left( \frac{\partial v_i}{\partial x_k} + \frac{\partial v_k}{\partial x_i} \frac{2}{3} \delta_{ik} \vec{\nabla} \cdot \vec{v} \right) \right) + \frac{\partial}{\partial x_i} (\zeta \vec{\nabla} \cdot \vec{v}) \right] \quad (\text{B.41})$$

where  $\eta$  is the shear viscosity coefficient and  $\zeta$  is the bulk viscosity. For a monoatomic gas

$$\eta \approx \frac{1}{3} \rho \lambda c_s \quad (\text{B.42})$$

where  $\lambda$  is the free mean path. The viscous terms can be estimated directly using the SPH interpolation formula but this leads to equations that do not conserve linear

and angular momentum. Gingold & Monaghan (1983) devised a viscosity by simple arguments about its form and its relation to gas viscosity. The viscous term is added to the pressure terms in SPH equations to give

$$\frac{d\vec{v}_a}{dt} = - \sum_b m_b \left( \frac{P_b}{\rho_b^2} + \frac{P_a}{\rho_a^2} + \Pi_{ab} \right) \vec{\nabla}_a W_{ab} \quad (\text{B.43})$$

where

$$\Pi_{ab} = -\nu \left( \frac{\vec{v}_{ab} \cdot \vec{r}_{ab}}{r_{ab}^2 + \varepsilon \langle h_{ab} \rangle^2} \right) \quad (\text{B.44})$$

being

$$\nu = \frac{\alpha \langle h_{ab} \rangle \langle c_{ab} \rangle}{\langle \rho_{ab} \rangle} \quad (\text{B.45})$$

and

$$\langle h_{ab} \rangle = \frac{h_a + h_b}{2} \quad (\text{B.46})$$

In this expression  $\varepsilon$  is a free parameter which is usually adopted to be  $\varepsilon \approx 0.01$ . This free parameter is introduced to prevent a singularity when  $r_{ab} = 0$ . Also

$$\langle c_{ab} \rangle = \frac{c_a + c_b}{2} \quad (\text{B.47})$$

is the average sound speed velocity and an equivalent expression is used to compute the average density  $\langle \rho_{ab} \rangle$ .

It can be easily shown that the artificial viscosity term is a Galilean invariant and vanishes for rigid rotation. When two particles approach each other, the artificial viscosity produces a repulsive force between the particles. When they recede from each other the force is attractive.

The SPH viscosity can be related to a continuum viscosity by converting the summation to integrals. The  $x$  component of the acceleration equation has the viscous contribution

$$f_x = \sum_b m_b \frac{\alpha \langle c_{ab} \rangle \langle h_{ab} \rangle}{\langle \rho_{ab} \rangle} \frac{\vec{v}_{ab} \cdot \vec{r}_{ab}}{r_{ab}^2 + \varepsilon \langle h_{ab} \rangle^2} (x_a - x_b) F_{ab} \quad (\text{B.48})$$

that can be written as a sum of terms if the  $\varepsilon$  is dropped. If  $\alpha$ ,  $c$ ,  $h$  and  $\rho$  are constant the continuum equivalent of  $f_x$  in two dimensions is

$$f_x = \alpha h c \left( \frac{3}{8} \frac{\partial^2 v_x}{\partial x \partial x} + \frac{1}{8} \frac{\partial^2 v_x}{\partial y \partial y} + \frac{1}{4} \frac{\partial^2 v_x}{\partial x \partial y} \right) \quad (\text{B.49})$$

This shows that the shear viscosity coefficient  $\eta = \rho\alpha hc/8$  and the bulk viscosity coefficient  $\zeta = 5\eta/3$ . In three dimensions  $\eta = \rho\alpha hc/10$  and  $\zeta = 5\eta/3$ . If there are rapid changes in the parameters, it is better to use

$$\Pi_{ab} = -\frac{16\mu_a\mu_b}{\rho_a\rho_b(\mu_a + \mu_b)} \left( \frac{v_{ab} \cdot r_{ab}}{r_{ab}^2 + \varepsilon\langle h_{ab} \rangle^2} \right) \quad (\text{B.50})$$

where

$$\mu_a = \frac{1}{8}\alpha_a h_a c_a \rho_a \quad (\text{B.51})$$

In the case of the shocks, it is usual to turn the viscosity on for approaching particles and turn it off for receding particles. In this way the viscosity is used for shocks and not rarefactions. Unfortunately this means that the viscosity is turned on when the density increases in the shock-free regions, for example when gravity pulls gas together.

When the viscosity was first used it was found to work well for shocks of moderate strength. Though, in astrophysical calculations involving colliding gas clouds, where the Mach number can be very high, it was found that gas particles from one cloud could stream between the particles of the other cloud. Generally, this streaming is limited to a few particle spacings and is therefore not a severe problem. However, it should not occur at all. To prevent this a new extra term can be included in the coefficient of the viscosity (Monaghan, 1992)

$$\nu = \frac{\langle h_{ab} \rangle}{\langle \rho_{ab} \rangle} \left( \alpha \langle c_{ab} \rangle - \beta \frac{\langle g_{ab} \rangle \vec{v}_{ab} \cdot \vec{r}_{ab}}{r_{ab}^2 + \varepsilon\langle h_{ab} \rangle^2} \right) \quad (\text{B.52})$$

Good results have been obtained with  $\alpha = 1$  and  $\beta = 2$ . Another form of the viscosity is found naturally by considering aspects of the dissipative term in shock solutions based on Riemann solvers, namely

$$\Pi_{ab} = -K \frac{v_{\text{sig}}(\vec{v}_{ab} \cdot \vec{r}_{ab})}{\langle \rho_{ab} \rangle |r_{ab}|} \quad (\text{B.53})$$

where  $K \sim 0.5$  and the signal velocity is defined as

$$v_{\text{sig}} = c_a + c_b - \beta \vec{v}_{ab} \cdot \frac{\vec{r}_{ab}}{|r_{ab}|} \quad (\text{B.54})$$

In this expression the constant  $\beta$  is usually adopted to be  $\approx 4$ . The signal velocity can be easily interpreted. If the fluid is at rest we estimate the speed at which a sound wave from  $a$  approaches a sound wave from  $b$  as  $(c_a + c_b)$ . The extra term represents the change in speed if the fluids at  $a$  and  $b$  are moving relatively to each other.

Viscosity dissipates the flow and transfers energy from kinetic to thermal, a contribution to the thermal energy that is always positive. Owing to the way in

which the SPH viscosity was derived, viscous dissipation is best obtained directly from the SPH equations. By taking the scalar product of  $\vec{v}_a$  and the acceleration equation, multiplying by  $m_a$  and summing over  $a$ , the viscous contribution to the rate of change of thermal energy can be identified. The final result is then

$$\frac{du_a}{dt} = \frac{P_a}{\Omega_a \rho_a^2} \sum_b m_b \vec{v}_{ab} \cdot \vec{\nabla}_a W_{ab} + \frac{1}{2} \sum_a m_a \sum_b m_b \Pi_{ab} \vec{v}_{ab} \cdot \vec{\nabla}_a W_{ab} \quad (\text{B.55})$$

Artificial dissipation is very successful for handling shocks but it can be too large in other parts of the flow. Another effect is that the Reynolds number of a flow is artificially increased. This leads to, for example, that the Kelvin-Helmholtz shear instabilities are heavily diffused. Balsara (1995) suggested reducing viscous dissipation by multiplying the artificial viscosity by the factor

$$\frac{|\vec{\nabla} \cdot \vec{v}|}{|\vec{\nabla} \cdot \vec{v}| + |\vec{\nabla} \times \vec{v}|} \quad (\text{B.56})$$

where  $\nabla \cdot \vec{v}$  is replaced by the symmetric pair of particles. Cornish & Larson (2003) found that it is preferable to replace the previous factor by

$$\frac{|\vec{\nabla} \cdot \vec{v}|}{|\vec{\nabla} \cdot \vec{v}| + \sqrt{E^{ij} E^{ij}} + 10^{-4} \langle c_{ab} \rangle / h} \quad (\text{B.57})$$

where the strain tensor  $E^{ij}$  is defined by

$$E^{ij} = \frac{1}{2} \left( \frac{\partial v^i}{\partial x^j} + \frac{\partial v^j}{\partial x^i} \right) \quad (\text{B.58})$$

The most commonly used prescription is (Monaghan & Gingold, 1983; Balsara, 1995)

$$\Pi_{ab} = \frac{-\alpha c_{ab} \mu_{ab} + \beta \mu_{ab}^2}{\rho_{ab}} \quad (\text{B.59})$$

if  $\vec{v}_{ab} \cdot \vec{r}_{ab} \leq 0$  and  $\Pi_{ab} = 0$  otherwise, where  $\alpha$  and  $\beta$  are adimensional constants whose value depends on the problem under study (typically  $\alpha = 1$  and  $\beta = 2$ ), and

$$\mu_{ab} = \frac{h_{ab} (\vec{v}_a - \vec{v}_b) \cdot (\vec{r}_a - \vec{r}_b)}{|\vec{r}_a - \vec{r}_b|^2 + \epsilon h_{ab}^2} \left( \frac{f_a + f_b}{2} \right) \quad (\text{B.60})$$

being  $\epsilon = 10^{-4}$ . Finally the factor  $f_a$  is defined as follows

$$f_a = \frac{|\vec{\nabla} \cdot \vec{v}_a|}{|\vec{\nabla} \cdot \vec{v}_a| + |\vec{\nabla} \times \vec{v}_a| + 0.0001 c_a / h_a} \quad (\text{B.61})$$

## B.8 Integration

Because the SPH algorithm reduces the original continuum partial differential equations to sets of ordinary differential equations, any stable time stepping algorithm for ordinary differential equations can be used to solve the problem. The aim of this section is to review these methods. The reader should bear in mind that SPH is an *approximate* method, and thus we will generally require the method to be stable, but not extremely accurate. Generally speaking we now have a problem in which we have solve a set of ordinary differential equations (ODEs) of the form

$$\frac{dy_i}{dx} + f_i(x, y_1, \dots, y_N) = 0, \quad i = 1, \dots, N \quad (\text{B.62})$$

The easiest and most straightforward way of integrating the system of ODEs is to use the so-called Euler method

$$y_i(x_{n+1}) \simeq y_i(x_n) - \delta x f(x_n, y_1(x_n), \dots, y_N(x_n)) \quad (\text{B.63})$$

where

$$\delta x = x_{n+1} - x_n \quad (\text{B.64})$$

However, this method is not very accurate. This can be seen by expanding  $y(x)$  around  $x_n$

$$y_i(x_{n+1}) = y_i(x_n) + \delta x \left. \frac{dy}{dx} \right|_n + \frac{\delta x^2}{2} \left. \frac{d^2 y}{dx^2} \right|_n + \dots \quad (\text{B.65})$$

Comparing Eqs. (2.63) and (2.65) it is clear that the difference between the true and the approximate solutions is of second order, which means that we have a first order approximation. Most importantly, we also want to study the stability of the solution. A method is stable if a small deviation from the true solution does not tend to grow as the solution is iterated. To do this end we assume that at some time the actual numerical solution deviates from the true solution of the difference equation by some small amount  $\delta y$ . By substrating we obtain

$$\begin{aligned} y_i(x_{n+1}) + \delta y_i(x_{n+1}) &\simeq y_i(x_n) + \delta y_i(x_n) \\ &- \delta x \left[ f \left( x_n, y_i(x_n) + \frac{\partial f}{\partial y_i} \Big|_n \delta y_i(x_n) \right) \right] \end{aligned} \quad (\text{B.66})$$

Hence, expanding around  $x_n$  and operating we have

$$\delta y_i(x_{n+1}) \simeq \left[ 1 - \delta x \left. \frac{\partial f}{\partial y_i} \right|_n \right] \delta y_i(x_n) = g \delta y_i(x_n) \quad (\text{B.67})$$

where  $g$  is the so-called growth factor. It is obvious that the Euler solution will be stable if the absolute value of the growth factor is smaller than unity, otherwise the perturbation will grow:

$$-1 \leq 1 - \delta x \left. \frac{\partial f}{\partial y^i} \right|_n \leq 1 \quad (\text{B.68})$$

This means that the choice of the integration step is limited. For instance, if

$$\left. \frac{\partial f}{\partial y_i} \right|_n < 0 \quad (\text{B.69})$$

the Euler method is unstable, whatever the choice of  $\delta x$  is, whereas if

$$\left. \frac{\partial f}{\partial y_i} \right|_n \geq 0 \quad (\text{B.70})$$

then by choosing an appropriately small  $\delta x$  we can stabilise the computation. Thus, the Euler method is conditionally stable. The Euler method can be improved by considering the different ways in which derivatives can be evaluated. For instance, another well known method, the Leap-Frog integrator uses another approximation (centered differences) for evaluating the derivatives:

$$\left. \frac{dy}{dx} \right|_n \simeq \frac{y_i(x_{n+1}) - y_i(x_{n-1}))}{2\delta x} \quad (\text{B.71})$$

and, consequently, we have

$$y_i(x_{n+1}) \simeq y_i(x_{n-1}) - 2\delta x f(x_{n-1}, y_i(x_n)) \quad (\text{B.72})$$

Applying the same techniques previously used, it can be shown that the Leap-Frog method is second order accurate. Also, the following stability condition can be obtained

$$\delta y_i(x_{n+1}) \simeq \delta y_i(x_{n-1}) - 2\delta x \left. \frac{\partial f}{\partial y} \right|_n \delta y_i(x_n) \quad (\text{B.73})$$

Thus, it is not guaranteed that the error will not grow as  $n$  increases and therefore the Leap-Frog method is also conditionally unstable. This is the method we use in our code.

Yet there are more accurate methods. For instance, the Runge-Kutta method uses a trial step in the middle of the interval to compute the solution across the whole interval

$$\begin{aligned}
k_1 &= f(x_n, y_i(x_n)) \delta x \\
k_2 &= f\left(x_n + \frac{1}{2}\delta x, y_i(x_n) - \frac{1}{2}k_1\right) \delta x \\
y_i(x_{n+1}) &\simeq y_i(x_n) - k_2 + O(\delta x^3)
\end{aligned} \tag{B.74}$$

There are also higher order Runge-Kutta schemes. They are also conditionally stable. It can be shown that

$$\delta y_i(x_{n+1}) \simeq \left[1 - \delta x \left.\frac{\partial f}{\partial y_i}\right|_n + \frac{1}{2} \left(\delta x \left.\frac{\partial f}{\partial y_i}\right|_n\right)^2\right] \delta y_i(x_n) \tag{B.75}$$

Consequently, the growth factor  $g$  must fulfill

$$|g| = \left|1 - \delta x \left.\frac{\partial f}{\partial y_i}\right|_n + \frac{1}{2} \left(\delta x \left.\frac{\partial f}{\partial y_i}\right|_n\right)^2\right| \leq 1 \tag{B.76}$$

Finally, the predictor-corrector method that considers a solution of the form

$$y_i(x_{n+1}) \simeq y_i(x_n) - \frac{1}{2} [f(x_{n+1}, y_i(x_{n+1})) + f(x_n, y_i(x_n))] \delta x \tag{B.77}$$

that does not have a direct solution as  $y_{n+1}$  appears on both sides, so the value has to be guessed

$$\begin{aligned}
y'_i(x_{n+1}) &= y_n - f(x_n, y_i(x_n)) \delta x \\
y_{n+1} &\simeq y_n - \frac{1}{2} [f(x_{n+1}, y'_i(x_{n+1})) + f(x_n, y_i(x_n))] \delta x
\end{aligned} \tag{B.78}$$

The accuracy and stability properties are identical to those of the Runge-Kutta method. We have used a stable method. However, the reader should take into account that, since SPH is an approximate method, it is preferable to do not invest much time in using high-order numerical schemes. It is also good to remember that maximum accuracy is desirable, of course, but not at any computational cost.



## Appendix C

# Cluster architecture

The SPH simulations described were run in a cluster of computers built by ourselves. We started its construction in 2004 and since then its has become an essential tool for performing efficient calculations.

### C.1 Characteristics of the cluster



Figure C.1: Front look of the cluster of computers.

The cluster is composed of 32 personal computers with Intel Pentium IV processors with velocities ranging from 2.8 up to 3.2 GHz and 1Gb of RAM. The computers

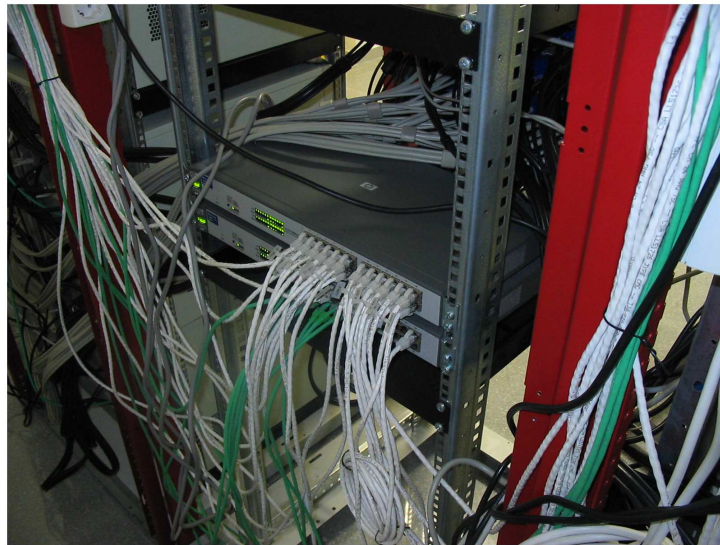


Figure C.2: Gigabit switches for internal communications.

are linked with Gigabit switches which ensure fast enough communications essential for the parallel calculations. A photograph of the actual cluster configuration is shown in Fig. C.1, whereas the detail of communications switches is shown in Fig. C.2. We installed the Red-Hat based LINUX operating system called LINUX-rocks which is specially designed for the installation, use and administration of clusters of computers. Some of the most remarkable features of the system are for example an extremely easy and friendly installation procedure, a complete set of administrative tools like a ready-to-use queue system or a completely automatic user control system. It also has an html interface that allows control and monitorization of the status of the cluster. This web page is accessible from any external computer.

One of the most complex task in designing the cluster has been the data storage system of the users. In fact all the computers of our cluster are standard computers with a hard disk of 60 Gb — see Fig. C.3. This means that none of them would be able to act as the master node and to store all the user data as required to obtain an optimal performance. To solve the problem, we decided to a particular node to each user, from which the data can be exported to the master node — which is the only accessible from outside the cluster — via NFS. In this way the cluster has a virtual master node with enough disk space for all data of a given user. Of course this structure has some limitations, because the NFS export of the data from the nodes can saturate the cluster internal communications. In order to partially overcome this problem we perform the data export via `autofs`, so the data is only transferred via NFS when the user is performing calculations. Only when many users



Figure C.3: Close look of one of the computers of the cluster.

are working simultaneously, which is a rare event, performance problems have been observed. However, this is only a partial solution and in the future, if more nodes and users are incorporated to the cluster, the acquisition of a high capacity storage unit will become an unavoidable necessity.



# Appendix D

## Code parallelization

In order to be able to perform the high resolution SPH simulations a parallelization of the code was an unavoidable task. Thus, one of the first tasks that has been tackled in the present thesis is the parallelization of the previously existing SPH code. In this appendix we discuss the parallelization strategy.

### D.1 Message Passage Interface and parallelization strategy

The **Message Passage Interface** or MPI is the parallelization language that was selected for the task. We have chosen this language because it is a well-established protocol which is widely used by the scientific community and because it is available in most scientific clusters of computers. MPI essentially consists of a set of subroutines that control the transfer of information between the different computers of the cluster and allows the user to freely design the parallelization strategy.

In order to tackle the problem we decided to adopt a conservative strategy, that is to parallelize just the most computationally-expensive subroutines. The most expensive part of our SPH code is by far the search of neighbors for the gravitational force calculation. This task actually accounts for more than 85% of the computing time. In sharp contrast the calculations involved in the hydrodynamical evolution need merely a 4% of the total computing time, an amount of computing time which is comparable the tree construction — which takes slightly more than a 3% of the time. The rest of the computing time is basically invested in the calculation of the input physics, including, among other necessary quantities, the calculation of the release of energy by nuclear reactions, the necessary thermodynamical quantities and the energy carried out by neutrinos. Thus, to parallelize the code the following strategy was followed. First the complete tree structure is calculated for each node, as shown in figure D.1. A more elegant and efficient approach would have been probably to build what it is known as the *locally essential tree* which is a small version of the

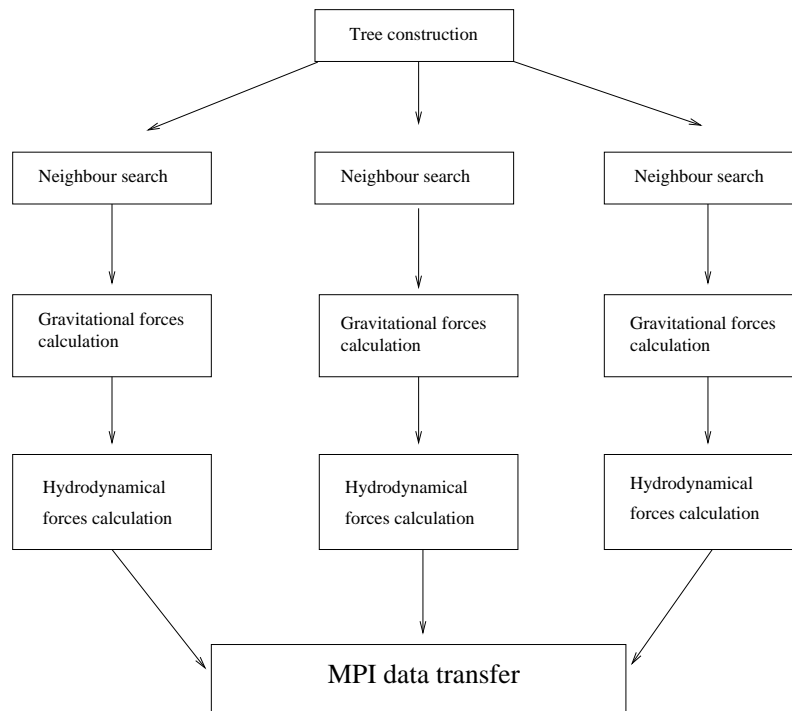


Figure D.1: Sketch of the calculation of the interactions in the parallel version of the SPH code. Each processor computes a local neighbor list and calculates the partial forces by walking the common tree. After doing this, the partial forces are sent to the rest of the nodes to obtain the total gravitational and hydrodynamical forces.

tree built in each node according to, for example, a spatial domain decomposition. With this local tree each processor is able to perform the subsequent tree walk and neighbour search with a minimum data transfer from the rest of the nodes. However, the tree construction is — as already commented — a relatively inexpensive process and we consider that for moderate numbers of particles the technical difficulties of its construction does not compensate its benefits.

Table D.1: Maximum gain factor as a function of the number of the particles used in the calculation. The gain factor is defined as the mean time spent in each time-step with one processor divided by the time spent with  $N_p$  processors.

Particles	Gain factor
300000	4.9
100000	6.7
50000	7.5
10000	8.0

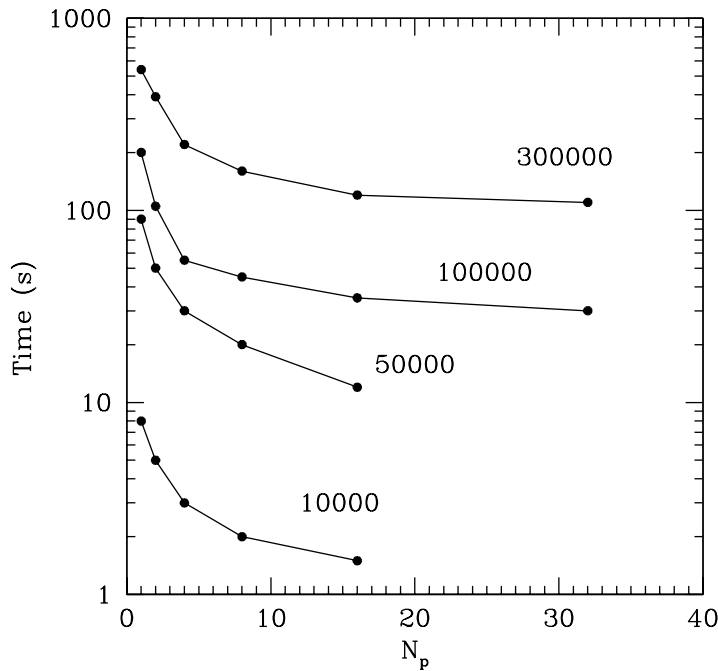


Figure D.2: Time spent by the program — in CPU seconds — to perform a complete SPH time-step as a function of the number of processors. Each curve is labelled with the number of particles of the simulation.

After tree construction we equally distribute particles into processors in order to evenly balance the computational work of every processor. This imposes a restriction to the number of processors that can be assigned to the parallel calculation, because the ratio between the number of particles and the number of processors must be an integer number. Note that at this stage no data transfer between processors is needed because all the information of the particles — including the tree structure — is present in every processor. Subsequently, each processor obtains from the global tree local neighbour lists which will be used to compute the hydrodynamical and gravitational forces for each particle. After the calculations we use the MPI subroutines to pass the local information of each processor to the rest of nodes, which are needed to continue the calculations. This transfer of information of course limits the computational gain, because the time needed for data transfer is finite, but as can be seen in table D.1 with this design very reasonable gain factors have been obtained.

In Fig. D.2 we show the limiting effect of internal communications as the number of processors employed in the calculation is increased. Note that for a sufficiently

large number of nodes adding a new node does not increase the efficiency of the calculation. There is no way to avoid such limiting effect because of the increasing demands of internal data transfers needed. However, our feeling is that the gain factor can be enhanced by code optimization. This is undoubtedly something that must be tackled in the future if we want to further increase the resolution of the simulations.

# Bibliography

- ABRAMOVICI, A., ALTHOUSE, W. E., DREVER, R. W. P., GURSEL, Y., KAWAMURA, S., RAAB, F. J., SHOEMAKER, D., SIEVERS, L., SPERO, R. E. & THORNE, K. S., 1992. LIGO - The Laser Interferometer Gravitational-Wave Observatory. *Science*, **256**, 325–333.
- ACERNESE, F., AMICO, P., ARNAUD, N., BABUSCI, D., BARILLÉ, R. ET AL., 2004. Status of VIRGO. *Classical and Quantum Gravity*, **21**, 385.
- ALCOCK, C. & ILLARIONOV, A., 1980. The surface chemistry of stars. I - Diffusion of heavy ions in white dwarf envelopes. II - Fractionated accretion of interstellar matter. *ApJ*, **235**, 534–553.
- ALEXANDER, D. R. & FERGUSON, J. W., 1994. Low-temperature Rosseland opacities. *ApJ*, **437**, 879–891.
- ALTHAUS, L. G., GARCÍA-BERRO, E., ISERN, J. & CÓRSICO, A. H., 2005a. Mass-radius relations for massive white dwarf stars. *A&A*, **441**, 689–694.
- ALTHAUS, L. G., SERENELLI, A. M., CÓRSICO, A. H. & MONTGOMERY, M. H., 2003. New evolutionary models for massive ZZ Ceti stars. I. First results for their pulsational properties. *A&A*, **404**, 593–609.
- ALTHAUS, L. G., SERENELLI, A. M., PANEI, J. A., CÓRSICO, A. H., GARCÍA-BERRO, E. & SCÓCCOLA, C. G., 2005b. The formation and evolution of hydrogen-deficient post-AGB white dwarfs: The emerging chemical profile and the expectations for the PG 1159-DB-DQ evolutionary connection. *A&A*, **435**, 631–648.
- ARMITAGE, P. J. & CLARKE, C. J., 1996. Magnetic braking of T Tauri stars. *MNRAS*, **280**, 458–468.
- BALSARA, D. S., 1995. von Neumann stability analysis of smooth particle hydrodynamics—suggestions for optimal algorithms. *Journal of Computational Physics*, **121**, 357–372.

- BARNES, J. & HUT, P., 1986. A Hierarchical  $O(N\log N)$  Force-Calculation Algorithm. *Nature*, **324**, 446–449.
- BECKLIN, E. E., FARIHI, J., JURA, M., SONG, I., WEINBERGER, A. J. & ZUCKERMAN, B., 2005. A Dusty Disk around GD 362, a White Dwarf with a Uniquely High Photospheric Metal Abundance. *ApJ*, **632**, L119–L122.
- BENACQUISTA, M., SEDRAKIAN, D. M., HAIRAPETYAN, M. V., SHAHABASYAN, K. M. & SADOYAN, A. A., 2003. Gravitational Radiation from Pulsating White Dwarfs. *ApJ*, **596**, L223–L226.
- BENDER, P. L., *et al.*, 1998. LISA: Laser Interferometer Space Antenna for the detection and observation of GW. *Pre-phase A Report (Garching: Max Planck-Institut für Quantenoptik)*.
- BENDER, P. L., *et al.*, 2000. LISA: A conerstone mission for the observation of gravitational waves. *ESA-SCI(2000)11, System and Technology Study Report*.
- BENVENUTO, O. G., GARCÍA-BERRO, E. & ISERN, J., 2004. Asteroseismological bound on  $\dot{G}/G$  from pulsating white dwarfs. *Phys. Rev. D*, **69**(8), 082002–+.
- BENZ, W., 1990. *The numerical modelling of Nonlinear stellar Pulsations*. J. Buchler (Dordrecht: Kluwer Academic Publishers).
- BENZ, W., CAMERON, A. G. W. & BOWERS, R. L., 1989a. Dynamic Mass Exchange in Doubly Degenerate Binaries - Part Two - the Importance of Nuclear Energy Release. In G. Wegner, ed., *IAU Colloq. 114: White Dwarfs*, vol. 328 of *Lecture Notes in Physics, Berlin Springer Verlag*, 511–+.
- BENZ, W., CAMERON, A. G. W., PRESS, W. H. & BOWERS, R. L., 1990. Dynamic mass exchange in doubly degenerate binaries. I - 0.9 and 1.2 solar mass stars. *ApJ*, **348**, 647–667.
- BENZ, W., THIELEMANN, F.-K. & HILLS, J. G., 1989b. Three-dimensional hydrodynamical simulations of stellar collisions. II - White dwarfs. *ApJ*, **342**, 986–998.
- BERGERON, P., WESEMAEL, F. & FONTAINE, G., 1991. Synthetic spectra and atmospheric properties of cool DA white dwarfs. *ApJ*, **367**, 253–269.
- BRADLEY, P. A., 1998. White Dwarf Data Tables. *Baltic Astronomy*, **7**, 355–367.
- BRADLEY, P. A., 2001. Asteroseismological Constraints on the Structure of the ZZ Ceti Stars L19-2 and GD 165. *ApJ*, **552**, 326–339.
- BRADLEY, P. A. & WINGET, D. E., 1994. An asteroseismological determination of the structure of the DBV white dwarf GD 358. *ApJ*, **430**, 850–857.

- CAMPBELL, B., 1984. New radio sources at AFGL 2591 - Young cluster or single star? *ApJ*, **287**, 334–337.
- CERDONIO, M., FORTINI, P., ORTOLAN, A., PRODI, G. A. & VITALE, S., 1993. Concept of a resonant-antennae observatory for gravitational wave bursts. *Physical Review Letters*, **71**, 4107–4110.
- CHIANG, E. I. & GOLDREICH, P., 1997. Spectral Energy Distributions of T Tauri Stars with Passive Circumstellar Disks. *ApJ*, **490**, 368–+.
- CLAYTON, G. C., GEBALLE, T. R., HERWIG, F., FRYER, C. & ASPLUND, M., 2007. Very Large Excesses of  $^{18}\text{O}$  in Hydrogen-deficient Carbon and R Coronae Borealis Stars: Evidence for White Dwarf Mergers. *ApJ*, **662**, 1220–1230.
- CLEMENT, M. J., 1974. On the solution of Poisson’s equation for rapidly rotating stars. *ApJ*, **194**, 709–714.
- COCCIA, E., FAFONE, V., FROSSATI, G., LOBO, J. A. & ORTEGA, J. A., 1998. Hollow sphere as a detector of gravitational radiation. *Phys. Rev. D*, **57**, 2051–2060.
- COORAY, A., FARMER, A. J. & SETO, N., 2004. The Optical Identification of Close White Dwarf Binaries in the Laser Interferometer Space Antenna Era. *ApJ*, **601**, L47–L50.
- CORNISH, N. J. & LARSON, S. L., 2003. LISA data analysis: Source identification and subtraction. *Phys. Rev. D*, **67**(10), 103001.
- CÓRSICO, A. H., ALTHAUS, L. G., BENVENUTO, O. G. & SERENELLI, A. M., 2001a. New DA white dwarf evolutionary models and their pulsational properties. *A&A*, **380**, L17–L20.
- CÓRSICO, A. H., ALTHAUS, L. G., BENVENUTO, O. G. & SERENELLI, A. M., 2002. The mode trapping properties of full DA white dwarf evolutionary models. *A&A*, **387**, 531–549.
- CÓRSICO, A. H., ALTHAUS, L. G., MONTGOMERY, M. H., GARCÍA-BERRO, E. & ISERN, J., 2005. New evolutionary models for massive ZZ Ceti stars. II. The effects of crystallization on their pulsational properties. *A&A*, **429**, 277–290.
- CÓRSICO, A. H., BENVENUTO, O. G., ALTHAUS, L. G., ISERN, J. & GARCÍA-BERRO, E., 2001b. The potential of the variable DA white dwarf G117-B15A as a tool for fundamental physics. *New Astronomy*, **6**, 197–213.
- CÓRSICO, A. H., GARCÍA-BERRO, E., ALTHAUS, L. G. & ISERN, J., 2004. Pulsations of massive ZZ Ceti stars with carbon/oxygen and oxygen/neon cores. *A&A*, **427**, 923–932.

- COX, J. P., 1980. *Theory of stellar pulsation*. Research supported by the National Science Foundation Princeton, NJ, Princeton University Press, 1980. 393 p.
- DOLEZ, N. & VAUCLAIR, G., 1981. Gravity modes instability in DA white dwarfs. *A&A*, **102**, 375–385.
- DOMINIK, C. & DECIN, G., 2003. Age Dependence of the Vega Phenomenon: Theory. *ApJ*, **598**, 626–635.
- D’SOUZA, M. C. R., MOTL, P. M., TOHLIN, J. E. & FRANK, J., 2006. Numerical Simulations of the Onset and Stability of Dynamical Mass Transfer in Binaries. *ApJ*, **643**, 381–401.
- DURISEN, R. H., 1973. Viscous Effects in Rapidly Rotating Stars with Application to White-Dwarf Models. Theory and Techniques. *ApJ*, **183**, 205–214.
- EGGLETON, P. P., 1983. Approximations to the radii of Roche lobes. *ApJ*, **268**, 368–+.
- EINSTEIN, A., 1916. Die Grundlage der allgemeinen Relativitätstheorie. *Annalen der Physik*, **49**, 769–822.
- EVANS, C. R., IBEN, I. J. & SMARR, L., 1987. Degenerate dwarf binaries as promising, detectable sources of gravitational radiation. *ApJ*, **323**, 129–139.
- FARMER, A. J. & PHINNEY, E. S., 2003. The gravitational wave background from cosmological compact binaries. *MNRAS*, **346**, 1197–1214.
- GARCIA-BERRO, E. & IBEN, I., 1994. On the formation and evolution of super-asymptotic giant branch stars with cores processed by carbon burning. 1: SPICA to Antares. *ApJ*, **434**, 306–318.
- GARCÍA-BERRO, E., LORÉN-AGUILAR, P., CÓRSICO, A. H., ALTHAUS, L. G., LOBO, J. A. & ISERN, J., 2006. The gravitational wave radiation of pulsating white dwarfs revisited: the case of BPM 37093 and PG 1159-035. *A&A*, **446**, 259–266.
- GARCÍA-BERRO, E., LORÉN-AGUILAR, P., PEDEMONTE, A. G., ISERN, J., BERGERON, P., DUFOUR, P. & BRASSARD, P., 2007. Evidence of a Merger of Binary White Dwarfs: The Case of GD 362. *ApJ*, **661**, L179–L182.
- GAUTSCHY, A. & SAIO, H., 1995. Stellar Pulsations Across The HR Diagram: Part 1. *ARA&A*, **33**, 75–114.
- GAUTSCHY, A. & SAIO, H., 1996. Stellar Pulsations Across the HR Diagram: Part 2. *ARA&A*, **34**, 551–606.

- GIANNINAS, A., DUFOUR, P. & BERGERON, P., 2004. Discovery of a Cool, Massive, and Metal-rich DAZ White Dwarf. *ApJ*, **617**, L57–L60.
- GINGOLD, R. A. & MONAGHAN, J. J., 1977. Smoothed particle hydrodynamics - Theory and application to non-spherical stars. *MNRAS*, **181**, 375–389.
- GINGOLD, R. A. & MONAGHAN, J. J., 1983. On the fragmentation of differentially rotating clouds. *MNRAS*, **204**, 715–733.
- GOKHALE, V., PENG, X. M. & FRANK, J., 2007. Evolution of Close White Dwarf Binaries. *ApJ*, **655**, 1010–1024.
- GUERRERO, J., GARCÍA-BERRO, E. & ISERN, J., 2004. Smoothed Particle Hydrodynamics simulations of merging white dwarfs. *A&A*, **413**, 257–272.
- GUTIÉRREZ, J., CANAL, R. & GARCÍA-BERRO, E., 2005. The gravitational collapse of ONe electron-degenerate cores and white dwarfs: The role of  $^{24}\text{Mg}$  and  $^{12}\text{C}$  revisited. *A&A*, **435**, 231–237.
- GUTIERREZ, J., GARCIA-BERRO, E., IBEN, I. J., ISERN, J., LABAY, J. & CANAL, R., 1996. The Final Evolution of ONeMg Electron-Degenerate Cores. *ApJ*, **459**, 701–+.
- HANSEN, B. M. S., KULKARNI, S. & WIKTOROWICZ, S., 2006. A Spitzer Search for Infrared Excesses around Massive Young White Dwarfs. *AJ*, **131**, 1106–1118.
- HERNQUIST, L. & KATZ, N., 1989. TREESPH - A unification of SPH with the hierarchical tree method. *ApJS*, **70**, 419–446.
- HILS, D., BENDER, P. L. & WEBBINK, R. F., 1990. Gravitational radiation from the Galaxy. *ApJ*, **360**, 75–94.
- IBEN, JR., I. & TUTUKOV, A. V., 1984. Supernovae of type I as end products of the evolution of binaries with components of moderate initial mass (M not greater than about 9 solar masses). *ApJS*, **54**, 335–372.
- IGLESIAS, C. A. & ROGERS, F. J., 1996. Updated Opal Opacities. *ApJ*, **464**, 943–+.
- ISERN, J., HERNANZ, M. & GARCIA-BERRO, E., 1992. Axion cooling of white dwarfs. *ApJ*, **392**, L23–L25.
- ITOH, N., HAYASHI, H. & KOHYAMA, Y., 1994. Electrical and Thermal Conductivities of Dense Matter in the Crystalline Lattice Phase. III. Inclusion of Lower Densities: Erratum. *ApJ*, **436**, 418–+.

- ITO, N., HAYASHI, H., NISHIKAWA, A. & KOHYAMA, Y., 1996. Neutrino Energy Loss in Stellar Interiors. VII. Pair, Photo-, Plasma, Bremsstrahlung, and Recombination Neutrino Processes. *ApJS*, **102**, 411–+.
- ITO, N., KOHYAMA, Y. & TAKEUCHI, H., 1987. Viscosity of dense matter. *ApJ*, **317**, 733–736.
- IZZARD, R. G., JEFFERY, C. S. & LATTANZIO, J., 2007. Origin of the early-type R stars: a binary-merger solution to a century-old problem? *A&A*, **470**, 661–673.
- JI, H., BURIN, M., SCHARTMAN, E. & GOODMAN, J., 2006. Hydrodynamic turbulence cannot transport angular momentum effectively in astrophysical disks. *Nature*, **444**, 343–346.
- JURA, M., 2003. A Tidally Disrupted Asteroid around the White Dwarf G29-38. *ApJ*, **584**, L91–L94.
- KANAAN, A., KEPLER, S. O., GIOVANNINI, O. & DIAZ, M., 1992. The discovery of a new DAV star using IUE temperature determination. *ApJ*, **390**, L89–L91.
- KANAAN, A., NITTA, A., WINGET, D. E., KEPLER, S. O., MONTGOMERY, M. H. ET AL., 2005. Whole Earth Telescope observations of BPM 37093: A seismological test of crystallization theory in white dwarfs. *A&A*, **432**, 219–224.
- KAWALER, S. D., 1998. What can we Learn from Wet about how to Make White Dwarfs? *Baltic Astronomy*, **7**, 11–20.
- KAWALER, S. D. & BRADLEY, P. A., 1994. Precision asteroseismology of pulsating PG 1159 stars. *ApJ*, **427**, 415–428.
- KEPLER, S. O., MUKADAM, A., WINGET, D. E., NATHER, R. E., METCALFE, T. S., REED, M. D., KAWALER, S. D. & BRADLEY, P. A., 2000. Evolutionary Timescale of the Pulsating White Dwarf G117-B15A: The Most Stable Optical Clock Known. *ApJ*, **534**, L185–L188.
- KILIC, M., VON HIPPEL, T., LEGGETT, S. K. & WINGET, D. E., 2005. Excess Infrared Radiation from the Massive DAZ White Dwarf GD 362: A Debris Disk? *ApJ*, **632**, L115–L118.
- KING, A. R., PRINGLE, J. E. & WICKRAMASINGHE, D. T., 2001. Type Ia supernovae and remnant neutron stars. *MNRAS*, **320**, L45–L48.
- KOESTER, D. & WILKEN, D., 2006. The accretion-diffusion scenario for metals in cool white dwarfs. *A&A*, **453**, 1051–1057.

- LANDAU, L. D. & LIFSHITZ, E. M., 1975. *The classical theory of fields*. Course of theoretical physics - Pergamon International Library of Science, Technology, Engineering and Social Studies, Oxford: Pergamon Press, 1975, 4th rev.engl.ed.
- LIEBERT, J., BERGERON, P. & HOLBERG, J. B., 2005. The Formation Rate and Mass and Luminosity Functions of DA White Dwarfs from the Palomar Green Survey. *ApJS*, **156**, 47–68.
- LIVIO, M. & PRINGLE, J. E., 1992. Dwarf nova outbursts - The ultraviolet delay and the effect of a weakly magnetized white dwarf. *MNRAS*, **259**, 23P–26P.
- LIVIO, M., PRINGLE, J. E. & SAFFER, R. A., 1992. Planets around massive white dwarfs. *MNRAS*, **257**, 15P–+.
- LIVIO, M., PRINGLE, J. E. & WOOD, K., 2005. Disks and Planets around Massive White Dwarfs. *ApJ*, **632**, L37–L39.
- LORÉN-AGUILAR, P., GUERRERO, J., ISERN, J., LOBO, J. A. & GARCÍA-BERRO, E., 2005. Gravitational wave radiation from the coalescence of white dwarfs. *MNRAS*, **356**, 627–636.
- LUCY, L. B., 1977. A numerical approach to the testing of the fission hypothesis. *AJ*, **82**, 1013–1024.
- MAGNI, G. & MAZZITELLI, I., 1979. Thermodynamic properties and equations of state for hydrogen and helium in stellar conditions. *A&A*, **72**, 134–147.
- MARSH, T. R., NELEMANS, G. & STEEGHS, D., 2004. Mass transfer between double white dwarfs. *MNRAS*, **350**, 113–128.
- MIRONOWSKI, V. M., 1965. Gravitational wave radiation from binaries. *Soviet Astr.*, **9**, 752.
- MISNER, C. W., THORNE, K. S. & WHEELER, J. A., 1973. *Gravitation*. San Francisco: W.H. Freeman and Co., 1973.
- MOCHKOVITCH, R. & LIVIO, M., 1989. The coalescence of white dwarfs and type I supernovae. *A&A*, **209**, 111–118.
- MOCHKOVITCH, R. & LIVIO, M., 1990. The coalescence of white dwarfs and type I supernovae - The merged configuration. *A&A*, **236**, 378–384.
- MONAGHAN, J. J., 1985. Particle methods for hydrodynamics. *Comput. Phys. Rep.*, **3**, 71–124.
- MONAGHAN, J. J., 1992. Smoothed particle hydrodynamics. *ARA&A*, **30**, 543–574.

- MONAGHAN, J. J., 1997. SPH and Riemann Solvers. *Journal of Computational Physics*, **136**, 298–307.
- MONAGHAN, J. J., 2005. Smoothed particle hydrodynamics. *Rep. Prog. in Phys.*, **68**, 1703–1759.
- MONAGHAN, J. J. & GINGOLD, R. A., 1983. Shock simulation by the particle method SPH. *Jour. of Comp. Phys.*, **52**, 374–389.
- MONAGHAN, J. J. & LATTANZIO, J. C., 1985. A refined particle method for astrophysical problems. *A&A*, **149**, 135–143.
- MONTGOMERY, M. H. & WINGET, D. E., 1999. The Effect of Crystallization on the Pulsations of White Dwarf Stars. *ApJ*, **526**, 976–990.
- MOTL, P. M., TOHLINE, J. E. & FRANK, J., 2002. Numerical Methods for the Simulation of Dynamical Mass Transfer in Binaries. *ApJS*, **138**, 121–148.
- NAKAMURA, T. & OOHARA, K.-I., 1989. *Methods in 3 D numerical relativity.*, 254–280. *Frontiers in Numerical Relativity*.
- NATHER, R. E., 1995. Status of the Wet. *Baltic Astronomy*, **4**, 117–126.
- NELEMANS, G., 2003. Galactic Binaries as Sources of Gravitational Waves. In J. M. Centrella, ed., *The Astrophysics of Gravitational Wave Sources*, vol. 686 of *American Institute of Physics Conference Series*, 263–272.
- NELEMANS, G., PORTEGIES ZWART, S. F., VERBUNT, F. & YUNGELSON, L. R., 2001a. Population synthesis for double white dwarfs. II. Semi-detached systems: AM CVn stars. *A&A*, **368**, 939–949.
- NELEMANS, G., YUNGELSON, L. R., PORTEGIES ZWART, S. F. & VERBUNT, F., 2001b. Population synthesis for double white dwarfs . I. Close detached systems. *A&A*, **365**, 491–507.
- NOMOTO, K. & IBEN, JR., I., 1985. Carbon ignition in a rapidly accreting degenerate dwarf - A clue to the nature of the merging process in close binaries. *ApJ*, **297**, 531–537.
- OSAKI, Y. & HANSEN, C. J., 1973. Nonradial oscillations of cooling white dwarfs. *ApJ*, **185**, 277–292.
- PACZYŃSKI, B. & SIENKIEWICZ, R., 1972. Evolution of Close Binaries VIII. Mass Exchange on the Dynamical Time Scale. *Acta Astronomica*, **22**, 73–91.
- PANDEY, J. C., SINGH, K. P., DRAKE, S. A. & SAGAR, R., 2005. Unravelling the Nature of HD 81032 - A New RS CVn Binary. *Journal of Astrophysics and Astronomy*, **26**, 359–+.

- PAQUETTE, C., PELLETIER, C., FONTAINE, G. & MICHAUD, G., 1986. Diffusion in white dwarfs - New results and comparative study. *ApJS*, **61**, 197–217.
- PFEIFFER, B., VAUCLAIR, G., DOLEZ, N., CHEVRETON, M., FREMY, J.-R. ET AL., 1996. Whole Earth Telescope observations and seismological analysis of the cool ZZ Ceti star GD 154. *A&A*, **314**, 182–190.
- POSTNOV, K. A. & YUNGELSON, L. R., 2006. The Evolution of Compact Binary Star Systems. *Living Reviews in Relativity*, **9**, 6–+.
- PRICE, D. J., 2007. splash: An Interactive Visualisation Tool for Smoothed Particle Hydrodynamics Simulations. *Publications of the Astronomical Society of Australia*, **24**, 159–173.
- PRINCE, T. A., BINETRUY, P., CENTRELLA, J., FINN, L., HOGAN, C., NELEMANS, G. & PHINNEY, S., 2007. Probing the Universe with Gravitational Waves: the Laser Interferometer Space Antenna (LISA). In *American Astronomical Society Meeting Abstracts*, vol. 211 of *American Astronomical Society Meeting Abstracts*, 140.01–+.
- RAUSCHER, T. & THIELEMANN, F.-K., 2000. Astrophysical Reaction Rates From Statistical Model Calculations. *Atomic Data and Nuclear Data Tables*, **75**, 1–2.
- RITOSSA, C., GARCIA-BERRO, E. & IBEN, I. J., 1996. On the Evolution of Stars That Form Electron-degenerate Cores Processed by Carbon Burning. II. Isotope Abundances and Thermal Pulses in a  $10 M_{sun}$  Model with an ONe Core and Applications to Long-Period Variables, Classical Novae, and Accretion-induced Collapse. *ApJ*, **460**, 489–+.
- RITOSSA, C., GARCÍA-BERRO, E. & IBEN, I. J., 1999. On the Evolution of Stars that Form Electron-degenerate Cores Processed by Carbon Burning. V. Shell Convection Sustained by Helium Burning, Transient Neon Burning, Dredge-out, URCA Cooling, and Other Properties of an 11  $M_{\text{solar}}$  Population I Model Star. *ApJ*, **515**, 381–397.
- ROBINSON, E. L., KEPLER, S. O. & NATHER, R. E., 1982. Multicolor variations of the ZZ Ceti stars. *ApJ*, **259**, 219–231.
- ROSSWOG, S., 2007. Fallback accretion in the aftermath of a compact binary merger. *MNRAS*, **376**, L48–L51.
- ROSSWOG, S. & DAVIES, M. B., 2002. High-resolution calculations of merging neutron stars - I. Model description and hydrodynamic evolution. *MNRAS*, **334**, 481–497.

- ROSSWOG, S., DAVIES, M. B., THIELEMANN, F.-K. & PIRAN, T., 2000. Merging neutron stars: asymmetric systems. *A&A*, **360**, 171–184.
- ROSSWOG, S. & LIEBENDÖRFER, M., 2003. High-resolution calculations of merging neutron stars - II. Neutrino emission. *MNRAS*, **342**, 673–689.
- SAIO, H. & NOMOTO, K., 1985. Evolution of a merging pair of C + O white dwarfs to form a single neutron star. *A&A*, **150**, L21–L23.
- SALARIS, M., GARCÍA-BERRO, E., HERNANZ, M., ISERN, J. & SAUMON, D., 2000. The Ages of Very Cool Hydrogen-rich White Dwarfs. *ApJ*, **544**, 1036–1043.
- SCHMIDT, G. D., BERGERON, P., LIEBERT, J. & SAFFER, R. A., 1992. Two ultramassive white dwarfs found among candidates for magnetic fields. *ApJ*, **394**, 603–608.
- SCHUTZ, B. F., 1999. Gravitational wave astronomy. *Classical and Quantum Gravity*, **16**, A131–A156.
- SCHUTZ, B. F. & RICCI, F., 2001. Gravitational Waves, Sources and Detectors. In *Gravitational Waves*, 11–+.
- SEGRETAİN, L., CHABRIER, G. & MOCHKOVITCH, R., 1997. The Fate of Merging White Dwarfs. *ApJ*, **481**, 355–+.
- SERNA, A., ALIMI, J.-M. & CHIEZE, J.-P., 1996. Adaptive Smooth Particle Hydrodynamics and Particle-Particle Coupled Codes: Energy and Entropy Conservation. *ApJ*, **461**, 884.
- SETO, N., 2002. Long-term operation of the Laser Interferometer Space Antenna and Galactic close white dwarf binaries. *MNRAS*, **333**, 469–474.
- SHAKURA, N. I. & SYUNYAEV, R. A., 1973. Black holes in binary systems. Observational appearance. *A&A*, **24**, 337–355.
- STARRFIELD, S., COX, A. N., KIDMAN, R. B. & PESNELL, W. D., 1984. Nonradial instability strips based on carbon and oxygen partial ionization in hot, evolved stars. *ApJ*, **281**, 800–810.
- STEINMETZ, M. & MUELLER, E., 1993. On the capabilities and limits of smoothed particle hydrodynamics. *A&A*, **268**, 391–410.
- TAKAHASHI, R. & THE TAMA COLLABORATION, 2004. Status of TAMA300. *Classical and Quantum Gravity*, **21**, 403.
- UNGLAUB, K. & BUES, I., 2000. The chemical evolution of hot white dwarfs in the presence of diffusion and mass loss. *A&A*, **359**, 1042–1058.

- UNNO, W., OSAKI, Y., ANDO, H., SAIO, H. & SHIBAHASHI, H., 1989. *Nonradial oscillations of stars*. Nonradial oscillations of stars, Tokyo: University of Tokyo Press, 1989, 2nd ed.
- VILLAVER, E. & LIVIO, M., 2007. Can Planets Survive Stellar Evolution? *ApJ*, **661**, 1192–1201.
- WEBBINK, R. F., 1984. Double white dwarfs as progenitors of R Coronae Borealis stars and Type I supernovae. *ApJ*, **277**, 355–360.
- WERNER, K., HEBER, U. & HUNGER, K., 1991. Non-LTE analysis of four PG1159 stars. *A&A*, **244**, 437–461.
- WILLKE, B., AUFMUTH, P., AULBERT, C., BABAK, S., BALASUBRAMANIAN, R. ET AL., 2004. Status of GEO 600. *Classical and Quantum Gravity*, **21**, 417.
- WINGET, D. E., KEPLER, S. O., KANAAN, A., MONTGOMERY, M. H. & GIOVANNINI, O., 1997. An Empirical Test of the Theory of Crystallization in Stellar Interiors. *ApJ*, **487**, L191+.
- WINGET, D. E., NATHER, R. E., CLEMENS, J. C., PROVENCAL, J., KLEINMAN, S. J. ET AL., 1991. Asteroseismology of the DOV star PG 1159 - 035 with the Whole Earth Telescope. *ApJ*, **378**, 326–346.
- WINGET, D. E., VAN HORN, H. M., TASSOUL, M., FONTAINE, G., HANSEN, C. J. & CARROLL, B. W., 1982. Hydrogen-driving and the blue edge of compositionally stratified ZZ Ceti star models. *ApJ*, **252**, L65–L68.
- WOOSLEY, S. E. & WEAVER, T. A., 1986. The physics of supernova explosions. *ARA&A*, **24**, 205–253.
- YOON, S.-C., PODSIADLOWSKI, P. & ROSSWOG, S., 2007. Remnant evolution after a carbon-oxygen white dwarf merger. *MNRAS*, **380**, 933–948.
- YUNGELSON, L. R., LIVIO, M., TUTUKOV, A. V. & SAFFER, R. A., 1994. Are the observed frequencies of double degenerates and SN IA contradictory? *ApJ*, **420**, 336–340.